TOHOKU
UNIVERSITY

# The 13th International Symposium on Water Environment Systems

## ---with Perspective of Global Safety

**13th ~ 15th November, 2025**


Department of Civil and Environmental Engineering
Graduate School of Engineering
Tohoku University


GP-RSS
International Joint Graduate Program in Resilience and Safety Studies

SyDE
WISE Program for Sustainability in the Dynamic Earth
変動地球共生学卓越大学院プログラム

# SPONSORS


**International Joint Graduate Program in Resilience and Safety Studies of Tohoku University**

**http://gp-rss.tohoku.ac.jp/**


**WISE Program for Sustainability in the Dynamic Earth of Tohoku University**
**https://syde.tohoku.ac.jp/**


**Department of Civil and Environmental Engineering, Graduate School of Engineering, Tohoku University**
**https://www.eng.tohoku.ac.jp/**

**Graduate School of Environmental Sciences, Tohoku University**
**https://www.kankyo.tohoku.ac.jp/**

## ORGANIZERS

| | |
|---|---|
| Dr. So KAZAMA | Professor, Tohoku Univ |
| Dr. Yu-You LI | Professor, Tohoku Univ |
| Dr. Daisuke SANO | Professor, Tohoku Univ |
| Dr. Keiko UDO | Professor, Tohoku Univ |
| Dr. Kengo KUBOTA | Associate Professor, Tohoku Univ |
| Dr. Mohan AMARASIRI | Associate Professor, Tohoku Univ |
| Dr. Rajapaksha Mudiyansekage Janaka Bamunawala | Assistant Prof., Tohoku Univ |

## SECRETARIATS

| | |
|---|---|
| Dr. Yusuke HIRAGA | Assistant Professor, Tohoku Univ |
| Dr. Yu QIN | Assistant Professor, Tohoku Univ |
| Dr. Wakana OISHI | Assistant Professor, Tohoku Univ |
| Dr. Yujie CHEN | Assistant Professor, Tohoku Univ |
| Dr. Juntong HA | Postdoctoral Researcher, Tohoku Univ |
| Zhafirah Meuthia ARDHANA | DC Student, Tohoku Univ |
| Weiyi WANG | DC Student, Tohoku Univ |

# PARTICIPANTS

**Qingdao University**, China

| | |
|---|---|
| Jin LI | Professor |

**Suzhou University of Science and Technology**, China

| | |
|---|---|
| Yong HUANG | Professor |
| Zhe KONG | Associate Professor |

**Taiyuan University of Technology**, China

| | |
|---|---|
| Jin YUAN | Professor |
| Liuying SONG | Assistant Professor |
| Biru ZHOU | Assistant Professor |
| Xuan WANG | Student |
| Xin SUI | Student |
| Yanbiao MA | Student |
| Haoye YANG | Student |

**Biogas Institute of Ministry of Agriculture and Rural Affairs**, China

| | |
|---|---|
| Lan WANG | Associate Professor |
| Na JIANG | Associate Professor |
| Yunhong ZHANG | Associate Professor |
| Hongwei ZHANG | Associate Professor |
| Hongnan YANG | Associate Professor |
| Runda DU | Assistant Professor |

**King Mongkut's University of Technology Thonburi**, Thailand

| | |
|---|---|
| Chaiwat EKKAWATPANIT | Associate Professor |

**The University of Tokyo**, Japan

| | |
|---|---|
| Jiayuan JI | Associate Professor |
| Heng Yi TEAH | Associate Professor |
| Jialing NI | Assistant Professor |

**Xi'an University of Architecture & Technology**, China

| | |
|---|---|
| Bao-Shan XING | Associate Professor |

**King Mongkut's University of Technology North Bangkok**, Thailand

| | |
|---|---|
| Weerayuth PRATOOMCHAI | Senior Lecturer |

**University of Moratuwa**, Sri Lanka

| | |
|---|---|
| Chaminda SP | Senior Lecturer |

**Sir John Kotelawala Defence University**, Sri Lanka

| | |
|---|---|
| Nilupul K. GUNASEKARA | Senior Lecturer |

**Universiti Putra Malaysia**, Malaysia

| | |
|---|---|
| Muhammad Aslam Mohd SAFARI | Senior Lecturer |

**OYO Corporation Pacific**, Japan

| | |
|---|---|
| Vladimir MOYA QUIROGA | Researcher |

**Beijing University of Technology**, China

| | |
|---|---|
| Lifang LIU | Student |

**Zhejiang University of Technology**, China

| | |
|---|---|
| Liangxu ZHOU | Student |

**Fukushima University**, Japan

| | |
|---|---|
| Sheikh Hefzul BARI | Student |

**Tohoku University**, Japan

| | |
|---|---|
| Yusuke HIRAGA | Assistant Professor |
| Amalia Nafisah Rahmani IRAWAN | Assistant Professor |
| Huqe FARHANA | Researcher |
| Adriana LEDEZMA-ESTRADA | Researcher |
| Hiroto BAUER | Student |
| Wasitha DILSHAN | Student |
| Zhaolong GU | Student |
| Atsuya IKEMOTO | Student |
| Sachio IWABU | Student |
| Takaya KANEKO | Student |
| Keita KUBO | Student |
| Yunhao LIU | Student |

| | |
|---|---|
| Kumudu Madhawa KURUGAMA | Student |
| Takuya MATSUMOTO | Student |
| Tomoaki MATSUURA | Student |
| Muthiah SADIDAH | Student |
| Sohta TADAKI | Student |
| Ryotaro TAHARA | Student |
| Tao YAMAMOTO | Student |
| Kanchana WIJERATNA | Student |
| Shoya TANAKA | Student |
| Shenghao JI | Student |
| Weizhe XIA | Student |
| Weiquan LI | Student |

# FIELDWORK

## 13 Nov (Thu)

### Fieldwork I: Arahama Elementary School and Natori-Denshokan

**・Arahama Elementary School**


This facility preserves and maintains the school building of the Arahama Elementary School in Sendai, which was damaged by the Great East Japan Earthquake on March 11, 2011, as a relic of the disaster, with the aim of raising awareness of disaster prevention and disaster mitigation among many people. The school building, which still retains clear traces of the disaster, is open to the public and exhibits images and videos of the immediate aftermath of the disaster so that visitors can experience the power and threat of the tsunami.

**・Natori-Denshokan**


The museum aims to pass on the memories and lessons of the Great East Japan Earthquake to the rest of the world and to future generations, to keep the disaster from fading away, and to foster awareness of disaster prevention. We are grateful for all the support we have received and will continue to work together with storytellers and local residents involved in disaster prevention activities to help realize a society that is resilient to natural disasters.

## Fieldwork II: Sen-en purification center and JNEX bioplant

**Gathering: 8:50 at Aobayama bus stop (青葉山駅前) (reserved only)**

**・Sen-en purification center**

Sen-en purification center, receiving 120,000 $m^3$/day of wastewater, is the second largest wastewater treatment plant in Miyagi-ken. The A/O and A/A/O methods are used to treat the wastewater and the sewage sludge is effectively digested for biogas, which is further converted to low-carbon electricity in the plant.

**・Jnex bioplant**


Jnex has been the largest biogas plant in Japan. This plant receives organic solid wastes from local areas and produces biogas, electricity and fertilizers. Jnex is making contributions to sustainable society in Sendai by reducing solid wastes, recycling bio-energy and reusing organic matters and nutrients.

# SYMPOSIUM

## 14 Nov (Fri) (GMT +9)

## 8:50 - 9:00 Opening Speech & Group Photo

## 9:00-12:30 Oral Session I : *Water & Wastewater treatment*

| | |
|---|---|
| 9:00 - 9:30 | [Keynote Lecture]<br>Exerting applied voltage promotes microbial activity of marine anammox bacteria for nitrogen removal in saline wastewater treatment<br>**Jin LI**, *Qingdao University* |
| 9:30 - 10:00 | [Keynote Lecture]<br>Anaerobic treatment of amide-containing industrial organic wastewater for synergetic removal of carbon and nitrogen<br>**Zhe KONG**, *Suzhou University of Science and Technology* |
| 10:00-10:15 | Evaluation and Restoration of Ecosystem Services in the Mining Area of the Ecologically Fragile Region along the Yellow River: A Case Study of the Xiegou Coal Mine<br>**Xin SUI**, *Taiyuan University of Technology* |
| 10:15-10:30 | Integrating Climate Change and Hydrological Models for Resilient Water Environment Infrastructure<br>**Vladimir MOYA QUIROGA**, *OYO Corporation Pacific* |
| 10:30-10:45 | Effects of Cell-to-Cell Communication Molecule Concentration on Toxin Production in Microcystis aeruginosa<br>**Shoya TANAKA**, *Tohoku University* |
| 10:45-11:00 | ***Coffee break*** |
| 11:00-11:15 | The in situ enrichment of low-density dispersed anammox bacteria and identification of its inhibitory and stimulatory metabolites<br>**Lan WANG**, *Biogas Institute of Ministry of Agriculture and Rural Affairs* |
| 11:15-11:30 | Enhanced Nutrient Removal via Small-Granule Sludge Formation in a Novel Continuous-Flow Reactor<br>**Lifang LIU**, *Beijing University of Technology* |
| 11:30-11:45 | The enhancement effect and mechanism of air mixing on biogas production performance in anaerobic digestion<br>**Hongnan YANG**, Biogas Institute of Ministry of Agriculture and Rural Affairs |

| | |
|---|---|
| 11:45-12:00 | Methane Extraction from Anaerobic Digestion of Rice Straw: Opportunities and Obstacles<br>**Huqe FARHANA**, *Tohoku University* |
| 12:00-12:15 | Life Cycle Carbon Benefit Assessment of Mine Water Reclamation and Utilization<br>**Xuan WANG**, *Taiyuan University of Technology* |
| 12:15-12:30 | PFAS in Aquatic Environments: A Growing Concern and the Role of Advanced Oxidation Processes in Remediation<br>**Adriana LEDEZMA-ESTRADA**, *Tohoku University* |

## 12:30-13:30 *Lunch Break*

## 13:30-14:30 Poster Session

Construction and Performance Enhancement of Photocatalysis–Microbe Coupled $CO_2$ Fixation Systems

**Hongwei ZHANG**, *Biogas Institute of Ministry of Agriculture and Rural Affairs*

Removal of antibiotic resistance genes from post-treated swine wastewater by mFe/nCu system

**Yunhong ZHANG**, *Biogas Institute of Ministry of Agriculture and Rural Affairs*

The enhanced performance of partial denitrification/anammoxhydroxyapatite (PDA-HAP) system based on the high up-flow velocity

**Shenghao JI**, *Tohoku University*

Municipal Wastewater Treatment by Novel Two-step System Based on Partial-denitrification /Anammox Process

**Weizhe XIA**, *Tohoku University*

Effects of Hydraulic Retention Time and Organic Loading Rate on Mesophilic Methanogenic Treatment of Brewery spent grain

**Weiquan LI**, *Tohoku University*

Skiing in a Changing Climate: A CONUS404 Analysis of Historical Snowfall Trends for U.S. Skiing

**Hiroto BAUER**, *Tohoku University*

Hydro-morphological controls on suspended sediment dynamics in the Abukuma River watershed

**Sheikh Hefzul BARI**, *Fukushima University*

Assessing Climate Change Impacts on Extreme Precipitation Using Large-Ensemble Data and Stochastic Storm Transposition: A Case Study for the Arakawa Watershed

**Wasitha DILSHAN**, *Tohoku University*

Long-Term Flood Resilience in the Chao Phraya River Basin, Thailand: Evidence from Historical Temples

**Zhaolong GU**, *Tohoku University*

An Integrated Evaluation of the Potential for Hydropower Generation and Flood Damage Reduction in Irrigation Reservoirs Across Japan

**Atsuya IKEMOTO**, *Tohoku University*

Verification of the Reproducibility of Extreme Precipitation in the Japanese Regional Reanalysis Data RRJ-Conv

**Sachio IWABU**, *Tohoku University*

An Integrative Assessment of Flood Control Efficacy and Maladaptation Risks Associated with Riparian Vegetation Clearing

**Takaya KANEKO**, *Tohoku University*

Effects of River Management Abandonment on Aquatic Insect Diversity in Small and Medium Rivers

**Keita KUBO**, *Tohoku University*

Physical Understanding of Parameters in a Large Woody Debris Discharge Model

**Yunhao LIU**, *Tohoku University*

## 14:45-18:00 Oral Session II : *Hydrology & Hydro-ecology*

| | |
|---|---|
| 14:45-15:10 | Flood Inundation Forecasting using Deep Learning Models<br>**Chaiwat EKKAWATPANIT**, *King Mongkut's University of Technology Thonburi* |
| 15:10-15:35 | An Assessment of Water Resources and Management in Bueng-Kan Province, Thailand: Sub-Mekong River Basin<br>**Weerayuth PRATOOMCHAI**, *King Mongkut's University of Technology North Bangkok* |
| 15:35-16:00 | Adaptive Modeling of Extreme Precipitation in Japan using Peaks Over Threshold Approach<br>**Muhammad Aslam Mohd SAFARI**, *Universiti Putra Malaysia* |
| 16:00-16:10 | ***Coffee break*** |
| 16:10-16:35 | Seasonal Variability and Climate Influence on Water Quality Parameters in the Kelani River Basin, Sri Lanka: A Two-Decade Analysis<br>**Chaminda SP**, *University of Moratuwa* |
| 16:35-17:00 | Flood Resilience and Community Safety: Insights from a Case-study in the Kelani Basin, Sri Lan<br>**Nilupul K. GUNASEKARA**, *Sir John Kotelawala Defence University* |
| 17:00-17:25 | Assessing agricultural drought vulnerability in Indonesia using 1-km gridded crop yield dataset<br>**Amalia Nafisah Rahmani IRAWAN**, *Tohoku University* |

## 17:30 - 18:00 General discussion & Closing Remarks

## 18:00 - 20:00 Network Dinner

# VENUE of SYMPOSIUM

Main Building of Graduate School of Environmental Studies (GSES),
Aobayama New Campus, Tohoku University

東北大学　新青葉山キャンパス　環境科学研究科本館(J22)

- Lectures: Room 204, Lecture Hall　（講演発表：204室　大講義室）
- Posters: Exhibition Space 2　（ポスター発表：102室　展示スペース２）

- Network Dinner: Center Hall & Aoba Restaurant (C01)
  （懇親会：工学部中央棟・工学部食堂(C01)）

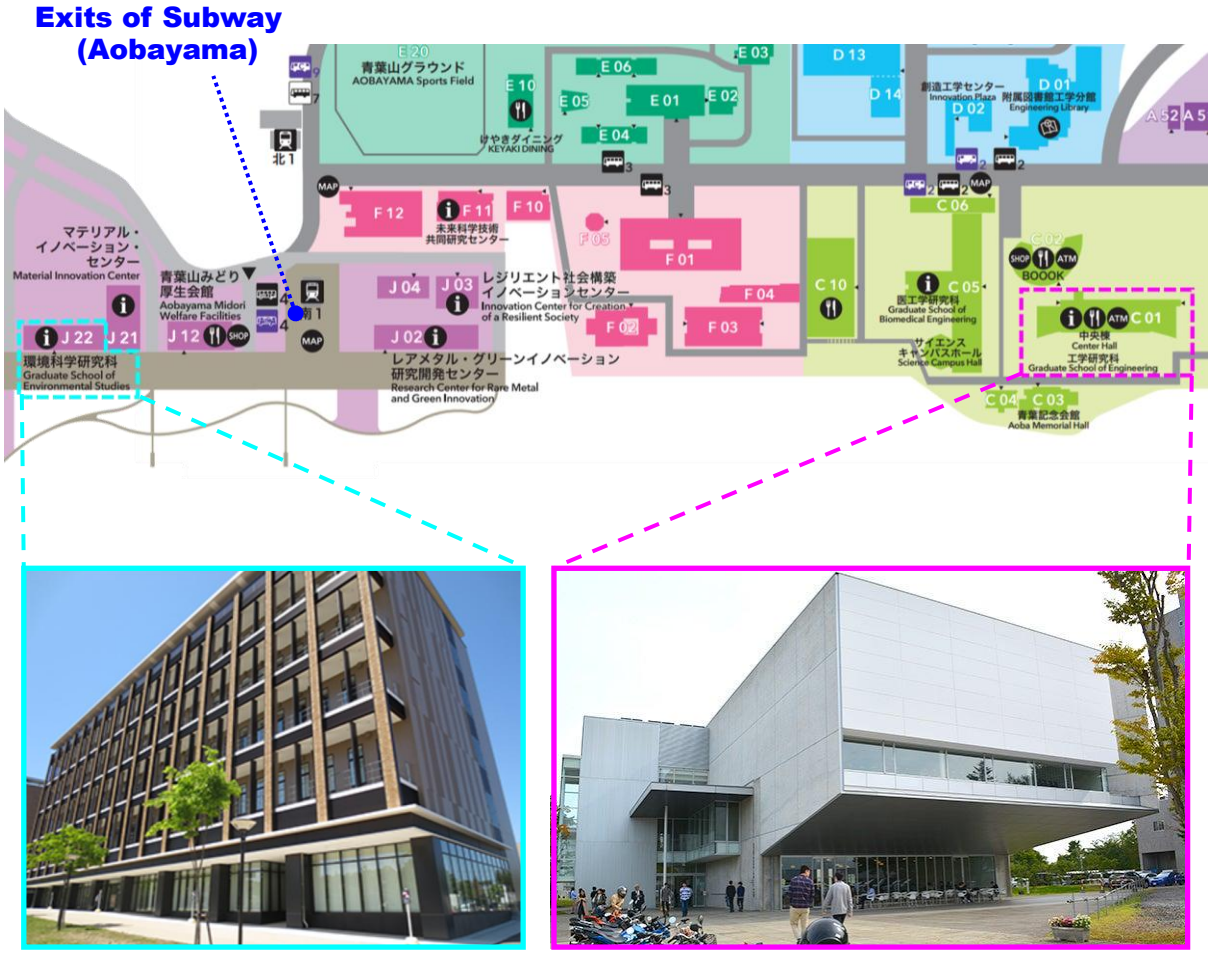


Left: Main Building of GSES (J22, 環境科学研究科本館)

Right: Center Hal & Aoba Restaurant (C01, 工学部中央棟・工学部食堂)

# ACCESS

## to Aobayama Campus, Tohoku Univ.

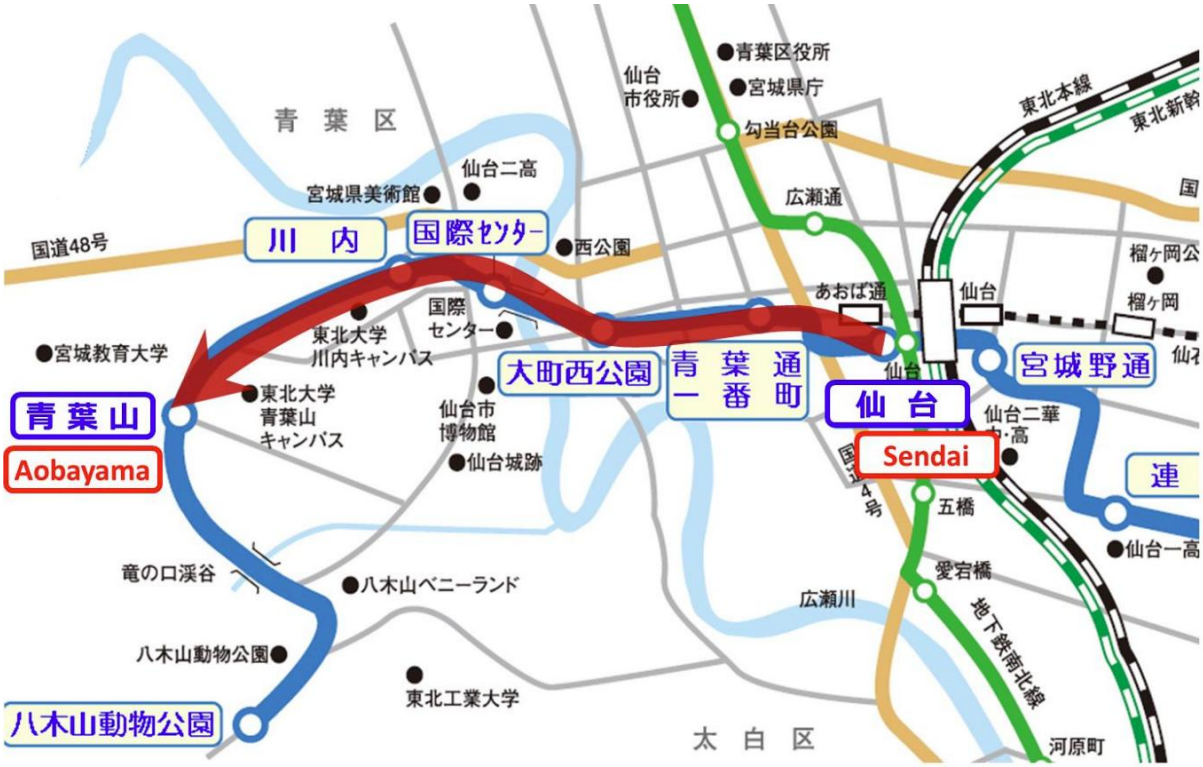


Public access: Only Subway **Tozai Line** is recommended.

If you start from **Sendai Sation** (or Aoba-dori Ichiban-cho), please take the direction of Yagiyama Zoological Park (Yagiyama Dobutsu Koen) and get off at **Aobayama**. (Ticket fee: 250 Yen)

公共交通機関：　地下鉄・東西線はオススメ

「仙台駅」（又は「青葉通一番町」）から「八木山動物公園」方面に「青葉山」まで。

（運賃：250 円）

# Exerting applied voltage promotes microbial activity of marine anammox bacteria for nitrogen removal in saline wastewater treatment

Zhi Hu, Yulong Zhang, Zhaopeng Qu & ○Jin Li*
[1] School of Environmental Science and Engineering, Qingdao University, Qingdao 266071, China

*E-mail: ljin0532@126.com

**Abstract**

To date, the application of marine anammox bacteria (MAB) is still a challenge in saline wastewater treatment due to the low growth rate and high sensitivity. Herein, bioelectrochemical system with applied voltage was exerted for the first time to promote the activity of MAB for removing nitrogen from saline wastewater. At the optimal voltage of 1.5 V, the mean total nitrogen removal rate (TNRR) reached the maximum of 0.65 kg/m3•d, which was 27.45% higher than that without applied voltage. Besides, applied voltage reduced the microbial diversity of MAB-based consortia, but the relative abundance of Candidatus Scalindua increased by 4.63% at 1.5 V compared with that without applied voltage. Also, proper applied voltage promoted the secretion of EPS and heme c, which resulted in the enhancement of MAB activity. Based on the remodified Logistic model analysis, the lag time of the nitrogen removal process was shortened by 0.72 h at the voltage of 1.5 V. Furthermore, it was found that higher voltage (> 2.0 V) had a negative effect on the MAB activity for low TNRR of 0.33 kg/m3•d (2.5 V). However, TNRR increased back to 0.61 kg/m3•d after removing the high applied voltage, which implied that the bioactivity was recoverable after being inhibited. These findings demonstrated that external electrical stimulation is an effective strategy to promote nitrogen removal and MAB activity for treating saline wastewater.

**Keywords:** Applied voltage, Marine anammox bacteria, Nitrogen removal, Microbial community, Saline wastewater.

# Anaerobic treatment of amide-containing industrial organic wastewater for synergetic removal of carbon and nitrogen

Zhe Kong[1, 2*]

[1] School of Environmental Science and Engineering, Suzhou University of Science and Technology, Suzhou, 215009, China

[2] Suzhou National Joint Laboratory of Green and Low-carbon Wastewater Treatment and Resource Utilization, Suzhou University of Science and Technology, Suzhou, 215009, China

*E-mail: zhekong@mail.usts.edu.cn

**Abstract**

Effective anaerobic digestion (AD) of N, N-dimethylformamide (DMF) and stable anaerobic treatment of high-strength DMF-containing wastewater was realized in this study, and verified by a lab-scale up-flow anaerobic sludge blanket (UASB). Synthetic wastewater with a constant DMF concentration of approximately 2000 mg/L and an organic loading rate (OLR) of approximately 3.0 kg COD/$m^3$/d was effectively treated during a 350-day long-term operation. The UASB initially realized a rapid start-up and maintained a high DMF removal with stable methane production for two months due to the enrichment of DMF-hydrolyzing bacteria (DHB) contained in the seed sludge. However, hydrolysis of DMF was gradually weakened due to the continuous decaying of DHB, and these DHB were unable to proliferate anaerobically. Dosing nitrate to the UASB resulted in a significant recovery of both DMF removal and methane production. Since DHB like *Paracoccus* are also known as denitrifying bacteria, dosage of nitrate significantly stimulated and enhanced their growth and DMF-hydrolyzing ability under the condition of simultaneous denitrification and methanogenesis (SDM), facilitating the establishment of an enhanced system: DHB hydrolyze DMF and simultaneously perform the heterotrophic denitrification to maintain the proliferation by feeding a portion of intermediates, while the rest of intermediates are directly utilized by methane-producing archaea (MPA). After long-term of adjustment, a molar ratio of approximately 1.59 for nitrate to DMF (N/D ratio) could realize an effective removal of 98.8% for the anaerobic degradation of DMF with stable methane production rate of 0.60 L/L. This study introduces a new direction to enhance the methanogenic degradation of degradation-resistant organic matters.

# Evaluation of Ecosystems and Construction of Ecological Management Models in Ecologically Fragile Mining Areas along the Yellow River: A Case Study of Xiegou Coal Mine

○ Xin Sui[1*], Jin Yuan[1] & Xuan Wang[1]

[1] Department of Environmental Science and Engineering, Taiyuan University of Technology, Taiyuan 510275, China.

[*]E-mail: suixin0155@link.tyut.edu.cn.

**Abstract**

The ecological protection and high-quality development of the Yellow River Basin are national strategic priorities, with fragile mining areas facing acute conflicts between ecosystem vulnerability and energy exploitation. This study takes the Xiegou mining area in Lvliang County, Shanxi Province—a core zone of both the national ecological security barrier and the Western Shanxi Energy Base—as a case to examine the spatiotemporal evolution of ecosystem services, values, security, and spatial networks from 2002 to 2022. Multi-source remote sensing (Landsat, MODIS), statistical data, the InVEST model, and spatial analysis techniques were employed to quantify water yield, soil retention, carbon storage, and habitat quality, and to reveal driving mechanisms. Results show that early high-intensity coal mining caused sharp declines in ecosystem functions, with water yield and soil retention most severely impacted. Recovery in later periods was driven by reclamation projects, vegetation restoration, and policy interventions, leading to enhanced multifunctional synergy and reduced trade-off hotspots, although residual conflicts remained in monoculture plantation zones. Ecosystem service value (ESV) increased overall, with forest land contributing most to value gains, while large-scale conversion of cropland to construction land and artificial grassland drove ESV decline. Ecological security exhibited a four-phase trajectory: high, decline (low point in 2012), recovery, and stabilization, with natural factors dominating early changes and anthropogenic management prevailing later. Integrating ecological function, value, and security into a resistance-surface framework, an ecological spatial network was constructed, identifying source areas, corridors, and critical nodes, and classifying four management zones—from core protection to system reconstruction—with corresponding targeted strategies. This closed-loop approach, spanning function assessment, value evaluation, security diagnosis, network optimization, and zoning design, offers actionable guidance for achieving synergy between energy development and ecological protection in fragile mining regions.

**Keywords:** mining area ecological restoration; ecosystem services; ecological security; ecological network; ecosystem service value

# Integrating Climate Change and Hydrological Models for Resilient Water Environment Infrastructure

○ Vladimir MOYA QUIROGA[1*], Adriana LEDEZMA[1]

[1]OYO Corporation Pacific, 1-12-24 Goya, Okinawa-shi, 〒904-0021, Okinawa, Japan
[*]E-mail: vmoya@oyopacific.com; vmoyaqg@gmail.com

## Abstract

This study quantifies the impacts of climate change–induced floods on civil infrastructure within water environment systems through coupled climate change and hydrological modeling. Climate projections from multiple global circulation models were bias-corrected and downscaled under SSP2-4.5 and SSP5-8.5 scenarios, to simulate future discharges for future periods 2021–2040, 2041–2060, and 2081–2100. The calibrated hydrological model reproduced historical flows (1990–2009). Results for the upper Madeira River basin (~1 million km²) indicate peak discharge increases of 10–40%, implying higher flood depths, erosion, and infrastructure vulnerability. Findings underscore the necessity of integrating quantitative climate risk analysis into water environment system design to enhance resilience and optimize long-term infrastructure investments.

**Keywords:** Water resources, Climate change, Numerical modelling.

## 1 Introduction

Floods are among the most destructive natural hazards affecting water environment systems, disrupting hydrological functions, damaging infrastructure, and threatening public safety. Climate change has intensified these risks by altering precipitation regimes and increasing the frequency of extreme rainfall events, particularly in tropical and subtropical regions. As a result, conventional design standards based on historical hydrological data often underestimate the magnitude and frequency of future flood events.

To address this challenge, modern engineering must integrate climate science into the analysis and management of water systems [1]. Quantitative climate risk assessment allows engineers to evaluate hazard, vulnerability, and exposure under future climate conditions, thereby improving the design of flood protection structures and the resilience of civil infrastructure.

This study presents an integrated framework combining hydrological modeling and climate change projections to quantify future flood impacts on civil infrastructure. The approach is applied to the upper Madeira River basin in South America, providing insights into expected flood behavior and infrastructure vulnerability under different climate scenarios.

## 2 Materials and methods

The study was conducted in the Upper Madeira River Basin, a major transboundary catchment encompassing areas of Bolivia, Brazil, and Peru. The Hydrologic Engineering Center's Hydrologic Modeling System (HEC-HMS) was employed to simulate the rainfall–runoff processes and quantify the effects of climate change on flood magnitudes. The model structure incorporated sub-basin delineation based on a digital elevation model, soil characteristics, and land-use data. Calibration and validation were performed using daily discharge observations from 1990 to 2009, remote sensing precipitation CHIRPS [2], and reanalysis evapotranspiration ERA5 [3] ensuring reliable representation of hydrological response under present conditions.

Future simulations were driven by climate projections from three global circulation models—EC-Earth3, EC-Earth3-Veg, and TaiESM1—under two Shared Socioeconomic Pathways (SSP2-4.5 and SSP5-8.5), consistent with the IPCC Sixth Assessment Report framework. The GCM outputs were bias-corrected and statistically downscaled to local scales. The corrected precipitation and temperature inputs were used to generate streamflow series for 2021–2040, 2041–2060, and 2081–2100, supporting the assessment of projected changes in flood magnitude, duration, and recurrence. Statistical analysis was applied to analyze flood frequency curves and flow duration curve for the present and future conditions A graphical description of the methodology is shown in **Fig. 1**.

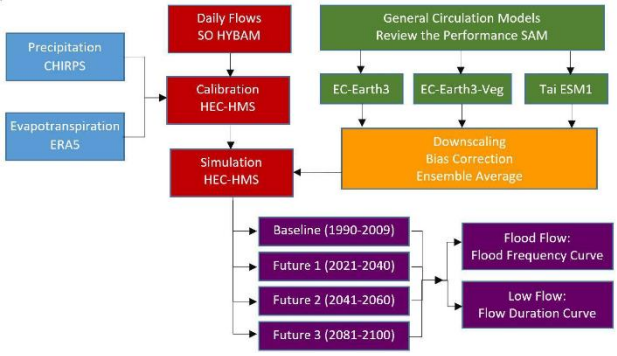


**Fig. 1. Methodology**

## 3 Results and discussion

The calibrated HEC-HMS model accurately reproduced the hydrological response of the Upper Madeira River Basin, demonstrating good agreement between simulated and observed daily discharges for the 1990–2009 baseline period. Performance metrics, including the Nash–Sutcliffe Efficiency (NSE), percentage bias, and the coefficient of determination ($R^2$), indicated reliable model performance across the control stations (**Table 1**); in all the stations the performance indicators indicate either satisfactory or a very good performance. This provided a solid basis for projecting future hydrological behavior under climate change scenarios. The model outputs revealed that the basin exhibits a strong

seasonal regime, with peak flows during the austral summer months (December–March) and pronounced low flows during the dry season (June–September).

**Table. 1. Hydrological model performance**

| Station | NSE | Bias [%] |
|---|---|---|
| Abapo | 0.440 | 0.83 |
| Abuna | 0.848 | 1.55 |
| CachuelaEsperanza | 0.667 | -5.09 |
| Camiaco | 0.593 | 0.45 |
| Guayaramerin | 0.759 | -6.23 |
| Ichilo | 0.470 | 2.07 |
| Miraflores | 0.515 | 4.23 |
| Pimenteiras | 0.747 | -4.05 |
| Principe Beira | 0.819 | 0.33 |
| Pto. Siles | 0.680 | -5.67 |
| Pto. Varador | 0.585 | 4.19 |
| Riberalta | 0.732 | 5.12 |
| Rurrenabaque | 0.665 | 0.38 |
| Sena | 0.607 | -2.26 |
| Vila Bela | 0.686 | -3.62 |

Future projections based on bias-corrected climate data from multiple global circulation models showed consistent increases in extreme precipitation and corresponding flood discharges (**Fig. 2**). Under both SSP2-4.5 and SSP5-8.5 scenarios, results indicated intensification of wet-season flows, with mean peak discharges increasing by approximately 10% basin-wide for 2021–2040, and up to 25–40% in localized sub-basins toward the late-century horizon (2081–2100). The most pronounced changes occurred in headwater areas characterized by steep slopes and high rainfall intensities, where runoff generation is particularly sensitive to changes in precipitation. In contrast, low-flow conditions during dry periods are projected to decrease by 10–20%, suggesting potential challenges for navigation, water supply, and hydropower generation. These findings highlight a likely amplification of hydrological extremes, resulting in greater flood magnitudes and longer flood durations.

The observed trends carry significant implications for infrastructure planning and management within the basin. The projected increase in flood peaks implies elevated risks of overtopping, scouring, and structural fatigue in hydraulic works such as bridges, culverts, and levees. Additionally, road and urban drainage systems designed under stationary assumptions may face higher frequencies of design exceedance, leading to service disruptions and maintenance cost escalation. The reduction in low flows further emphasizes the need for integrated water management strategies to balance flood protection with water availability during dry seasons. The results demonstrate that a quantitative, model-based climate risk assessment provides a more reliable basis for adaptation planning than traditional, purely empirical methods. Incorporating such analyses into engineering practice will enable more resilient infrastructure design and optimize investment by aligning structural capacity with projected hydrological conditions.

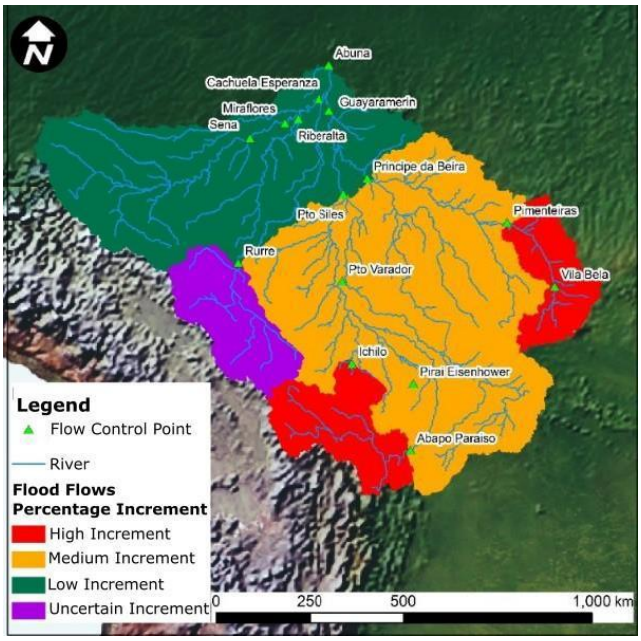


**Fig. 2. Future flood flow changes.**

## 4 Conclusions

The objective of the present study was to evaluate the impacts of climate change on the civil infrastructure related to rivers in the upper basin of the Madera River. The results show that the flood flows (used for the engineering design) will have a significant percentage increment with respect to current conditions. In other words, civil works designed based on current conditions will experience flows greater than the design flows. This percentage increase is different depending on the stations. Stations can be grouped into four groups according to their percentage flood flows increase: Stations with a high percentage increment, stations with a medium percentage increase, stations with a low percentage increase, stations without a defined trend.

This study highlights the significant influence of land use and climate change on streamflow dynamics in the Upper Madeira River Basin. Using HEC-HMS modeling, results demonstrate how deforestation and intensified rainfall may heighten flood risks and alter hydrological responses. These findings emphasize the need for integrated watershed management and sustainable land-use planning to enhance regional resilience.

## Reference

[1] Salas, E., Moya, V., & Mendoza, S. (2025). Cómo reducir la incertidumbre por cambio climático en el desarrollo de infraestructura [How to reduce climate change uncertainty in infrastructure development]. CAF Banco de Desarrollo de América Latina., February 2025.
[2] Funk, C., Peterson, P., Landsfeld, M., Pedreros, D., Verdin, J., Shukla, S. & Michaelsen, J. (2015). The Climate Hazards InfraRed Precipitation with Station data (CHIRPS) dataset. Remote Sensing of Environment, 165, 38–55
[3] Hersbach, H., Bell, B., Berrisford, P., Hirahara, S., Horányi, A., Muñoz-Sabater, J., … & Thépaut, J.-N. (2020). The ERA5 global reanalysis. Quarterly Journal of the Royal Meteorological Society, 146(730), 1999–2049

# Effects of Cell-to-Cell Communication Molecule Concentration on Toxin Production in *Microcystis aeruginosa*

○ Shoya TANAKA[1*], Yohei MIURA [1] & Daisuke SANO[1]
[1]Department of Civil Engineering, Tohoku University, Miyagi 980-8579, Japan.
[*]E-mail: tanaka.shoya.s8@dc.tohoku.ac.jp

**Abstract**
In semi-enclosed water bodies, such as dam reservoirs, an abnormal increase of cyanobacteria, known as harmful algal blooms (HABs), often occurs. When such water is utilized as a drinking water source, the toxic substances produced by cyanobacteria can pose serious problems. It has been suggested that *Microcystis aeruginosa*, a species of cyanobacteria, may synthesize a toxin known as microcystin through a process referred to as quorum sensing, which involves cell-to-cell communication. In this study, Quorum sensing signal molecules were experimentally added to the *Microcystis aeruginosa* culture, and the effects on cell density and microcystin concentration were evaluated. Within the concentration range of quorum sensing substances evaluated in this study, no significant effect was observed on cell growth. However, the amount of microcystin produced per cell was found to be affected.
These results suggest that quorum sensing may play a regulatory role in microcystin production independent of cell proliferation in *M. aeruginosa*.
**Keywords:** Harmful Algal Blooms; *Microcystis*; Microcystins (MCs); Quorum Sensing (QS)

## 1 Introduction

Water supply systems are essential facilities that ensure citizens have access to safe and clean water. In Japan, approximately 50% of drinking water sources are derived from dam reservoirs. However, in these reservoirs, the abnormal proliferation of cyanobacteria, known as harmful algal blooms (HABs), frequently poses a serious problem. Due to the semi-enclosed nature of dam reservoirs, which are characterized by limited water flow, nutrients tend to accumulate within these bodies. These conditions provide a favorable environment for the growth of cyanobacteria. Furthermore, cyanobacteria have been observed to flourish under conditions of elevated temperature; thus, an increase in water temperatures, as would be expected due to climate change, is likely to result in an escalation of the incidence of harmful algal blooms [1].

Among the various species of cyanobacteria, those belonging to the genus Microcystis are of particular concern because they produce microcystins (MCs), which are hepatotoxic compounds known to cause damage to humans and livestock [2, 3]. It has been reported that the production of MCs is influenced by a variety of factors, including environmental elements such as water temperature and nutrient levels. Additionally, the phenomenon of quorum sensing (QS), which refers to cell-to-cell communication, has been identified as a potential contributing factor. [4] In the context of QS, bacteria detect specific chemical signals, termed autoinducers (AIs), which are implicated in the sensing of population density and the subsequent regulation of physiological activities [5].

It has been suggested by preceding studies that the incorporation of acyl-homoserine lactone (AHL), a category of AI, into the culture medium may exert an influence on the proliferation of *Microcystis aeruginosa* and the concentration of MCs [6]. However, in these studies, relatively high concentrations of AHL were utilized, and the effects of low AHL concentrations on the growth and MCs production of M. aeruginosa remain to be elucidated.

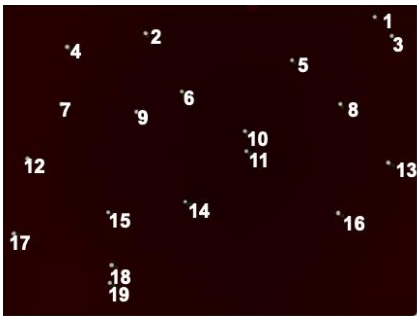

Fig. 1. Cell Counting

In this study, we investigated the effects of low concentrations of AHL on the growth of *M. aeruginosa* and on MCs production per cell.

## 2 Materials and methods

### 2.1 Culture Conditions

An axenic strain of *Microcystis aeruginosa* (NIES-843), provided by the National Institute for Environmental Studies, Japan, was cultured for 40 days in an incubator. The cultures were maintained in 200 mL of MA medium [7] at 20 °C under a light intensity of 30 μmol $m^{-2}$ $s^{-1}$ with a light–dark cycle of 9 h:15 h.

The QS signal molecule used in this study was N-(3-oxohexanoyl)-L-homoserine lactone (AHL; AdipoGen Co.). The final concentrations of AHL in the culture medium were adjusted to 0.5 mg $L^{-1}$ (n = 2) and 1 mg $L^{-1}$ (n = 3).

### 2.2. Measurement of Cell Density

Cell density was determined every one or two days. Micrographs of the cultures were taken using a cell counter plate (As One Co.) and a fluorescence microscope (Keyence).

The number of cells was counted using a BZ-X analyzer (Keyence) (Fig. 1).

Cell density (cells mL⁻¹) was calculated from the number of cells counted, the photographed area, and the depth of the cell counter plate according to the following equation:

$$\text{Cell density (cells/mL)} = \frac{\text{Number of cells}}{\text{Area of image} \times \text{Depth}} = \frac{\text{Number of cells (cells)}}{1.629 \times 10^{-4}\ \text{mL}}$$

### 2.3. Measurement of Microcystins Concentration

The measurement of MCs concentration was conducted following the method described in a previous study [8]. Samples (1 mL) were collected on days 12, 16, 20, 24, and 40 of the culture periods and subjected to freeze–thaw cycles. The samples were then diluted with 19 mL of ultrapure water, and an internal standard was added.

In the pretreatment process, MCs was oxidatively degraded into 2-methyl-3-methoxy-4-phenylbutyric acid (MMPB). The resulting MMPB was then extracted using solid-phase extraction, concentrated under a nitrogen gas stream, and quantified as the total MCs concentration. The measurement was performed using liquid chromatography–mass spectrometry (LC/MS).

## 3 Results and discussion

### 3.1. Results

The results of cell density measurements showed that *Microcystis aeruginosa* exhibited exponential growth until day 30 of cultivation under all conditions—without AHL, with 0.5 mg L⁻¹ AHL, and with 1.0 mg L⁻¹ AHL. After day 30, growth reached the stationary phase, and no significant differences in specific growth rate were observed among the treatments. This indicates that the AHL concentrations tested in this study did not affect the growth of *M. aeruginosa*.

The MCs content per cell (Fig. 2) showed that, on day 12, the AHL-added cultures produced less MCs per cell than the control without AHL. From day 16 onward, no differences in MCs content per cell were observed among the different AHL concentrations.

### 3.2. Discussion

Although AHL concentrations had no observable effect on the growth of *M. aeruginosa*, they appeared to influence MCs production per cell. The lower MCs content per cell observed on day 12 under AHL-added conditions suggests that the addition of AHL may have caused *M. aeruginosa* to perceive a higher cell density than the actual one, leading to the downregulation of MCs synthesis.

Previous studies have reported that MCs concentration per cell increases with rising cell density [4]. However, in this study, the MCs content per cell decreased as the culture period progressed, that is, as cell density increased. This discrepancy is likely due to differences in the initial cell densities between this study and previous reports. In earlier studies, cell densities ranged from 6.9 to 7.7 log cells mL⁻¹, whereas in this study, the range from day 12 to day 40 was 5.5–6.8 log cells mL⁻¹.

Since QS is a mechanism that regulates bacterial behavior depending on cell density, further studies across a wider range of initial cell densities are required to better understand how QS influences MCs production in *M. aeruginosa*.

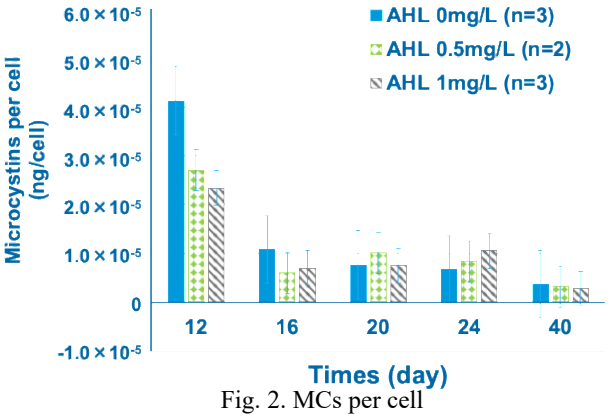

Fig. 2. MCs per cell

## 4 Conclusions

This study suggested that QS signaling molecules may influence MCs production at the cellular level in *Microcystis aeruginosa*. Although the AHL concentrations tested in this experiment did not affect cell growth, they appeared to alter MCs production per cell, implying that QS may regulate toxin synthesis independently of cell proliferation.

Future work will focus on conducting additional experiments under different environmental conditions, such as temperature and light intensity, as well as by varying the types of AHLs added. These efforts aim to further elucidate the relationship between QS and toxin production in *M. aeruginosa*.

## Reference

[1] Umeda N., Tomioka S., Relationship between water quality environmental factors and algal growth in reservoirs, *Journal of Hydraulic Engineering*, **51** (2007), pp. 1373–1378. (in Japanese)

[2] Carmichael W.W., et al., Human fatalities from cyanobacteria: Chemical and biological evidence for cyanotoxins, *Environmental Health Perspectives*, **109**[7] (2001), pp. 663–668.

[3] Nakamura T., et al., Accumulation of cyanotoxin microcystin-LR in dead ducks from Iso Fishing Port, Lake Biwa, *Japanese Journal of Ornithology*, **62**(2) (2013), pp. 153–165. (in Japanese)

[4] Wang S., et al., Cell density-dependent regulation of microcystin synthetase genes (*mcy*) expression and microcystin-LR production in *Microcystis aeruginosa* that mimics quorum sensing, *Ecotoxicology and Environmental Safety*, **220** (2021), pp. 1–8.

[5] Papenfort K., Bassler B.L., Quorum sensing signal–response systems in Gram-negative bacteria, *Nature Reviews Microbiology*, **14** (2016), pp. 576–588.

[6] Lamos-Samanamud G., et al., The role of quorum sensing in the development of *Microcystis aeruginosa* blooms: Gene expression, *Microorganisms*, **11** (2023), Article 383.

[7] Nishizawa K., Chihara M., *Methods in Phycological Research*, Kyoritsu Shuppan, (1979), pp. 294–305. (in Japanese)

[8] Tanaka Y., et al., A study on rapid determination of total microcystin by LC/MS/MS, *Journal of the Association of National Environmental Research Institutes*, **38**(3) (2013), pp. 140–144. (in Japanese)

# The in situ enrichment of low-density dispersed anammox bacteria and identification of its inhibitory and stimulatory metabolites

○Lan Wang [1,2]*, Yahui Wang [1, 2], Liangwei Deng [1, 2], Wenguo Wang [1,2]
[1]Biogas Institute of Ministry of Agriculture and Rural Affairs, Chengdu, Sichuan 610041, P. R. China
[2]Key Laboratory of Development and Application of Rural Renewable Energy, Ministry of Agriculture and Rural Affairs, Chengdu, Sichuan 610041, P. R. China
*E-mail: wanglan01@caas.cn

## Abstract

The anaerobic ammonium oxidation (anammox) process offers promise for the compliant treatment of wastewater. However, during the start-up phase of the anammox process, anammox bacteria typically exist in a low-density and dispersed state with low activity and growth rates, which makes in situ enrichment of anammox bacteria difficult. Therefore, enhancing the enrichment rate of anammox bacteria is critical. This study focused on low-density and dispersed anammox bacteria (with a cell concentration of $10^5$ cells/mL), simulating their in-situ enrichment. Through optimization of culture conditions, the rapid enrichment of anammox bacteria was successfully achieved. During the acclimation of low-density and dispersed anammox bacteria, the culture medium replacement frequency emerged as a key cultivation parameter affecting the activity and enrichment of anammox bacteria. As replacement frequency increased, anammox bacterial aggregates became larger, sludge exhibited a brighter red coloration, and specific activity improved. Meanwhile, the relative abundance (8.97%-9.91%) and relative expression levels (39.36%-41.38%) of anammox bacteria (Unclassified Kuenenia MAG_C55) were at least 1.85 times and 2.40 times those of other groups, respectively. The results of non-targeted metabolomics and batch experiments showed that timely medium replacement could alleviate the inhibition of anammox bacteria caused by metabolite accumulation. dCMP and GTP were the main inhibitory metabolites of anammox bacteria. When the concentration of exogenous dCMP and GTP was 1 mmol/L, the activity of anammox bacteria was severely inhibited. Metatranscriptomic and non-targeted metabolomic analyses indicated that when accumulated metabolites inhibited nitrogen metabolism and induced energy deficiency, anammox bacteria would successively up-regulate the expression of carbohydrate, amino acid, lipid, and nucleotide metabolism pathways to obtain energy for basic survival and growth. This study laid a theoretical foundation for the identification of inhibitory metabolites of anammox bacteria and provided a reference for the in-situ enrichment of anammox bacteria and the rapid start-up of the anammox process.

**Keywords:** Anammox; in situ enrichment; Metagenomic; Metatranscriptomic; Non-targeted metabolomic.

## 1 Introduction

After a long-term development, the anammox process has become increasingly mature. However, its large-scale popularization and application are still lacking. The reason lies in the difficulty of rapid enrichment and cultivation of anammox bacteria, due to its low growth rate and long doubling times (Zhang et al. 2017). Therefore, the start-up of the anammox process currently is difficult to completely depend on the direct inoculation of anammox granular sludge.

To address the challenge of no enough mature anammox granular sludge as inoculum, some researchers have developed an in situ anammox bacteria enrichment strategy to initiate the anammox process(Xu et al. 2023). Evidently, the operation of the anammox bacteria in situ enrichment system is unstable. Moreover, during first more than 100 days in situ enrichment period no any anammox activity can be detected and the relative abundance of anammox bacteria is also low.

Lots of studies indicated that the activity and growth rate of anammox bacteria are closely associated with their cell density and aggregation state. Strous et al. has demonstrated that anammox activity is only exhibited in the system when the cell density exceeds $10^{10}$-$10^{11}$ cells/mL, conversely, when the cell density is less than $10^6$ cells/mL, anammox activity is not present (Strous et al. 1999). Why the anammox reaction cannot be detected when the anammox bacteria exist in low cell density and free-living planktonic or dispersed state? How to shorten this no anammox reaction period? Whether are there some metabolic products inhibiting anammox activity? Exploring the best cultivation parameters of low density and dispersed anammox bacteria, identifying the metabolic products that inhibit the enrichment of anammox bacteria, and thereby promoting in situ enrichment and cultivation of anammox bacteria are of great significance for the popularization and application of the anammox process.

## 2 Materials and methods

### 2.1 Experimental Setup and Design

About 20mL suspend was inoculated in 100 or 150 mL serum bottle which was then filled by 80 mL culture medium for keeping the final culture volume of 100 mL, the MLVSS of $0.07 \pm 0.01$ g/L and the cell concentration of $8.5 \times 10^5$ cells/mL.

In order to determine the optimal culture parameters, we designed three experiments to optimize the carbon source supplemetation methods, oxygen removal methods and culture medium replacement frequency. (I) Optimization of Carbon Source supplementation methods: Eight treatment

groups were set up, including a blank control without sludge addition (CK), no carbon source supplementation (NCS), carbon source supplementation based on total nitrogen consumption at C/N ratios of 1:1 (C/N=1:1), 2:1 (C/N=2:1), and 4:1 (C/N=4:1), as well as fixed carbon source supplementation at 1 g/L every week (OW_C), every two weeks (TW_C), or every four weeks (FW_C). (II) Optimization of oxygen removal methods: Five treatments were included, namely a blank control without sludge addition (CK), no oxygen removal method was utilized (NOR), nitrogen gas purging ($N_2$), nitrogen gas purging combined with sodium sulfide as a deoxygenating agent ($N_2$+$Na_2S$), and nitrogen gas purging combined with L-cysteine hydrochloride as a deoxygenating agent ($N_2$+Cys). (III) Seven treatment groups were designed to optimize the Culture Medium Replacement Frequency (MRF), including replacing 50% and 25% medium every week (OW50 and OW25), replacing 50% and 25% medium every two weeks (TW50 and TW25), replacing 50% and 25% medium every four-weeks (FW50 and FW25), and no culture medium replacement throughout the experiment (NR).

## 3 Results and discussion

### 3.1 Optimization of cultivation parameters

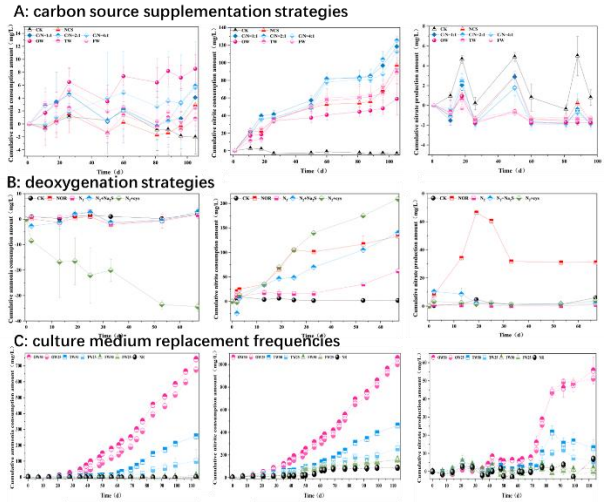


**Fig. 1. Differences in nitrogen metabolism under different carbon source supplementation strategies (A), deoxygenation strategies (B) and culture medium replacement frequencies (C).**

### 3.2 Differences in Key Nitrogen cycling Genes Induced by Medium Replacement Frequency

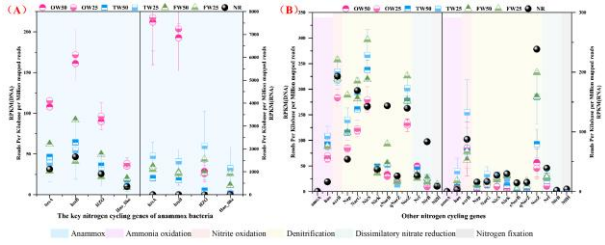

**Fig. 2 Differences in the relative abundance and relative expression levels of key genes involved in nitrogen metabolism (A) anammox-related genes, (B) genes related to other nitrogen metabolism pathways**

### 3.3 Microbial Community Differences Induced by Medium Replacement Frequency

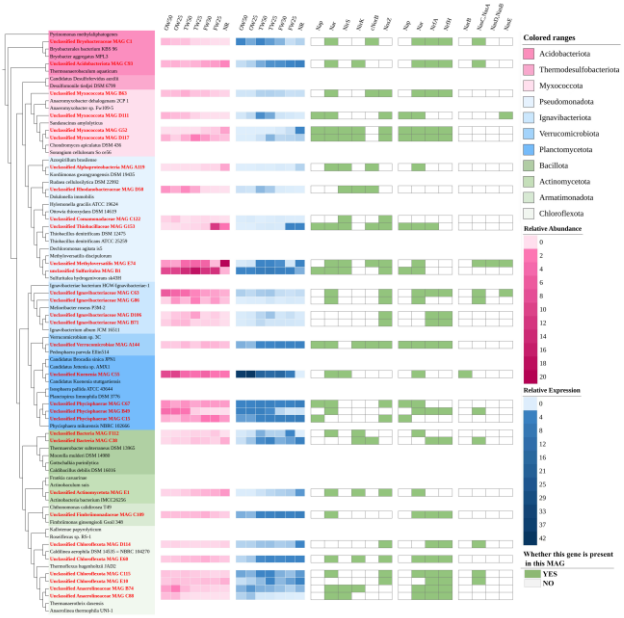

**Fig. 3 The relative abundance and expression levels of 31 high-quality genomes, along with their denitrification, dissimilatory nitrate reduction, and assimilatory nitrate reduction genes**

### 3.4 Metabolictes Differences Induced by Medium Replacement Frequency

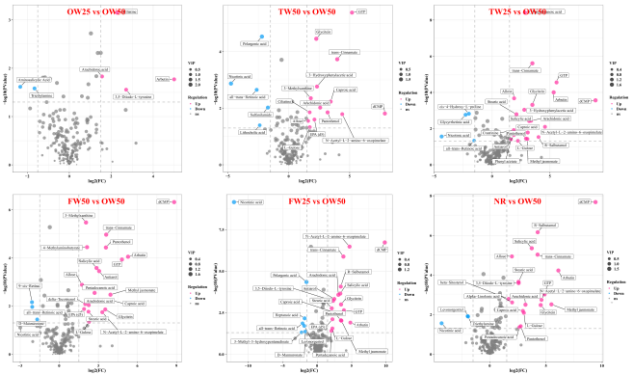

**Fig. 6. Differential metabolites under different medium replacement frequencies.**

## 4 Conclusions

(1) the replacement frequency of the culture medium was determined to be a key cultivation parameter affecting the enrichment of anammox bacteria.

(2) The accumulation of inhibitory metabolites dCMP and GTP of anammox bacteria was the key factor affecting enrichment and culturation.

## Reference

[1] Zhang, L. *et al*. (2017) Maximum specific growth rate of anammox bacteria revisited. Water research 116, 296-303.

[2] Xu, R. *et al*. (2023) Combination of sequencing batch operation and A/O process to achieve partial mainstream anammox: Pilot-scale demonstration and microbial ecological mechanism. Environmental science & technology 57(37), 13887-13900.

[3] Strous, M. *et al.* (1999) Missing lithotroph identified as new planctomycete. Nature 400(6743), 446-449.

# Enhanced Nutrient Removal via Small-Granule Sludge Formation in a Novel Continuous-Flow Reactor

○ Lifang LIU[1*], Wei-Kang QI[1] & Yu-You LI[2]
[1]College of Environmental Science and Engineering, Beijing University of Technology, Beijing 100124, China
[2]Department of Civil and Environmental Engineering, Tohoku University, Graduate School of Engineering, Miyagi 980-8579, Japan
[*]E-mail: l1978659045@163.com

## Abstract

Optimizing reactor designs and deciphering metabolic mechanisms are critical for advancing granular sludge applications. This study investigates granulation in a continuous self-circulating reactor (AcOA-Zier), focusing on transformation mechanisms and system stability. Over 290-day operation, the reactor achieved efficient sludge granulation, increasing the average particle diameter from 93 to 378 μm while maintaining sludge volume indices ($SVI_5$) below 55 mL/g. Granulation was driven by high-velocity liquid-sludge circulation (recirculation-to-influent ratio (R/I) >20, upflow velocity ($V_{up}$) >17 m/h), which maximized dissolved oxygen utilization while generating hydrodynamic shear and feast-famine conditions for granulation. Simultaneously, high removal efficiencies of 95% for COD and 90% for total nitrogen (TN) were achieved at an HRT of 6 h.

**Keywords:** Self-recirculation; Granular sludge; Self-aggregation; In-situ cultivation.

## 1 Introduction

Granular sludge technology leverages a compact microbial architecture to establish stratified aerobic, anoxic, and anaerobic zones within individual granules under oxygenated conditions. This unique structure enables simultaneous removal of organic carbon, nitrogen, and phosphorus while reducing footprint by 70% and operational costs by 48% compared to conventional activated sludge systems [1]. These advantages position granular sludge as a transformative solution for sustainable wastewater treatment.

Despite successful implementation in sequencing batch reactors, operational complexity continues to inhibit widespread adoption. Continuous-flow reactors offer inherent operational simplicity and infrastructure compatibility but face fundamental barriers: extended granulation timelines exceeding three months, early-stage biomass washout compromising nitrification efficiency, and limited availability of seed sludge. These unresolved challenges highlight the critical need for innovative reactor designs that enable rapid granulation with robust biomass retention.

This study pioneered a novel self-circulating upflow Zier reactor for in situ granular sludge cultivation. We systematically evaluated granulation feasibility, assessed long-term pollutant removal stability, and elucidated the underlying mechanisms governing granule formation.

## 2 Materials and methods

The AcOA-Zier reactor comprised an aeration column (Zier-Ac), an oxic column (Zier-O), and an anoxic column (Zier-A). These three columns were connected in series via recirculation tubes to form a closed-loop system with a combined effective volume of 22.5 L. Seed sludge was inoculated from a wastewater treatment plant in Shandong Province (China) with an average sludge size of 93.1 μm.

The pH, temperature and dissolved oxygen (DO) were monitored daily using a portable multi-parameter meter (WTW Multi3620, Germany). Conventional indicators were measured using APHA Standard Methods.

## 3 Results and discussion

During initial reactor operation, flocculent sludge predominated, with only 5.5% of sludge particles exceeding 200 μm (Figs. 1a-b). Granule development increased the average particle size from 93.1 μm to 342 μm on day 178, with 84.1% exceeding 200 μm. This small-particle granular system enhanced specific surface area, minimized fragmentation, and ensured long-term operational stability.

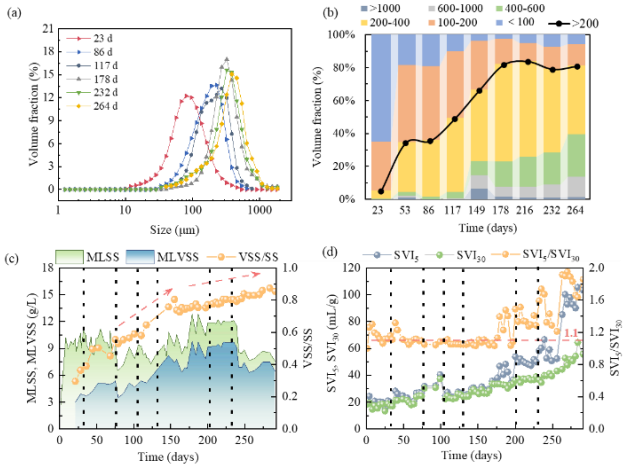


**Fig. 1. Characterization of sludge properties and performance. (a) Sludge size dynamics; (b) Temporal variations in particle size fractions; (c) Biomass indicators: MLSS, MLVSS, and VSS/SS ratio; (d) Settling performance indicators: $SVI_5$, $SVI_{30}$, and $SVI_5/SVI_{30}$ ratio.**

During initial operation, average mixed liquor suspended solids (MLSS) concentration were 10.2 g/L (fluctuations due to high flow velocities). The volatile-to-total suspended solids ratio (VSS/SS) was 0.4 (Fig. 1c), while sludge volume indices at 5 and 30 minutes ($SVI_5$, $SVI_{30}$) averaged 19 and 22

mL/g, respectively (Fig. 1d), indicating minimal impact of carbon-free influent on settling. Following carbon source introduction (Phases II–V), MLSS increased progressively, stabilizing at 12 g/L after day 200. Phase III reduction of solids retention time (SRT) from 100 to 35 days marginally decreased sludge concentration. Concurrently, VSS/SS rose to 0.9, indicating elevated organic content. $SVI_5$ and $SVI_{30}$ increased to 40 and 36 mL/g, demonstrating enhanced settling performance. Reducing hydraulic retention time (HRT) from 7.5 to 6 h (day 176) increased $SVI_5/SVI_{30}$ to 1.32, indicating sedimentation sensitivity to loading conditions.

Bioreactor operation induced a gradual sludge transformation from flocculent to compact granules with smooth surfaces and light-yellow coloration. Scanning electron microscope (SEM) imaging revealed porous granule surfaces densely colonized by coccoid, rod-shaped, and filamentous bacteria (Fig. 2a). These microbial communities facilitate nutrient degradation and structural integrity maintenance. Granule interiors contained rod-shaped and spherical microorganisms interspersed among cavities (Fig. 2b), indicating substrate and DO penetration enabling internal microbial growth under shifting reactor conditions.

To investigate microbial stratification, mature granules (day 290) were sectioned and stained for ammonia-oxidizing (AOB) and nitrite-oxidizing bacteria (NOB). Both populations were distributed throughout the granules, though AOB fluorescence intensity significantly exceeded that of NOB (Fig. 2c), demonstrating partial nitrification potential. Abundant cavities facilitated nutrient and gas exchange between granule interior and bulk liquid.

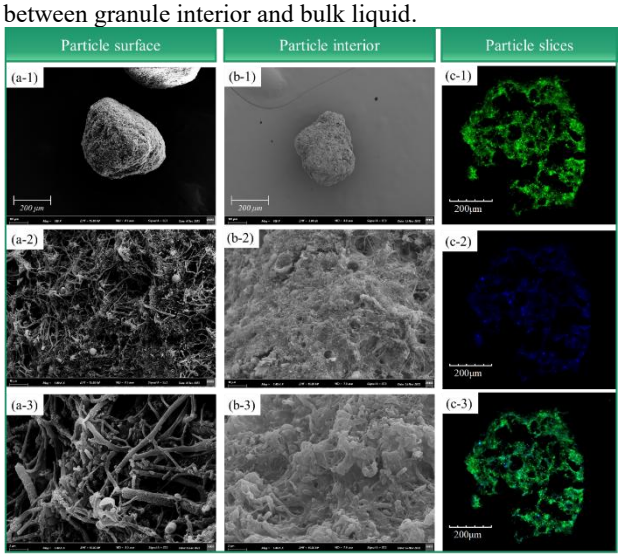


**Fig. 2. Microstructural and functional characterization of granules. (a) SEM image of granule surfaces; (b) SEM image of granule interiors; (c) CLSM image: AOB stained in green and NOB stained in blue.**

The AcOA-Zier reactor maintained continuous operation for 290 days. In phase I, influent $NH_4^+$-N (200 mg/L) was reduced to <3 mg/L effluent, facilitating autotrophic bacterial domestication (Fig. 3c). In phase II, carbon source addition adjusted influent concentrations to 50 mg/L $NH_4^+$-N and 800 mg/L COD, achieving 98% COD and 99% TN removal (Figs. 3c-e). Reduced oxygen demand enabled HRT reduction from 39 to 15 h. Phase III further decreased COD to 400 mg/L and HRT to 7.5 h, maintaining >96% TN/COD removal under steady state. Subsequent phases (IV–V) modulated influent conditions, consistently yielding approximately 1 mg/L $NH_4^+$-N and below 40 mg/L COD effluent (99% $NH_4^+$-N; 95% COD removal). TN removal efficiency exhibited a positive correlation with influent C/N ratio, exceeding 90% at C/N >4 but declining to 80% at C/N of 3 (Figs. 3d-e). Sludge granulation enhanced treatment capacity, reducing HRT from 15 to 5 h while increasing nitrogen loading rate (NLR) from 0.1 to 0.6 kg-N/m³/d and organic loading rate (OLR) to 3.0 kg-COD/m³/d (Figs. 3d-e). TN removal remained robust throughout, with no nitrification deterioration from sludge washout, attributable to the AcOA-Zier process's distinct operational mode: optimized oxygen supply-demand balance, high-speed wastewater circulation, and established aerobic-to-anoxic DO gradients.

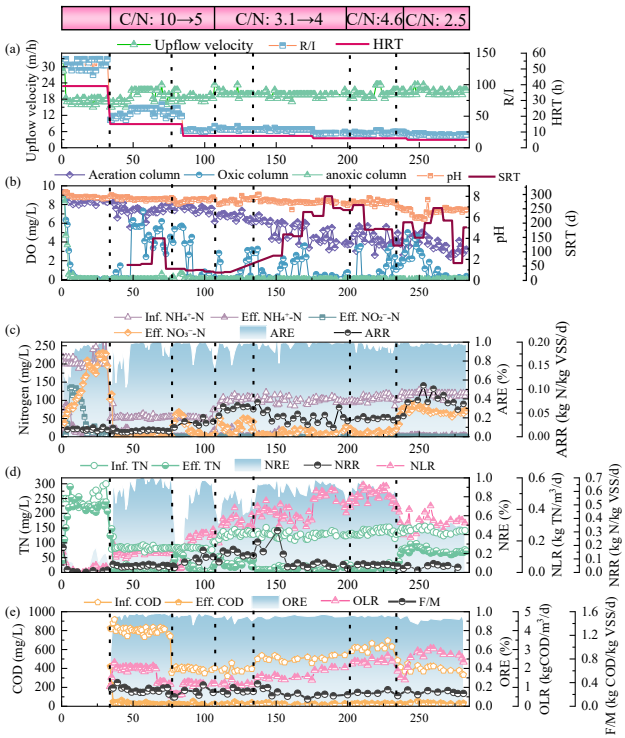


**Fig. 3. Bioreactor operational performance indicators. (a) Temporal variations in $V_{up}$, R/I and HRT; (b) Monitoring of DO concentration, pH and SRT; (c) Dynamics of nitrogen transformation; (d) TN removal efficiency; (e) COD removal efficiency.**

## 4 Conclusions

This study demonstrates stable activated sludge-to-granular sludge transformation, producing mature granules with an average diameter of 378 μm while maintaining excellent settling characteristics ($SVI_5$ <55 mL/g). Granulation was primarily driven by aeration-induced high-velocity circulation, generating optimal hydraulic shear and feast-famine conditions. Throughout 290 days of continuous operation, COD and TN removal efficiencies remained consistently high at 95% and 90%, respectively, at an HRT of 6 h.

## Reference

[1] Y.V. Nancharaiah, M. Sarvajith, Aerobic granular sludge process: a fast growing biological treatment for sustainable wastewater treatment, Current Opinion in Environmental Science & Health. 12 (2019) 57-65.

# The enhancement effect and mechanism of air mixing on biogas production performance in anaerobic digestion

○Hongnan Yang[1,2*], Liangwei Deng [1,2] & Xinwei Li [1,2]
[1]Biogas Institute of Ministry of Agriculture and Rural Affairs, Chengdu 610041, PR China.
[2] Key Laboratory of Development and Application of Rural Renewable Energy, Ministry of Agriculture and Rural Affairs, Chengdu 610041, PR China.
[*]E-mail: yanghongnan@caas.cn

## Abstract

Air mixing, a novel agitation method using air as the gas source in anaerobic digestion (AD), was investigated to assess its impact on process performance. The results demonstrated that air mixing enhanced methane production, improved hydrolysis efficiency, and reduced hydrogen sulfide ($H_2S$) content in biogas. Under optimal conditions, air mixing significantly increased methane yield compared to conventional mixing methods. The enhancement is attributed to improved mass transfer, the creation of a transient microaerobic environment, the enrichment of functional microbial communities, and the upregulation of hydrolytic enzymes. These findings confirm that air mixing is a sustainable and efficient mixing strategy for AD systems treating high-solids waste and animal wastewater.

**Keywords:** Anaerobic digestion; Air mixing; Methane production; Microaeration; Microbial community.

## 1 Introduction

Anaerobic digestion (AD) is a widely adopted technology for organic waste treatment and renewable energy recovery [1]. Mixing is a critical operational factor that influences mass transfer, substrate-microbe contact, and overall digester performance [2]. Conventional mixing methods—mechanical, hydraulic, and biogas mixing—each have limitations, such as high energy consumption, dead zones, and reliance on sufficient biogas production [3]. Biogas mixing, though energy-efficient, is often impractical in on-farm digesters with low biogas output [4].

Recent studies have explored the tolerance of AD systems to trace oxygen, leading to the concept of micro-aeration [5–7]. Building on this foundation, this study proposes and evaluates air mixing—using air instead of biogas for agitation—to overcome the limitations of biogas mixing while leveraging the benefits of microaeration. The overall goal of this work was to assess the feasibility of air mixing and evaluate its effects on the AD process based on methane production efficiency, hydrolysis, and microbial community structure.

## 2 Materials and methods

### 2.1. Reactors and experimental setup

Lab-scale reactors (1–4.5 L working volume) were used in batch and semi-continuous modes [4,8,9]. Air was introduced via a peristaltic pump and aeration disc at the bottom. Comparisons were made with biogas mixing, mechanical mixing, and no mixing under the same power input (~5 W/m³) [4]. Full-scale validation was conducted in a 2000 m³ continuous stirred tank reactor (CSTR) treating swine wastewater [8].

### 2.2. Substrate and inoculum

Swine wastewater and cow manure were used as substrates, with total solids (TS) concentrations ranging from 6% to 21.8% [4,8,9]. Inoculum was obtained from operational anaerobic digesters [4]

### 2.3. Analytical methods

Biogas production and composition ($CH_4$, $CO_2$, $H_2S$) were measured using gas flowmeters and gas chromatography. TS, VS, VFAs, crude fiber, fat, and protein were analyzed using standard methods. Microbial community analysis was performed via 16S rRNA sequencing. Hydrolytic enzyme abundance was predicted using PICRUSt2 and the KEGG database.

## 3 Results and discussion

### 3.1. Enhanced biogas and methane production

Air mixing significantly increased cumulative methane production by 6–20% compared to controls [4,8,9]. The optimal aeration intensity was 37.5–66.7 mL/L·min, with a mixing time of 1.5–2 min [4,8]. Methane production decreased when mixing time exceeded 3 min due to reduced effective methane production time (EMPT) [8].

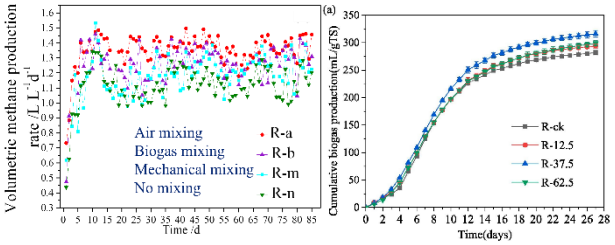


**Fig. 1. Volumetric methane production rate from four anaerobic digesters and variation of cumulative biogas production under different air mixing intensities. R-ck represents no mixing; R-12.5, R-37.5 and R-62.5 represent the experimental groups with air mixing intensity of 12.5, 37.5 and 62.5 mL/(L·min), respectivelys**

### 3.2. Improved hydrolysis and carbon recovery

Air mixing enhanced the hydrolysis of macromolecular substrates (proteins, carbohydrates, fiber, and fat) by 5–34% [4,9]. Carbon recovery in the form of methane increased by 6–7%, indicating more efficient conversion of organic carbon into biogas [9].

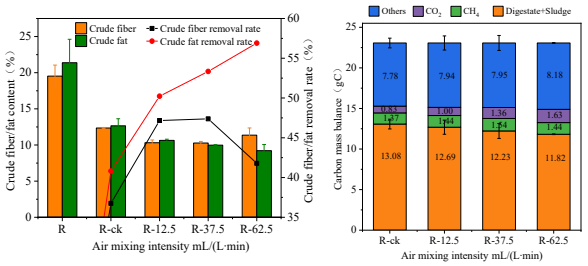


**Fig. 2. Crude fat/fiber content and crude fat/fiber content removal efficiency and carbon mass balance (gC) under different air mixing intensities.**

### 3.3. Microbial community shifts

Air mixing enriched:

Sulfide-oxidizing bacteria (SOB) such as *Magnetospirillum*, enhancing $H_2S$ removal [9].

Syntrophic acetate-oxidizing bacteria (SAOB) like *Synergistaceae*, facilitating acetate degradation [14].

Acetoclastic methanogens (*Methanosaeta*), which dominated under microaerobic conditions [4,9].

Hydrogenotrophic methanogens (*Methanospirillum*) also increased, supporting syntrophic relationships [4].

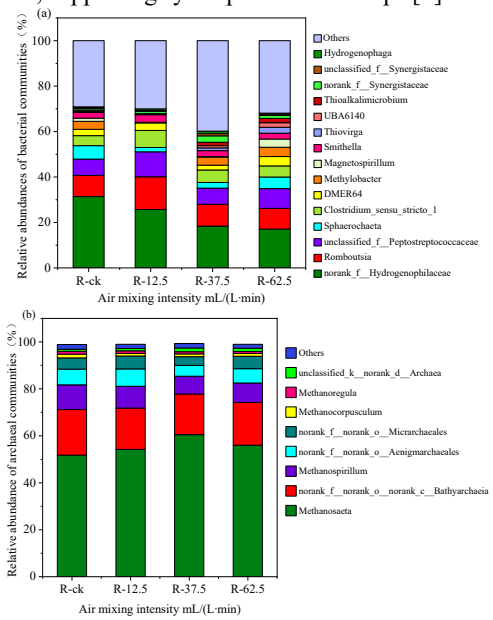


**Fig. 3. The relative abundance of bacteria at the genus level(a) and the relative abundance of archaea at the genus level(b) under different air mixing intensities.**

### 3.4. Enzymatic activity enhancement

PICRUSt2 prediction revealed higher abundance of hydrolytic enzymes (e.g., cellulase, α-amylase, triacylglycerol lipase) under air mixing, accelerating the degradation of complex organics [9]

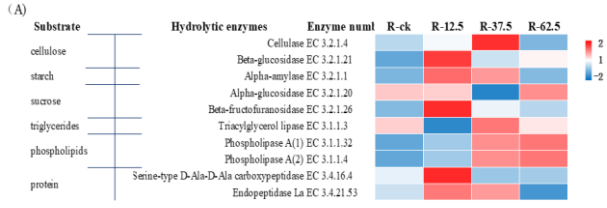


**Fig. 4. Schematic diagram of predicted hydrolytic enzymes related to degradation of macromolecules under different air mixing intensities.**

### 3.5. Mechanistic contributions

The improvement in methane production was attributed to:

Improved mass transfer (62.9%) [4] and Microaerobic reactions (37.1%), including oxidative degradation of inhibitors and enhanced hydrolysis [4,9].

### 3.6. Full-scale validation

A full-scale CSTR operated stably for over one year with air mixing, demonstrating practical applicability [8]. Biogas production remained consistent, and no blockages or operational failures were reported.

## 4 Conclusions

Air mixing is a viable and effective mixing strategy for anaerobic digestion systems, particularly for high-solids waste and animal wastewater. It enhances methane production, promotes hydrolysis, reduces $H_2S$, and enriches beneficial microbial communities. The optimal operational parameters—aeration intensity of 37.5–66.7 mL/L·min and mixing time of 1.5–2 min—should be maintained to avoid oxygen inhibition. Air mixing represents a promising alternative to conventional mixing methods, combining the benefits of efficient agitation and microaeration in a single process.

## Reference

[1] Deng, L., Liu, Y., Zheng, D., Wang, L., Pu, X., Song, L., Wang, Z., Lei, Y., Chen, Z., Long, Y., 2019. Application and development of biogas technology for the treatment of waste in China. Renew. Sustain. Energy Rev. 70, 1019–1028.

[2] Kariyama, I.D., Zhai, X., Wu, B., 2018. Influence of mixing on anaerobic digestion efficiency in stirred tank digesters: A review. Water Res. 143, 503–517.

[3] Latha, K., Velraj, R., Shanmugam, P., Sivanesan, S., 2019. Mixing strategies of high solids anaerobic co-digestion using food waste with sewage sludge for enhanced biogas production. J. Cleaner Prod. 210, 388–400.

[4] Yang, H., Deng, L., 2020. Using air instead of biogas for mixing and its effect on anaerobic digestion of animal wastewater with high suspended solids. Bioresour. Technol. 318, 124047.

[5] Botheju, D., Bakke, R., 2011. Oxygen effects in anaerobic digestion-a review. Open Waste Manage. J. 4, 1–19.

[6] Nguyen, D., Khanal, S.K., 2018. A little breath of fresh air into an anaerobic system: How microaeration facilitates anaerobic digestion process. Biotechnol. Adv. 36(7), 1971–1984.

[7] Chen, Q., Wu, W., Qi, D., Ding, Y., Zhao, Z., 2020. Review on microaeration-based anaerobic digestion: State of the art, challenges, and prospectives. Sci. Total Environ. 710, 136388.

[8] Yang, H., Deng, L., Wu, J., Wang, W., Zheng, D., Wang, Z., Liu, Y., 2021. Intermittent air mixing system for anaerobic digestion of animal wastewater: Operating conditions and full-scale validation. Bioresour. Technol. 335, 125304.

[9] Li, X., Deng, L., Li, F., Zheng, D., Yang, H., 2023. Effect of air mixing on high-solids anaerobic digestion of cow manure: Performance and mechanism. Bioresource Technology 370, 128545.

# Methane Extraction from Anaerobic Digestion of Rice Straw: Opportunities and Obstacles

○ HUQE Farhana[1*] & LI You Yu[2]
[1]Department of Civil and Environmental Engineering, Graduate School of Engineering, Tohoku University, Miyagi, Japan.
[2]Department of Civil and Environmental Engineering, Graduate School of Engineering, Tohoku University, Miyagi, Japan.
[*]E-mail: huqe.farhana.d1@tohoku.ac.jp

## Abstract

Rice straw is an extensively potential biomass for biogas production through anaerobic digestion [1]. Biomethanation of rice straw is a comprehensible way for energy production as well as for waste management. But the low biodegradability of rice straw is a major obstacle for achieving methane at a satisfactory level. Moreover, the anaerobic digestion of rice straw often undergoes with some other defiance such as high retation time, unbalanced nutrients and lack of productive inoculum[2]. These challenges can be overcome by adopting some potential strategies via pretreatment of rice straw, co-digestion with other raw materials such as food wastes and cattle manure, selection of effective inoculum sources, optimizing the process parameters [3,4,5,6]. Furthermore, optimized design of anaerobic digester plays a vital role for the digestion of rice straw. Proper mixing of the raw materials and regular removal of digested sludge can be the solutions to reduce such dead zones inside digester[7]. These strategies still require standardization for the enhancement of biodegradability of rice straw to obtain adequate amount of methane. Further exploration of diverse inoculum sources and co-digestion is required for the commercialization of rice straw.

**Keywords:** rice straw; anaerobic digestion; pretreatment; optimization.

## Reference

[1] Bentsen, N.S., et al, Agricultural Residue Production and potentials for energy and materials services, Prog. Energy Combust. Sci. 40 (2014), 59-73.

[2] Liu, Z., et al, Energy from combustion of rice straw: status and challenges to China. Energy Power Eng. 03 (2011), 325-33.

[3] Sari, F., et al, Enhanced of Biogas Production from Rice straw with Various Pretreatments: A Review, Waste Technol. 2 (2014), 17-25

[4] Zhao, M.,et al, Synergistic and pretreatment effect on anaerobic co-digestion from rice straw and municipal sewage sludge. BioResources. 9 (2014), 5871-5882.

[5] Deng, Y., et al, Co-inoculation of cellulolytic rumen bacteria with methanogenic sludge to enhance methanogenesis of rice straw. Int. Biodeterior. Biodegrad. 117(2017),224-235.

[6] Mussoline, W., et al, Enhanced methane production from rice straw co-digested with anaerobic sludge from pulp and paper mill treatment process. Bioresour. Technol. 148(2017b), 135-143.

[7] Rahman, K.M., et al, Evaluating the potential of rice straw as a Co-digestion feedstock for biogas production in Bangladesh evaluating the potential of rice straw as a Co-digestion feedstock for biogas production in Bangladesh. J. Adv. Comput. Sci. Technol. 4 (2017), 8-14.

# Evaluation of carbon benefit in the whole life cycle of mine water recycling

○ Xuan Wang[1*], Jin Yuan[1] & Xin Sui[1]

[1] Department of Environmental Science and Engineering, Taiyuan University of Technology, Taiyuan 510275, China.

[*]E-mail: wangxuan0521@link.tyut.edu.cn.

**Abstract**

Climate change and water scarcity are two global challenges. Coal mining is the main source of carbon emissions. The utilization of mine water resources and its carbon footprint calculation are of paramount significance in promoting water conservation and carbon reduction in mining areas. However, research on the carbon footprint and other environmental indicators across the life cycle of mine water in developing countries, such as China, remains limited. This study focuses on a representative mine water resource utilization system in China and describes the method used to calculate carbon emissions associated with mine water resource utilization throughout its life cycle. Based on life cycle assessment (LCA) and using on-site investigations and analysis of environmental indicators, the study evaluates the environmental impacts at different stages of mine water resource utilization, identifies key processes, and provides some improvement suggestions. The research results indicate that the life cycle carbon emissions of mine water amount to 2.35 kg CO2 eq per 1 $m^3$. The water extraction stage highlights the potential environmental impact, including water use (WU) and ozone depletion potential (ODP). By substituting traditional power generation methods and incorporating intelligent dosing equipment to optimize chemical usage, the global warming potential (GWP) has been decreased by over 90%, and the GWP of chemical consumption has also witnessed respective reductions of 21.5% and 10.1%. This study can serve as a basis for calculating carbon emissions in mining areas and formulating strategies to reduce their environmental impact.

**Keywords:** mine water; resource utilization; carbon emissions; LCA; environmental indicators

# PFAS in Aquatic Environments: A Growing Concern and the Role of Advanced Oxidation Processes in Remediation

○ Adriana LEDEZMA-ESTRADA[1]
[1]Department of Civil and Environmental Engineering, Tohoku University, Graduate School of Engineering, Miyagi 980-8579, Japan.
*E-mail: aledezmaes@gmail.com.

## Abstract

Per-and Polyfluoroalkyl Substances (PFAS) are anthropogenic substances that started to being used since 1940's. Since then, about 5000 different compounds using the PFAS as a backbone structure have been synthetized. The main characteristic of such compounds is the strong bond between the Carbon and Fluor elements, which confers thermal stability and chemical inertness. Therefore, PFAS compounds are very stable compounds that persist in the environment because they cannot be oxidized by weather conditions or microbial activity, and they are known as a "forever chemicals". In particular, these substances have been used as firefighting agents, such as the aqueous film-forming foams (AFFFs) in facilities that use flammable liquids, such as fuel. AFFFs are storage as a concentrate that needs to be mixed with water to create foam, as a result after using they end up mixed with water and turning into a pollutant in aquatic environments. The most common way to avoid their entrance into the environment is by absorbing the foam with absorbent pads but that is not enough. A promising alternative is the use of Advanced Oxidation Processes (AOPs), which produce free radicals that can react with strong chemical bonds to break the molecule into more bridgeable substances.

**Keywords:** Per-and Polyfluoroalkyl Substances (PFAS); aqueous film-forming foams (AFFFs); Advanced Oxidation Processes (AOPs).

## 1 Introduction

In the 1930-1940 the companies 3M and Dupont began the discovery and synthesis of fluoropolymers and fluorochemicals, they found that such compounds have an exceptional stability and resistance to heat, water, and oils. 3M started to add fluorinated surfactants (early PFAS) to protein firefighting foams to enhance spread-ability, until 1960 when 3M finally developed the aqueous film-forming foams (AFFFs), a complete inorganic product.

AFFFs are used in facilities where Class B fires are likely to happen due to flammable liquid fires, such as fuels like gasoline, diesel, jet fuel, etc. are used. Therefore, AFFFs are currently used in airfields, oil refineries and petrochemical plants, fuel storage facilities or tank farms, marine and offshore platforms, industrial facilities that use flammable solvents, and on smaller scale in fire departments and transport hubs including fueling stations.

AFFFs are used worldwide, but especially in military facilities with airfields in developed countries. For many years, its use was not strictly regulated because their effects on the environment and public health were unknown. It was until 1980s that scientists noticed PFAS contamination in water near manufacturing plants, which suggested that they were not easily degraded in the environment. Then, 1990s blood tests of workers and nearby residents showed PFAS presence which confirm their ability to bioaccumulate in living organisms.

Further investigations in the 2000s showed PFAS ability to undergo long-range transport as they have been found in various matrices, like arctic ice or wildlife, where PFAS were not manufactured or used. As a result of these discoveries scientist and regulatory bodies started to recognize PFAS as a persistent organic pollutant (POP) that bioaccumulate, and they started to be called as the "forever chemicals".

Further investigations found that the main vector of the PFAS to enter the environment was through as a water pollutant because conventional water treatment techniques are unable to remove them.

### 1.2 PFAS main point of entrance to the environment.

The two main sources of PFAS as water pollutants are the manufacturing industry and the activities related to the use of firefighting foams. In the first case, regular wastewater treatment fails to remove PFAS from water effluents. As for the AFFF, the problem is broad because it involves not only their use but their transportation, storage and accidental release due to fire false alarms, training or poor management.

### 1.3 How does AFFF works environment.

The AFFF is stored as a concentrated liquid in a tank located in the facility that needs to be protected from fire. To activate the AFFF to produce the foam, it has to be mixed with water, usually in a ratio of 3% -6% AFFF and 94-97% of water. Therefore, the AFFF tanks is connected to a system of water pipes that will provide water and will act as mixing container. Then, the pipes and nozzles discharge the foam in the facility.

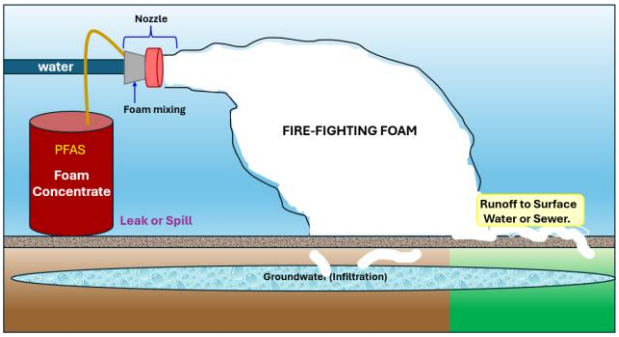


**Fig. 1 Release of fire-fighting foam**

### 1.4 Environmental and Health Concerns

Even though since the 2000s the PFAS were considered POP, the regulation was not very clear mostly because the 75% of the AFFF produced are used in the military industry, the other 25% is used for oil refineries, airports, tank farms and fire stations.

It was until independent associations around the world started conducting their own environmental and health screen surveys that finally proved the impact of the PFAS on the environment and the impact on human health. For instance, in Japan, civil associations in conjunction with independent researchers analyzed water samples from waterbodies and tap drinking water located near military bases, in addition to blood test in children, adults and elderlies. These results show PFAS are present in the environment and confirm their bioaccumulation ability in people's bodies.

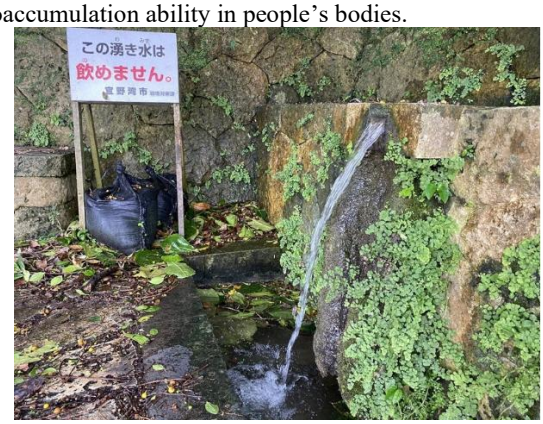


**Fig. 2 Chunna-ga, Ginowan, Okinawa. Sept 5 2022. (Courtesy of Yuya Miyagi)**

Further investigations conducted by national entities found that long-chain PFAS cannot be excreted from the body, while short-chain PFAS could be excreted from a healthy organism in function of the accumulated concentration. It was also found that PFAS are carcinogenic substances, hormone disruptors, hepatoxic, and immunological disruptors.

### 1.5 Strong Regulation and Phaseout Requirements

It took almost 20 years and many investigations around the world to finally recognize the PFAS huge impact on the environment and human health. It was until 2021 that the EPA issued a final guidance regulating the AFFF. The first step was to phase out AFFFs that contain long-chain PFAS from 16-C to 8-C or less, this is an effort that is still on going. At least now, any AFFF containing log-chain PFAS cannot be used.

In Japan, starting from October 2024 AFFFs containing PFAS have been starting to get replaced with Fluorine-Free-Foam (F3). While the United States has the deadline to replace all AFFF with long-chain being replaced with the new F3.

### 1.6 Challenges to Dispose or Treat PFAS

PFAS elimination is still a challenge either when AFFF are concentrated or mixed with water.

Currently, the methodology used to dispose concentrated AFFF is through incineration. The liquid is adsorbed with adsorbent pads or activated carbon and then incinerated. But, it becomes a challenge when the AFFF is mixing with water, the incineration process becomes very expensive and thus usually this mixture is kept in sealed drums that are store for further disposal.

### 2.0 Advanced Technologies

Due to the great environmental concern PFAS have, different technologies have been tried at laboratory scale, including physical, chemical and biological process such as nanofiltration (NF), Reverse osmosis (RO), biological degradation (BD), chemical oxidation, adsorption. Anion exchange, sono-chemical treatment, etc.

It has been found that adsorption and processes involving free radicals have been the more effective to oxidize PFAS than common treatments. However, those processes have a high operational cost either for the material that is required or the energy and special requirement the processes demand.

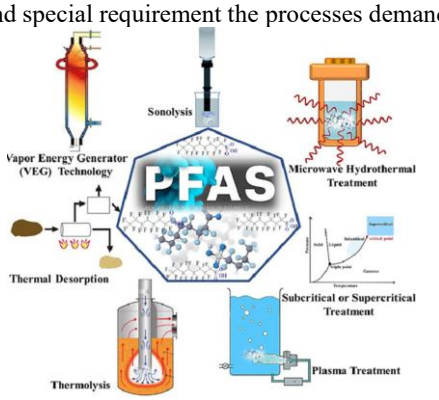


**Fig. 3 Recent advance on PFAS degradation, Author Sanny Verma.**

### 2.1 Advanced Oxidation Process (AOPs)

AOPs are a physicochemical process that involves the generation of highly reactive agents such as free radicals, primarily hydroxyl radical (OH).

On of the most common and effective AOP is based on the electro-Fenton reaction, an electrochemical reaction, where water undergoes an electrolysis catalyzed by iron (Fe) ions to produce hydroxyl radicals. The efficiency of the process depends on the electrode material and pollutant concentration. It has been found that using an activated carbon fiber cathode, which has low cost, enhances the production of oxygen reactive compounds during the electro-Fenton process. The cost limitation of this AOP is the energy demand, because the process requires electricity to function, However, several studies have been conducted using solar energy.

The AOP could be used as pre-treatment to oxidize the PFAS, and later the process could be switch to common wastewater treatment or to a biological treatment to yield it complete mineralization.

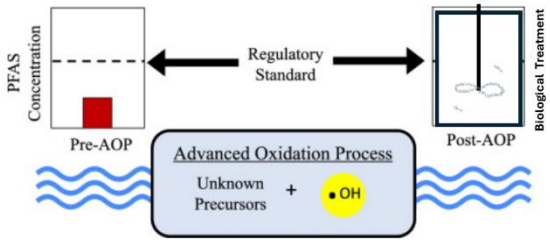


**Fig 4. AOPs as pre-treatment.**

**3.0 Conclusion**: AOPS are feasible alternative to pretreat PFAS in water. Regardless of the PFAS being phased out their presence will persist in the environment for long time, thus new technologies should be implemented.

**References:** PFAS chemical degradation strategies: insights into the underlying mechanisms. Brian D Etz, Engineering, Vol 42, Dec 2023. 1000956.

# Construction and Performance Enhancement of Photocatalysis–Microbe Coupled CO2 Fixation Systems

○Hongwei Zhang [1,2*], Xinru Jiang [1,2], Xiaolei Guo [1,2], Yuhang Shao [1,2], Liangwei Deng [1,2]
[1]Biogas Institute of Ministry of Agriculture and Rural Affairs, Chengdu 610041, PR China.
[2] Key Laboratory of Development and Application of Rural Renewable Energy, Ministry of Agriculture and Rural Affairs, Chengdu 610041, PR China.
*E-mail: zhw9590@163.com

## Abstract

Coupling photocatalysis with autotrophic microorganisms enables renewable-energy-driven $CO_2$ fixation under mild conditions. Here we construct a stable photocatalysis–biohybrid system (PBS) by integrating a visible-light-responsive semiconductor ($ZnIn_2S_4$) with Methanosarcina barkeri for methanogenesis and with Cupriavidus necator for single-cell protein (SCP) production. Compared with widely used CdS-based PBSs that suffer from photocorrosion, $ZnIn_2S_4$ enhances solar utilization while suppressing self-deactivation, thereby improving system robustness. In the $ZnIn_2S_4$@M. barkeri system, methane formation peaks at a catalyst dose of 2 mg, affording 0.97 μmol $CH_4$—9-told that of the pure-culture control (0.10 μmol). For SCP, introducing an electron mediator (Ension Y) into the $ZnIn_2S_4$@C. necator system increases optical density by 8% (48 h) and soluble cellular protein by 20% (24 h), accompanied by a higher live-cell fraction. These results demonstrate a generalized strategy for light-driven $CO_2$ conversion to fuels and proteins in stable biohybrids.

**Keywords:** Extracellular electron transfer; photocatalysis; biotic-abiotic interface; intracellular methanogenesis; $CO_2$ conversion.

## 1 Introduction

Renewable-energy-assisted $CO_2$ fixation via chemical and biological routes has attracted broad interest for converting $CO_2$ into methane, acetate, ethanol, and other value-added products. Purely chemical routes often require high energy input, whereas purely biological routes can be slow or less selective. Photocatalysis–biohybrid systems (PBSs) combine the strengths of both, enabling light-driven $CO_2$ conversion with enhanced efficiency and selectivity. Although CdS-based PBSs exhibit favorable biocompatibility and visible-light activity, their intrinsic photocorrosion undermines durability and safety. To address this, we employ a more stable semiconductor, $ZnIn_2S_4$, and build two PBS platforms: (i) $ZnIn_2S_4$@M. barkeri for methanogenesis and (ii) $ZnIn_2S_4$@C. necator for autotrophic SCP production, with the latter further enhanced by an electron mediator. Our design hypothesis is that $ZnIn_2S_4$ can supply photogenerated electrons to microbes through $H_2$-mediated and/or extracellular electron transfer (EET) pathways, while resisting self-corrosion to sustain long-term operation.

## 2 Materials and methods

### 2.1 Construction of PBS.

$ZnIn_2S_4$ photocatalysts with controlled structures were synthesized by a temperature-controlled hydrothermal method. M. barkeri (DSM 800; China Collection of Anaerobic Microorganisms, Chengdu) was inoculated into 50 mL heterotrophic medium at 37 °C (1:5 inoculation). At mid-log phase ($OD_{600}$ ≈ 0.2), 2 mg $ZnIn_2S_4$ was added. After 12 h culturing at 180 rpm, the $ZnIn_2S_4$@M. barkeri suspension was centrifuged, washed, and resuspended three times in 0.9% NaCl (5 mL) for subsequent assays. For SCP studies, $ZnIn_2S_4$ was co-cultured with C. necator with/without Ension Y as an electron mediator.

### 2.2 Photocatalytic/biological performance and characterization.

Reactions were conducted in a 10-channel parallel photoreactor. After $N_2$ purge (10 min), $CO_2$ was introduced for 10 min at ambient pressure; temperature was maintained at 38 °C. Illumination used LEDs (400–750 nm, 100 mW $cm^{-2}$).

Analytics: $CH_4$ and $H_2$ were quantified by GC (FID); OD by microplate reader; SCP by Coomassie brilliant blue; extracellular electron transfer (EET) by INT-INF; cell viability by Beckman flow cytometry. To visualize the biotic–abiotic interface, inverted fluorescence microscopy and SEM were employed to evaluate cell activity and contact between $ZnIn_2S_4$ and cell surfaces. These methods, together with viability assays, informed the operational $ZnIn_2S_4$ dosage window that balances electron supply and biocompatibility.

## 3 Results and discussion

### 3.1 Interface formation and biocompatibility.

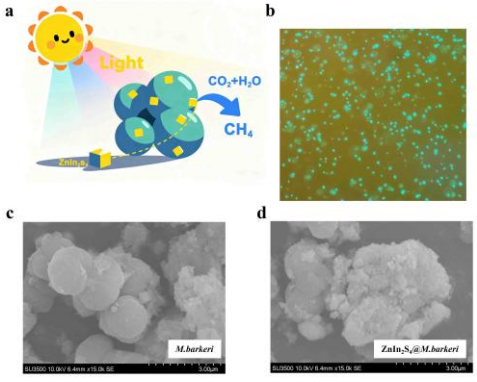


**Fig. 1. (a) Schematic of $ZnIn_2S_4$@M. barkeri; (b) fluorescence images at high $ZnIn_2S_4$ concentration; (c–d) SEM showing $ZnIn_2S_4$ adherence to cells.**

Inverted fluorescence microscopy revealed that even at 208.4 μg $mL^{-1}$ $ZnIn_2S_4$, M. barkeri remained active without significant viability loss, indicating good biocompatibility (Fig. 1b). SEM showed intimate contact between $ZnIn_2S_4$ and cell envelopes (Fig. 1c–d), consistent with a short electron-transfer distance at the interface. The conceptual configuration of the $ZnIn_2S_4$@M. barkeri PBS is summarized in Fig. 1a, highlighting potential $H_2$-mediated and mediator-assisted EET routes from the photocatalyst to intracellular methanogenesis.

### 3.2 Light-driven $CO_2$ methanogenesis with $ZnIn_2S_4$@M. barkeri

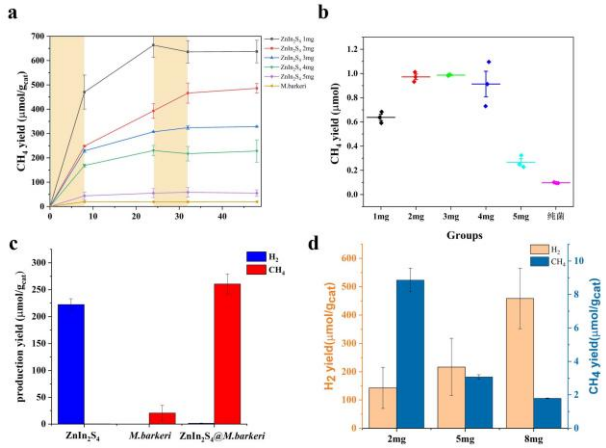


**Fig. 2. (a) Light–dark $CH_4$ trajectories at various $ZnIn_2S_4$ doses; (b) $CH_4$ vs. dose; (c) comparison to pure culture control; (d) $H_2$ evolution vs. dose.**

Under periodic light–dark operation (Fig. 2a), $H_2$ evolution increased monotonically with $ZnIn_2S_4$ dosage (Fig. 2d), while $CH_4$ formation exhibited an optimum at 2 mg $ZnIn_2S_4$ (Fig. 2b). The maximum $CH_4$ yield reached 0.97 μmol, which is ~9 fold the pure-culture control **(**0.10 μmol**;** Fig. 2c**)**. This non-monotonic $CH_4$ response is consistent with two counteracting effects: (i) higher dosage enhances electron availability (beneficial), whereas (ii) excess particles can induce shading or local reactive oxygen stress (detrimental). The 2 mg loading balances these factors, supporting efficient electron delivery from $ZnIn_2S_4$ to M. barkeri methanogenic pathways.

### 3.3 $CO_2$ to SCP with $ZnIn_2S_4$@C. necator and mediator assistance

In the absence of mediator, SCP productivity remained limited. Adding Ension Y improved electron shuttling from $ZnIn_2S_4$, leading to +8% OD (48 h) and +20% soluble protein (24 h) relative to the no-mediator case (Fig. 3c–d). Live/dead assays indicated a higher live-cell ratio with mediator across tested irradiances (Fig. 3b), consistent with sustained intracellular metabolism fueled by inorganic photogenerated electrons. The system layout for the SCP platform is summarized in Fig. 3a. Together, these results suggest that mediator-enabled EET complements $CO_2$ assimilation in C. necator, pointing to a modular strategy to boost biomass and protein formation in PBSs.

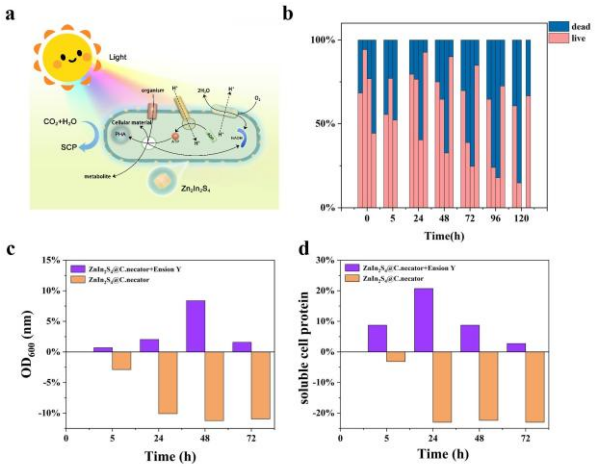


**Fig. 3. (a) Schematic of $ZnIn_2S_4$@C. necator; (b) live/dead ratios vs. irradiance; (c) OD with/without Ension Y; (d) soluble protein with/without Ension Y.**

## 4 Conclusions

A $ZnIn_2S_4$-based PBS enables stable, visible-light-driven $CO_2$ conversion to $CH_4$ with M. barkeri, and to SCP with C. necator—the latter further boosted by an electron mediator. By mitigating photocorrosion relative to CdS while preserving biocompatibility, $ZnIn_2S_4$ offers a generalizable route to robust, light-powered biohybrids for carbon-neutral fuels and proteins.

## Reference

[1] Ye, J.; Yu, J.; Zhang, Y.; et al. Light-Driven Carbon Dioxide Reduction to Methane by Methanosarcina barkeri–CdS Biohybrid. Applied Catalysis B: Environmental 2019, 257, 117916.
[2] Ye, J.; Wang, C.; Gao, C.; et al. Solar-Driven Methanogenesis with Ultrahigh Selectivity by Turning Down $H_2$ Production at Biotic–Abiotic Interface. Nature Communications 2022, 13, 6612.
[3] Ye, J.; Chen, Y.; Gao, C.; et al. Sustainable Conversion of Microplastics to Methane with Ultrahigh Selectivity by a Biotic–Abiotic Hybrid Photocatalytic System. Angewandte Chemie International Edition 2022, 61, e202213244.
[4] Pi, S. S.; Yang, W. J.; Feng, W.; et al. Solar-Driven Waste-to-Chemical Conversion by Wastewater-Derived Semiconductor Biohybrids. Nature Sustainability 2023, 6, 1673–1684.
[5] Hu, G.; Li, Z.; Ma, D.; et al. Light-Driven $CO_2$ Sequestration in Escherichia coli to Achieve Theoretical Yield of Chemicals. Nature Catalysis 2021, 4, 395–406.

# Removal of antibiotic resistance genes from post-treated swine wastewater by mFe/nCu system

○Yunhong Zhang [1,2*], Hao Wang [1,2] & Yuhuan Wu [1,2]
[1] Biogas Institute of Ministry of Agriculture and Rural Affairs, Chengdu 610041, China.
[2] Key Laboratory of Development and Application of Rural Renewable Energy, Ministry of Agriculture and Rural Affairs, Chengdu 610041, China
[*]E-mail: zhangyunhong@caas.cn

## Abstract

In this study, a distinct type of nanoscale copper, produced by iron-copper replacement (Fe-nCu), was used to reduce ARGs from post-treated swine wastewater. The effects of several key parameters (i. e., theoretical Cu mass loadings, Fe-nCu dosage, air flow rate, initial pH and temperature) were investigated in details. The contribution of nanoscale copper in Fe-nCu system towards ARGs removal was determined. Furthermore, the removal mechanism of ARGs by Fe-nCu was examined by SEM, TEM and living/dead cell staining. Results indicate that the Fe-nCu process can promptly remove the absolute abundances of ARGs (>2.4 logs) from post treated swine wastewater. The outstanding performance of this approach could be attributed to the use of nanoscale copper itself rather than the oxidation by Fenton-like reaction of Fe-nCu bimetallic system. Moreover, the Fe-nCu process exhibited an excellent activity in regards bacterial killing and destruction of ARGs structure and function which, ultimately, could serve as a plausible mechanism of ARGs removal. Reactivation experiments showed that ARGs removal by Fe-nCu was permanent and irreversible. Altogether, our findings suggest that Fe-nCu treatment can be a promising advanced method for ARGs removal from post treated swine wastewater.

**Keywords:** Swine wastewater; Antibiotic resistance genes; Nanoscale copper; Iron-copper bimetallic system.

## 1 Introduction

The misuse of antibiotics can induce genetic mutations and adaptive evolution in environmental microorganisms, leading to the emergence of antibiotic resistance genes (ARGs). These ARGs are now recognized as an emerging class of environmental contaminants, attracting increasing global concern [1]. Extensive use of antibiotics in medical and aquaculture settings has led to the proliferation of resistant microorganisms within gut microbiota and contaminated environments [2]. Antibiotic-resistant bacteria (ARB) carrying ARGs are subsequently released into the environment through various pathways, making medical wastewater and wastewater treatment plants (WWTPs) critical reservoirs and dissemination sources for ARGs [3]. Consequently, the development of efficient, cost-effective, and environmentally friendly technologies to eliminate ARB and ARGs from aquatic environments has become an urgent research priority.

In recent years, the application of nanotechnology in environmental remediation has attracted growing interest. Among various nanomaterials, Fe–Cu bimetallic nanoparticles (Fe–nCu) have emerged as a promising candidate, demonstrating remarkable performance in the removal of ARB and ARGs. These materials exhibit high removal efficiency, strong anti-interference capability, and unique mechanisms of action. Studies have shown that Fe–nCu nanoparticles can effectively inactivate microorganisms under both aerobic and anaerobic conditions, achieving 4.4 logs removal of Escherichia coli and MS2 phage within 15 minutes, reflecting potent cytotoxicity [4]. Notably, Fe–nCu has been reported to attain 3.75 and 4.36 logs removal efficiencies for intracellular and extracellular ARGs, respectively [5]. The underlying mechanism involves rapid induction of cellular oxidative stress, which disrupts intracellular redox homeostasis, leading to cell membrane damage and ultimately cell death [6]. Owing to these superior attributes, Fe–nCu represents a highly promising material for controlling environmental pollutants.

## 2 Materials and methods

### 2.1 Preparation of mFe/nCu and nanoscale copper particles

The Fe-nCu particles were prepared by the displacement reaction between Fe and $CuSO_4 \cdot 5H_2O$, in aqueous solution, as previously described. Mixing speed, temperature and $Cu^{2+}$ concentration ($CuSO_4 \cdot 5H_2O$) of the reaction solution were 250 rpm, 40 °C and 3 g/L, respectively. $CuSO_4 \cdot 5H_2O$ (analytical reagent) and zero valent iron (ZVI). The ZVI powder has a mean particle size of ~120 μm and iron content of ~98%.

The nCu-p particles were also prepared by the displacement reaction between Fe and $CuSO_4 \cdot 5H_2O$, in aqueous solution. For this, excess $CuSO_4 \cdot 5H_2O$ was used (1:1 Fe-Cu molar ratio). Upon completion of the displacement reaction, residual iron in the prepared nanoscale copper was magnetically separated.

### 2.2 *E. coli* suspension

We constructed *E. coli* (TOP 10) strains with plasmids encoding an ARG (pUC57), which resist ampicillin and tetracycline. The bacterial cells were cultured in a nutrient broth growth medium at 37 ℃ for 16 h to reach the logarithmic phase of bacterial growth. Then, the bacterial cell concentration was adjusted to a final cell concentration of 1 × 10 8 CFU/mL in 1 ×PBS solution, based on the principle that the bacteria must persist in appropriate osmotic pressure during Fe-nCu treatment.

## 3 Results and discussion

### 3.1 Contribution of nanoscale copper to the removal of ARGs

As shown in Fig.1, none of the ARGs could be eliminated within 30 min by mFe alone system. This indicated that no reactive substances were present in this procedure, such as •OH, which could remove ARGs effectively. Meanwhile, mFe/nCu, nCu-p, nCu-30 and nCu-100 could remove ARGs and had similar removal rates (between 2 and 3 logs).

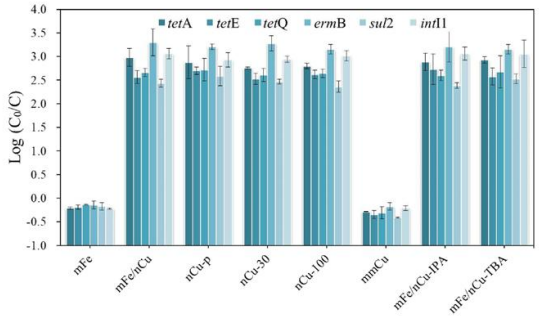


**Fig. 1. ARGs removal during different systems.**

### 3.2 Fe-nCu effect on bacterial cell membrane integrity

Generally, disruption of bacterial cell membrane integrity is the first indicator of bacterial inactivation. Before Fe-nCu treatment, all cells displayed strong green fluorescence (Fig. 2a). After Fe-nCu treatment, almost all cells were red, indicating that the *E. coli* cell membranes were severely damaged (Fig. 2b). (Green fluorescence represents *E. coli* with intact cell membranes, and red fluorescence represents *E. coli* with altered cell membrane permeability.)

Additionally, the FCM images provided data on cell membrane damage. Two areas were divided into two zones: area I indicated the number of cells with lost cell membrane integrity, and area II indicated cells with intact cell membranes. Before Fe-nCu treatment, almost all the cells had intact cell membranes (Fig. 2c). After Fe-nCu treatment for 30 min, the number of membrane-damaged cells increased sharply, from 4.72 % to 91.53 % (Fig. 2d).

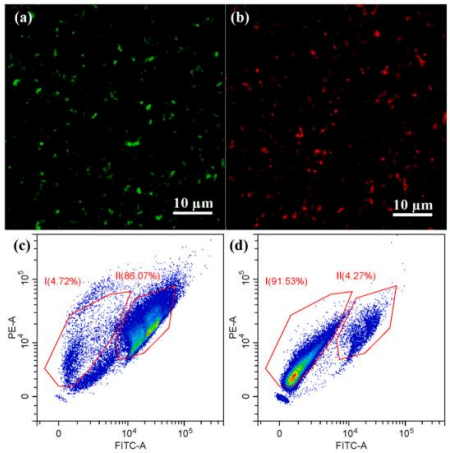


**Fig. 2. Confocal laser scanning microscopy (a-b) and FCM images of *E. coli* before and after Fe-nCu treatment (c-d)**

### 3.3 Bacterial morphology changes

We used SEM to observe *E. coli* cell morphology before and after Fe- nCu treatment. Untreated *E. coli* cells were rod-shaped and well-defined, with intact and smooth cell walls (Fig. 3a). After 30 min of Fe-nCu treatment, the cells showed noticeable folds and concave deformations (Fig. 3b). Using TEM, we further observed changes in the internal structure of *E. coli* cells before and after Fe-nCu treatment. The internal texture of untreated *E. coli* cells was clear and uniform; the cell membrane was intact, and cell morphology was regular (Fig. 3c). However, after 30 min of Fe-nCu treatment, the bacteria underwent plasma wall separation, the cell wall began to dissolve, and the cell membrane became blurred. (Fig. 3d)

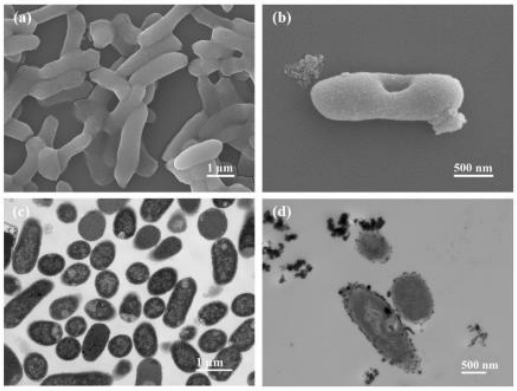


**Fig. 3. SEM and TEM images of untreated and Fe-nCu treated E. coli**

## 4 Conclusions

This study demonstrates that Fe-nCu can effectively remove intra cellular and extracellular ARGs. The removal of ARGs is facilitated by nCu.

## Reference

[1] Jingyang Luo, et al., Dissimilarity of different cephalosporins on volatile fatty acids production and antibiotic resistance genes fates during sludge fermentation and underlying mechanisms, Chinese Chemical Letters 34 (2023) 107661.

[2] M. Zhang, et al., Quantification of multi-antibiotic resistant opportunistic pathogenic bacteria in bioaerosols in and around a pharmaceutical wastewater treatment plant, Journal of Environmental Sciences 72 (2018) 53–63.

[3] A. Karkman, et al., Antibiotic-Resistance Genes in Waste Water, Trends in Microbiology 26 (2018) 220–228.

[4] H. Wang, et al., Mechanistic insights for efficient removal of intracellular and extracellular antibiotic resistance genes by iron-based nanocopper: Intracellular oxidative stress and internalization of nanocopper, Journal of Hazardous Materials 484 (2025) 136745.

[5] L. Zhang, et al., Oxidative damage of antibiotic resistant E. coli and gene in a novel sulfidated micron zero-valent activated persulfate system, Chemical Engineering Journal 381 (2020) 122787.

[6] F. Li, et al., Characteristics of microplastics in typical poultry farms and the association of environment microplastics colonized-microbiota, waterfowl gut microbiota, and antibiotic resistance genes, Journal of Hazardous Materials 490 (2025) 137808.

# The enhanced performance of partial denitrification/anammox-hydroxyapatite (PDA-HAP) system based on the high up-flow velocity

Shenghao Ji[1], Yu-You Li[1,2*]

[1]Department of Civil and Environmental Engineering, Graduate School of Engineering, Tohoku University, 6-6-06 Aza, Aramaki, Aoba-ku, Sendai, Miyagi 980-8579, Japan

[2]Department of Frontier Science for Advanced Environment, Graduate school of Environmental Studies, Tohoku University, 6-6-20 Aoba, Aramaki-Aza, Aoba-ku, Sendai, Miyagi 980-8579, Japan

* Corresponding author: Yu-You Li, e-mail: gyokuyu.ri.a5@tohoku.ac.jp

## Abstract

Partial denitrification/anammox (PDA) offers an efficient method for achieving deep denitrification in effluents after the anaerobic ammonium oxidation (anammox) process has treated high-ammonium wastewater. However, sludge flotation remains a significant operational challenge in PDA reactors, limiting the reactor performance. Increasing the up-flow velocity can promote nitrogen gas release and reduce flotation but does not resolve poor sludge settleability，limiting its effectiveness. Hydroxyapatite (HAP) provides an effective solution to address the fundamental issue of poor settling performance. The reactor can maintain high sludge settleability even at elevated up-flow velocities by forming PDA-HAP granules, thereby enhancing mass transfer and reactor capacity. In this study, a high nitrogen loading rate (NLR) of 4.11 g N/L/d was successfully achieved at an up-flow velocity of 3.78 m/h. The presence of HAP ensured that the upper sludge, which typically exhibited weaker settling performance, maintained excellent settleability (>40 m/h), thereby enabling the use of higher up-flow velocities. Under enhanced mass transfer conditions, the PDA-HAP reactor achieved a total nitrogen removal efficiency (TNRE) of 89.2% and an anammox contribution efficiency (ACE) of 80.1% during high-load operation. This study presents a viable strategy for improving PDA performance, supporting the broader implementation of anammox-based technologies for treating high-ammonium wastewater.

**Keywords:** PD/Anammox; Up-flow velocity; Hydroxyapatite; High load; Settleability

## 1 Introduction

In the field of high-ammonium wastewater treatment, the two-stage partial nitrification/anammox (PNA) process has gained broad recognition because of the stability of its microbial populations [1]. However, based on the stoichiometry of the anammox reaction, the two-stage PNA process can remove only 89% of the total nitrogen (TN), leaving 11% of the nitrogen in the form of nitrate [2]. This does not meet the standards for nitrogen discharge. The partial denitrification/anammox (PDA) strategy offers a promising pathway for enhanced nitrogen removal from the effluent of a two-stage PNA process [3]. However, sludge flotation remains a major operational challenge in PDA reactors, significantly restricting performance optimization [4]. The flotation tendency of PDA sludge is primarily attributed to the entrapment of nitrogen gas within the sludge matrix, which prevents its effective release. This issue becomes more pronounced under high-load conditions owing to intensified gas production. Facilitating gas release is crucial for mitigating sludge flotation and enhancing the overall performance of PDA. In expanded granular sludge bed (EGSB) reactors, increasing the up-flow velocity by adjusting the recirculation ratio is a simple and effective strategy to promote nitrogen gas release while simultaneously improving mass transfer efficiency [2]. However, this approach does not fundamentally resolve the issue of sludge settleability, and the risk of performance deterioration due to sludge flotation remains. Excessive recirculation rates can also lead to sludge washout, adversely affecting PDA performance. Accordingly, improving the settling properties of PDA sludge is essential for maintaining stability under high up-flow velocities and improving the overall treatment capacity of the PDA process. Hydroxyapatite (HAP) is an effective agent for enhancing sludge settleability. When coupled with anammox granular sludge, HAP can increase sludge settling velocity to over 280 m/h. The integration of HAP can significantly enhance PDA sludge settleability, enabling it to withstand higher up-flow velocities, improve mass transfer efficiency, and ultimately enhance process performance. However, research on their application in PDA systems remains limited. The objective of this study was to investigate the effect of high up-flow velocity on the enhancement of PDA-HAP reactor performance.

## 2 Materials and methods

An EGSB reactor with an effective working volume of 5.0 L was employed. The operation was divided into six phases, with corresponding up-flow velocities: phase 1 (0.87 m/h); phase 2 (1.65 m/h); phase 3 (1.97 m/h); phase 4 (3.32 m/h); phase 5 (3.69 m/h); phase 6 (3.78 m/h). Sodium acetate served as the external carbon source throughout the operation, with the carbon-to-nitrogen (C/N) ratio maintained at 2.7 to ensure consistent process conditions. Additionally, the $NO_3^-$-N/$NH_4^+$-N ratio in the influent was controlled at 1.4. The seed sludge employed in this study was sourced from a well-established PDA reactor that had been consistently treating food waste dewatering effluents under stable operational conditions. The synthetic wastewater was formulated with $NH_4^+$-N and $NO_3^-$-N as the primary nitrogenous substrates. Its composition included the following constituents (mg/L):

$NaNO_3$ 910, $NH_4Cl$ 420, KCl 570, $NaHCO_3$ 1000, $CaCl_2{\cdot}2H2O$ 142, $KH_2PO_4$ 79.1, $MgSO_4{\cdot}7H_2O$ 100, $FeCl_2{\cdot}4H_2O$ (0.125 ml/L), Trace elements (0.125 ml/L).

The concentrations of $NO_3^-$-N, $NH_4^+$-N, and $NO_2^-$-N were measured using a capillary electrophoresis (CE) system. The chemical oxygen demand (COD) was determined according to standard method. A pH meter was used to measure the pH. The calcium, magnesium and phosphorus were quantified using inductively coupled plasma optical emission spectroscopy (ICP-OES). Alkalinity (ALK, mg CaCO3/L) was measured by potentiometric titration without color change, and the pH at the end of the titration was 4.4. The setting velocity of PDA sludge was measured in the middle 1 m through a 2 m water column. The microbial community of the collected samples was tested by the Bioengineering Lab, Japan, using primers 341 F and 805 R, and further analyzed using the QIIME2 framework.

## 3 Results and discussion

This part is Results and discussion.

The PDA operation process can be divided into six phases based on different NLR, which increased from 0.84 g N/L/d to 4.11 g N/L/d, and achieve a stable operation in high-load condition (Fig. 1). During Phase 1, a reflux ratio of 8.3 was maintained, resulting in an up-flow velocity of 0.87 m/h within the reactor. However, the PDA performance was poor, with a TNRE of only 69.4% and ACE of only 64.4%, which may have been caused by uneven mass transfer at low up-flow velocities. It has been reported that the high up-flow velocity can promote sludge fluidization and mass transfer. Therefore, in phase 2, the reflux ratio was increased to 16.5, and the up-flow velocity was raised to 1.65 m/h. After changing the conditions, the PDA performance improved significantly, with the TNRE increasing to 86.2% and the $NH_4^+$-N and $NO_3^-$-N removal efficiencies reaching 74.0% and 95.2%, respectively. Meanwhile, the ACE increased to 73.4%. This indicates that increasing the up-flow velocity can effectively improve PDA performance. In Phase 3, the NLR was elevated to 1.49 g N/L/d by adjusting the influent flow rate. Concurrently, the reflux ratio was set at 10.9, leading to an up-flow velocity increase to 1.97 m/h. The reactor performance was further improved, achieving a TNRE of 87.6% and an ACE of 78.9%. In phase 4, the NLR was further increased to 2.44 g N/L/d, with the reflux ratio maintained and the up-flow velocity increased to 3.32 m/h. The TNRE improved to 91.7% and the ACE increased to 84.0%. Although increasing up-flow velocity can promote gas release and reduce sludge flotation, high velocities can lead to sludge bulking and increased energy consumption. Consequently, during Phase 5, the NLR was enhanced to 3.27 g N/L/d by further elevating the influent flow rate, while the up-flow velocity was kept unchanged basically to ensure consistent hydraulic conditions. A high up-flow velocity could still ensure effective mass transfer and gas release, achieving a TNRE of 93.4% and an ACE of 81.0%. In phase 6, the NLR was further increased, while the up-flow velocity was kept constant, and the reflux ratio was reduced to 7. The PDA performance remained stable with a TNRE of 89.2% and an ACE of 80.1%.

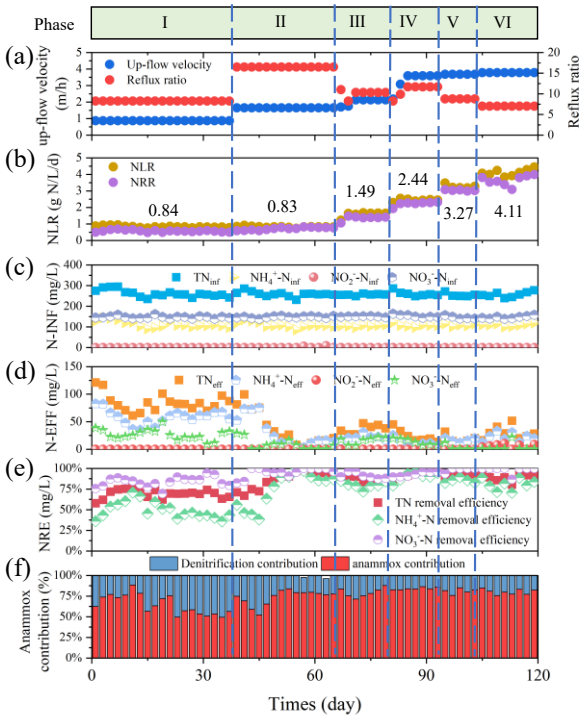


**Fig. 1. The operation performance of the PDA-HAP reactor at different up-flow velocity**

## 4 Conclusions

A high-load PDA-HAP reactor of 4.11 g N/L/d was successfully achieved in this study. A high up-flow velocity is key to enhancing the PDA performance, and the presence of HAP provides the foundation for the PDA reactor to withstand high up-flow velocities. Ultimately, the reactor achieved a TNRE of 89.2% and an ACE of 80.1% under high-load conditions.

## Reference

[1] Y. Song, Z. Ma, Y. Qin, W. Zhao, W.-K. Qi, Y.-Y. Li, A novel system of two-stage partial nitritation/hydroxyapatite (HAP)-anammox treating effluent of anaerobic membrane reactor: Performance, elemental flow and nutrient recovery potentials, Resources, Conservation and Recycling 184 (2022).

[2] R. Du, S. Cao, B. Li, H. Zhang, S. Wang, Y. Peng, Synergy of partial-denitrification and anammox in continuously fed upflow sludge blanket reactor for simultaneous nitrate and ammonia removal at room temperature, Bioresour Technol 274 (2019) 386-394.

[3] H.E. Al-Hazmi, M. Maktabifard, D. Grubba, J. Majtacz, G.K. Hassan, X. Lu, G. Piechota, G. Mannina, C.B. Bott, J. Makinia, An advanced synergy of partial denitrification-anammox for optimizing nitrogen removal from wastewater: A review, Bioresour Technol 381 (2023) 129168.

[4] L. Lin, Z. Luo, Y. Zhang, Y. Ren, Y.-Y. Li, Partial denitrification-anammox granular sludge domesticated from high-strength anammox granules and the high-efficiency performance in treating low-nitrogen wastewater, Chem. Eng. J. 477 (2023).

# Municipal Wastewater Treatment by Novel Two-step System Based on Partial-denitrification/Anammox Process

○ Weizhe XIA[1*], Yizhu SUN[1], Zibin LUO[1] and Yu-You LI[1]

[1] Dept. of Civil and Environmental Engineering, Graduate School of Engineering, Tohoku University, 6-6-06 Aoba, Sendai, 980-8579, Japan.

[*]E-mail: xia.weizhe.r5@dc.tohoku.ac.jp

## Abstract

A novel partial-denitrification/anammox (PD/A)-based process was investigated for mainstream treatment of low-strength municipal wastewater. The system consistently achieved over 90% total inorganic nitrogen removal and maintained effluent COD levels below 25 mg/L across varying influent $NH_4^+$-N/$NO_3^-$-N ratios. The PD/A reactor exhibited stable organic matter removal and effective nitrogen transformation, with anammox activity contributing between 48% and 58%. These findings demonstrate that the PD/A system enables efficient and energy-saving nitrogen and COD removal in mainstream municipal wastewater treatment, offering a promising approach for sustainable urban sewage management.

**Keywords:** mainstream wastewater; low nitrogen wastewater; partial-denitrification/anammox.

## 1 Introduction

Since its discovery in the 1990s, the anammox reaction has greatly advanced the development of wastewater treatment technologies. Although the process has been widely applied to high-strength wastewater, its application to low-strength municipal wastewater remains limited. This limitation arises mainly from the high COD levels in municipal wastewater, which favor denitrifying bacteria over anammox bacteria, and the low nitrogen concentrations, which provide insufficient substrate for anammox activity. To overcome these challenges, this study introduces a wastewater treatment system based on the partial denitrification/anammox (PD/A) process.

## 2 Materials and methods

### 2.1 Composition of the system

This study investigates the feasibility of the proposed system for urban sewage treatment and examines the influence of varying ammonia-nitrogen to nitrate-nitrogen ratios on its performance. The system comprises a primary sedimentation tank, a nitrification unit, an intermediate tank, and a PD/A reactor (Fig. 1). Effluent from the primary sedimentation tank is divided into two streams: one directed to the nitrification unit for nitrate ($NO_3^-$–N) generation, and the other fed directly to the PD/A reactor to provide ammonia nitrogen and organic carbon, enabling simultaneous removal of COD and nitrogen from the mainstream wastewater.

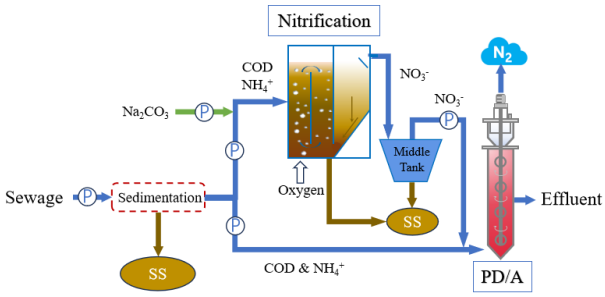


**Fig. 1 schematic diagram of PD/A based system**

The effective volumes of the primary sedimentation tank, intermediate tank, nitrification unit, and PD/A reactor were 27 L, 4 L, 5 L, and 5 L, respectively. The nitrification unit operated as an airlift reactor, while the PD/A reactor was configured as an upflow anaerobic sludge blanket (UASB) reactor. To maintain stable pH conditions, a sodium carbonate ($Na_2CO_3$) solution at a concentration of 75 mg/L was continuously supplied to the nitrification unit.

### 2.2 Analytical methods

Influent and effluent samples were filtered by 0.45 μm filter. Capillary electrophoresis (Agilent 7100) was used to measure nitrogen concentrations. COD was analyzed according to APHA standard method.

## 3 Results and discussion

### 3.1 Operation parameter

The sewage is from the wastewater plant in Sendai. The characteristics are shown in Table 1.

**Table 1 Characteristics of Sewage**

| Phase | pH | COD (mg/L) | $NH_4^+$-N |
|---|---|---|---|
| 1 | 7.06 ± 0.14 | 320 ± 116 | 22.1 ± 3.7 |
| 2 | 6.91 ± 0.16 | 244 ± 91 | 21.3 ± 3.5 |

The ratio of $NH_4^+$ - N and $NO_3^-$ - N of the PD/A influent was controlled by the flow rate of the primary sedimentation tank effluent into the nitrification unit and PD/A reactor. In phase 1 (day 25 – 69), the ratio of flow rate was 1: 3; in phase 2 (day 98-134), the ratio came to 1: 2.

### 3.2 Sedimentation tank

Table 2 summarizes the effluent quality from the primary sedimentation tank.

**Table 2 Characteristics of sedimentation effluent**

| Phase | 1 | 2 |
|---|---|---|
| pH-eff | 6.99 ± 0.12 | 6.91 ± 0.07 |
| COD-eff (mg/L) | 120 ± 37 | 96 ± 25 |
| $NH_4^+$-N-eff | 20.7 ± 3.0 | 21.9 ± 4.6 |

The water quality of the primary sedimentation tank showed minor variation between phases 1 and 2, with COD removal efficiency (CODRE) decreasing from 60% to 55%, while ammonia nitrogen remained relatively stable, ensuring sufficient substrate for subsequent biological reactions.

### 3.3 Performance of nitrification unit

The nitrification unit maintained stable COD removal efficiency (CODRE) across both operational phases, with effluent COD concentrations consistently around 50 mg/L, indicating effective elimination of residual organic matter from the wastewater. In phase 1, the reactor achieved an ammonia removal efficiency (ARE) of 99%, and the effluent nitrogen was predominantly in the form of nitrate (17.5 mg-N/L), with a minor presence of nitrite (1.2 mg-N/L). During phase 2, effluent ammonia and nitrite concentrations were 0.9 mg-N/L and 1.5 mg-N/L, respectively, while nitrate increased slightly to approximately 18 mg-N/L. The observed decrease in ARE during phase 2 was attributed to variations in influent water quality, whereas changes in flow rate had negligible influence on reactor performance.

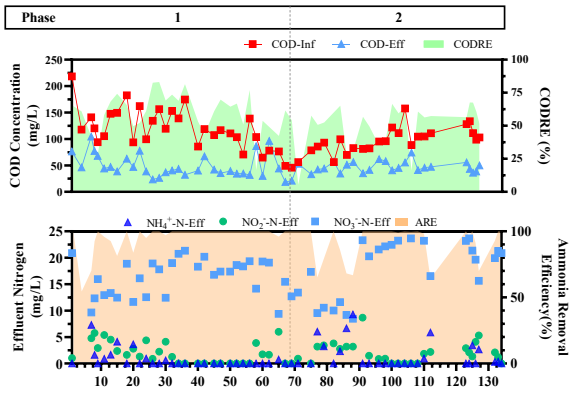


Fig. 2. Performance of nitrification unit

### 3.4 Performance of PD/A reactor

In phase 2 of the PD/A reactor, the influent COD concentration increased from 40 mg/L to 54 mg/L due to changes in the influent ratio, while the effluent COD remained stable at approximately 24 mg/L. During phase 1, the reactor achieved a high ammonia removal efficiency (ARE) of about 95%, with effluent $NH_4^+$–N concentrations around 0.3 mg/L. However, following the change in influent ratio, the ARE decreased to 73% in phase 2, accompanied by a rise in effluent ammonia to roughly 1.9 mg/L. Only ammonia nitrogen was detected in the effluent throughout both phases, suggesting that partial and complete denitrification occurred effectively within the system. The elevated effluent ammonia in phase 2 was mainly attributed to the increased influent ammonia concentration and COD/N ratio, along with a reduced $NH_4^+$–N/$NO_3^-$–N ratio, which led to incomplete PD/A reactions. The contribution of the anammox process accounted for 48% in phase 1 and increased to 58% in phase 2 due to the lower nitrate concentration.

The reactor achieved a total inorganic nitrogen removal efficiency (TINRE) of 98% in phase 1, corresponding to an effluent concentration of 0.3 mg-N/L. In phase 2, the TINRE slightly decreased to 92%, with an effluent concentration of 1.9 mg-N/L. These results demonstrate that the PD/A reactor maintains excellent performance in removing both TIN and COD from low-strength municipal wastewater. Overall, the PD/A-based system presents a promising and energy-efficient approach for nitrogen removal in mainstream urban wastewater treatment.

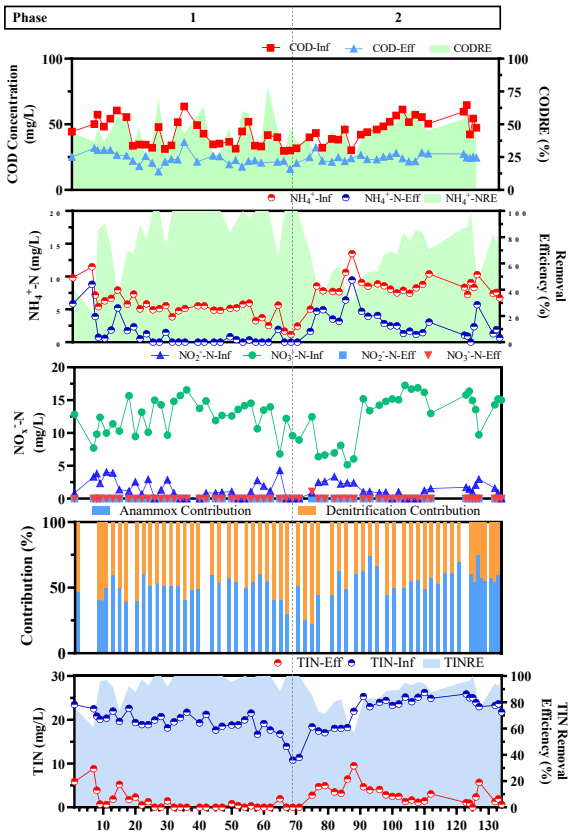


Fig. 3. Performance of PD/A reactor

## 4 Conclusions

This study demonstrated that a PD/A-based system could effectively treat municipal wastewater with low ammonia concentrations, consistently achieving TIN removal efficiency (TINRE) above 90%, effluent TIN below 2 mg/L, and COD below 25 mg/L across all phases. Variations in the flow rate ratio were found to significantly influence TIN removal, with effluent TIN increasing as the proportion of nitrate nitrogen in the influent decreased. Future work will focus on further examining the effects of flow rate ratio on overall system performance.

## Reference

[1] APHA., Standard Methods for the Examination of Water and Wastewater. APHA-AWWA-WEF, Washington, DC, USA, 2005.

[2] Lin. et al., Partial denitrification-anammox granular sludge domesticated from high-strength anammox granules and the high-efficiency performance in treating low-nitrogen wastewater, Chemical Engineering Journal, 2023.

# Effects of Hydraulic Retention Time and Organic Loading Rate on Mesophilic Methanogenic Treatment of Brewery spent grain

○ Weiquan LI[1*], Kengo KUBOTA[1], Yu-you LI[1,2*]

[1] Department of Frontier Science for Advanced Environment, Graduate School of Environmental Sciences, Tohoku University, 6-6-06 Aoba, Aramaki-Aza, Sendai, 980-8579, Miyagi, Japan.

[2] Department of Civil and Environmental Engineering, Graduate School of Engineering, Tohoku University, 6-6-06 Aoba, Aramaki-Aza, Sendai, 980-8579, Miyagi, Japan

[*]E-mail: li.weiquan.r4@dc.tohoku.ac.jp

## Abstract

The growing beer industry generates vast amounts of brewery spent grain (BSG), a promising anaerobic digestion (AD) substrate hindered by its low C/N ratio and lignocellulosic structure. Pretreatments are often costly, and system stability in continuous operation remains poorly understood. This study investigated the effects of hydraulic retention time (HRT) and organic loading rate (OLR), modulated via total solids (TS) content, on the continuous mesophilic (35°C) anaerobic digestion of brewery spent grain (BSG) in a CSTR. Results demonstrated that at 10% TS, reducing HRT from 100 to 30 days increased the average methane production rate from 0.325 to 0.853 L/L/d. However, this shorter HRT also led to a significant decrease in the degradation efficiencies of TS, VS, and COD. A critical failure occurred at a higher load of 15% TS and 30-day HRT, characterized by a rapid accumulation of propionic acid to 2600 mg/L and eventual system collapse. The study concludes that while the process remains stable and efficient at 10% TS and a 30-day HRT, excessive OLR induced by high TS content severely inhibits digestion. Therefore, careful control of TS and HRT is paramount for the stable and efficient operation of anaerobic digesters treating BSG.

**Keywords:** Anaerobic digestion; Hydraulic Retention; Total solid; Mesophilic.

## 1 Introduction

Energy issues remain a persistent focus of attention in Japan. Among various biomass resources, brewers' spent grain (BSG), a primary brewing by-product, possesses significant potential for resource recovery. In 2023, global beer production reached approximately 188.8 billion liters, corresponding to a BSG output of 37.6 million tons. This substantial volume presents both a major challenge and opportunity for the efficient treatment and resource utilization of BSG[1,2].

Traditionally, BSG has been primarily used as animal feed. However, amidst increasingly stringent environmental regulations and the growing need for sustainable development in Japan, the conversion of BSG into energy has garnered significant interest. Among the available technologies, anaerobic digestion, which simultaneously achieves waste treatment and energy recovery, has emerged as a critical pathway for the resource utilization of BSG[3,4].

Nevertheless, several key challenges remain in the anaerobic digestion process of BSG. This study aims to investigate the effects of hydraulic retention time (HRT) and organic loading rate (via Total Solids content) on reactor performance during the mesophilic (35°C) anaerobic digestion of BSG using a continuous stirred-tank reactor (CSTR). The research focuses on varying the operational load by adjusting different HRTs and TS concentrations, thereby assessing the impact on key performance indicators, including biogas production, COD-based mass balance, and volatile fatty acids analysis.

## 2 Materials and methods

### 2.1 Experimental Setup and Materials

Figure 1 shows the schematic diagram of mesophilic AD system used for the continuous experiment. The temperature was maintained at mesophilic conditions (35±1°C) via a heater and water jacket, and mixing within the tank was achieved using a motor-driven impeller with mechanical stirring[5].

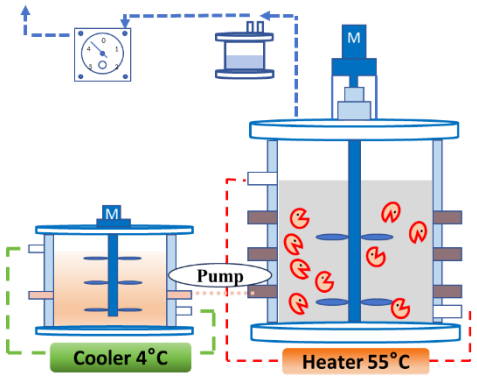


Fig.1. Schematic of Mesophilic AD System

The feedstock used in this experiment was BSG, a solid waste supplied from a factory in Japan. The initial total solids (TS) content of the BSG was 37%, which was diluted with water to concentrations of 10% and 15% TS for use. Trace elements were added based on varying load conditions, with $FeCl_3 \cdot 6H_2O$: 60mg/kg CODin, $NiCl_2 \cdot 6H_2O$: 7.5 mg/kg CODin, and $CoCl_2 \cdot 6H_2O$: 7.5 mg/kg CODin used as the standard. The inoculum sludge was obtained from a previous anaerobic digestion reactor treating BSG in our laboratory.

## 3 Results and discussion

### 3.1 Biogas Production under Different HRTs

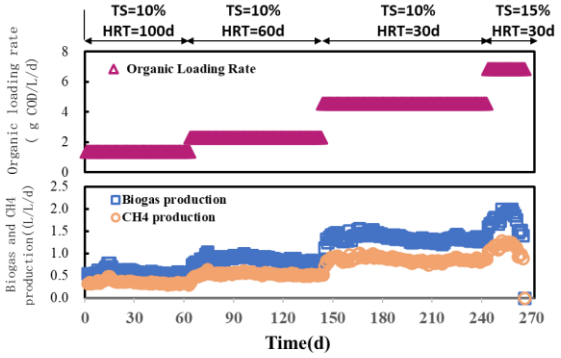


Fig.2. Biogas and $CH_4$ production

As shown in the Figure 2, the average biogas production rates under each operational condition were 0.538 ± 0.03 L/L/d in Run 1, 0.823 ± 0.01 L/L/d in Run 2, 1.322 ± 0.04 L/L/d in Run 3, and 1.766 ± 0.16 L/L/d in Run 4, showing a trend of increase proportional to the organic loading rate. The average methane production rates were 0.325 ± 0.01 L/L/d in Run 1, 0.515 ± 0.01 L/L/d in Run 2, 0.853 ± 0.03 L/L/d in Run 3, and 1.132 ± 0.11 L/L/d in Run 4, also increasing with the organic load.

However, in Run 4, the biogas and methane production rates peaked within 10 days but then rapidly declined to zero, leading to a complete reactor failure.

### 3.2 COD Mass Balance Analysis

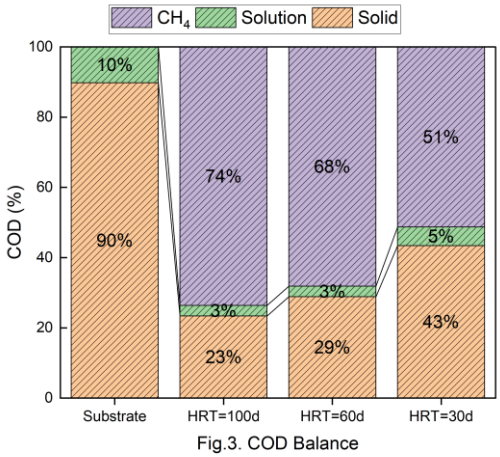


Fig.3. COD Balance

This analysis involved establishing a Chemical Oxygen Demand (COD) mass balance to elucidate material degradation dynamics during methanogenesis. The influent substrate COD was normalized to 100%, with constituent mass distributions calculated across three principal phases: particulate solids, soluble metabolites, and methane gas. Results delineated in Figure 3 indicate that the feedstock composition was 90% solid and 10% soluble. Process evolution under diminishing HRT revealed a systematic decline in methane conversion (from 74% to 51%), accompanied by accumulating soluble intermediates (3% to 5%) and residual solids (23% to 43%). These trends collectively indicate compromised degradation efficacy at reduced retention times.

### 3.3 Volatile Fatty Acids (VFA) Analysis

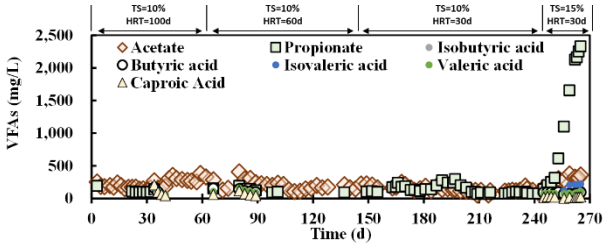


Fig.4. Volatile Fatty Acid (VFA) Concentration

The concentrations of volatile fatty acids (VFA) in Runs 1, 2, and 3 were all maintained at low levels throughout these three phases, and no significant accumulation was observed. In contrast, Run 4 exhibited a distinct behaviour, where the concentration of propionic acid reached a maximum of 2600 mg/L. Due to the high organic loading rate, it accumulated daily. This value exceeds the typical inhibition threshold for anaerobic digestion processes, suggesting that this accumulation was likely the primary cause of the overall deterioration and failure of the reactor.

## 4 Conclusions

In this study, under the condition of TS=10% and HRT=30 days, the anaerobic digestion process was stably operable. The volatile fatty acid (VFA) concentration within the system remained low, and both biogas production (1.32 L/L/d) and methane production (0.85 L/L/d) stabilized at high levels, demonstrating high process stability and energy recovery efficiency.

In contrast, under the condition of increased TS=15% with HRT maintained at 30 days, rapid accumulation of propionic acid occurred within the process, reaching a concentration of 2600 mg/L. This value significantly exceeds the generally accepted threshold of 1000 mg/L for anaerobic digestion processes. Gas production rapidly declined, ultimately leading to the collapse of the anaerobic digestion system.

These results strongly suggest that for the stable operation of the anaerobic digestion process, it is crucial to appropriately control the TS content and hydraulic retention time, and to design and operate the process under a reasonable organic loading rate.

## Reference

[1] Mussatto, S. I., Dragone, G. & Roberto, I. C. Brewers' spent grain: Generation, characteristics and potential applications. J. Cereal Sci. 43, 1–14 (2006).

[2] P.M., T. Preparation of commercial products from brewer's waste grain and trub. Tech. Q. Master Brew. Assoc. Am. 16, 130-134(3) (1979).

[3] Bisaria, R., Madan, M. & Vasudevan, P. UTILISATION OF AGRO-RESIDUES AS ANIMAL FEED T H R O U G H BIOCONVERSION. 59, 5–8 (1997).

[4] Statisa. Global beer production 1998-2023. (2024)

[5] Ren, Y. et al. System stability associated with different lipid contents during mesophilic anaerobic digestion of lipid-rich food waste. J. Clean. Prod. 443, 141171 (2024).

# Adaptive Modeling of Extreme Precipitation in Japan using Peaks Over Threshold Approach

○ Muhammad Aslam Mohd SAFARI [1, 2*] & Tosiyuki NAKAEGAWA[2]
[1]Department of Mathematics and Statistics, Faculty of Science, Universiti Putra Malaysia, 43400 UPM Serdang, Selangor, Malaysia
[2]Department of Applied Meteorology, Meteorological Research Institute, Japan Meteorological Agency, Tsukuba, Japan
*E-mail: aslam.safari@upm.edu.my

## Abstract

Extreme precipitation poses a persistent threat in Japan, where typhoons, monsoons, and complex topography cause recurrent floods and landslides. This study applies the peaks-over-threshold framework with the generalized Pareto distribution (GPD) to model extreme precipitation using daily rainfall data from 51 synoptic stations across Japan covering 1901–2020. For stations exhibiting temporal dependence, a 5-day blocking strategy was applied to isolate independent exceedances. Thresholds were determined using mean residual life plots, while parameters were estimated by maximum likelihood estimation and L-moments. The GPD model's performance was verified using the Kolmogorov–Smirnov and Anderson–Darling tests, supported by relative root mean square error. Results show that the L-moment method provided more stable and accurate estimates across most locations. Return levels for 5–, 10–, 20–, 50–, 100–, and 200-year periods revealed strong spatial contrasts: southern regions such as Kyushu and Okinawa–Amami exhibited much higher design rainfall values than northern regions like Hokkaido, reflecting the strong influence of typhoons and monsoonal rains. These findings provide critical insights into extreme precipitation risks, offering valuable guidance for region-specific flood risk management and disaster mitigation strategies in Japan.

**Keywords:** Extreme value modeling; extreme precipitation; generalized Pareto; L-moment; return level

## 1 Introduction

Japan's geographical setting and exposure to typhoons make it highly susceptible to extreme rainfall and flood disasters. Events such as the July 2018 and 2020 floods caused severe landslides and infrastructure damage, with losses exceeding ¥500 billion [1]. Climate change further amplifies such extremes. The IPCC AR6 reported a global temperature rise of 1.1°C since 1850–1900, projected to reach 1.5°C within two decades [2]. Studies by Hatsuzuka and Sato [3], Watanabe et al. [4], and Kawase et al. [5] revealed an increasing trend in 100-year rainfall intensity in western Japan under future warming scenarios.

Extreme value theory (EVT) provides a framework for estimating rare events beyond historical limits [6]. The block maxima (BM) approach, based on the generalized extreme value (GEV) distribution, is widely used but often discards submaximal information, reducing statistical efficiency. Conversely, the peaks-over-threshold (POT) method employs all exceedances above a threshold and fits them using the generalized Pareto distribution (GPD), which effectively captures the tail behavior of extremes [7]. The GPD's flexibility through its shape parameter allows characterization of both light- and heavy-tailed processes.

## 2 Materials and methods

Daily precipitation data from 51 JMA synoptic stations spanning 1901–2020 were analyzed. These stations cover diverse climate zones, from northern Hokkaido to the typhoon-prone Okinawa–Amami islands.

In the POT framework, all rainfall values $X$ that exceed a threshold $\tau$ are modeled using the GPD. The cumulative distribution function (CDF) of the GPD is expressed as

$$F(x;\sigma,\xi)=\begin{cases}1-\left(1+\dfrac{\xi(x-\tau)}{\sigma}\right)^{-\frac{1}{\xi}} & \text{for } \xi\neq 0,\\ 1-\exp\left(-\dfrac{(x-\tau)}{\sigma}\right) & \text{for } \xi=0,\end{cases} \quad (1)$$

The threshold $\tau$ was determined using mean residual life (MRL) plots [8], with values typically between 50–100 mm to ensure tail stability.

The POT method assumes independent exceedances. The Ljung–Box test [9] identified significant serial correlation ($p < 0.05$) at several stations, indicating clustering due to multi-day rainfall. Based on a preliminary analysis of consecutive exceedances, a 5-day blocking window was adopted, retaining only the maximum value within each block. Retesting after blocking confirmed independence ($p > 0.05$).

The parameters $\sigma$ and $\xi$ were estimated using both maximum likelihood estimation (MLE) and L-moments (LMOM) methods. The L-moments (LMOM) approach [10,11] is particularly robust for skewed rainfall and provides stable estimates even in the presence of outliers.

Model adequacy was assessed using the Kolmogorov–Smirnov (KS) and Anderson–Darling (AD) tests, complemented by the Relative Root Mean Square Error (RRMSE). Models with $p$-values greater than 0.05 were accepted as adequately describing the extreme tail behavior.

Return levels were estimated to quantify rainfall magnitudes associated with specific return periods (e.g., -year event). These values were derived from the fitted GPD parameters and represent the rainfall intensity expected to be exceeded once every given period. The estimated return levels provide a direct basis for assessing design rainfall and flood risk in different climatic regions of Japan.

## 3 Results and discussion

Thresholds determined using MRL plots ranged from 50 mm to 100 mm, reflecting Japan's diverse climatic conditions. Lower thresholds were sufficient for temperate regions, while higher ones were needed in typhoon-affected southern areas. Independence testing with the Ljung–Box test revealed serial correlation at Wakayama, Kochi, and Kumamoto, for which the previously described 5-day blocking was applied to ensure independence.

Both MLE and LMOM produced good parameter estimates, with LMOM showing better stability under skewed distributions. Goodness-of-fit tests (KS, AD) confirmed that the GPD accurately captured the tail behavior of precipitation exceedances across all 51 stations. The shape parameter $(\xi)$ varied considerably among stations, positive values reflected heavy-tailed behavior and a greater likelihood of very large precipitation events, while negative values suggested a bounded tail and upper limits on rainfall intensity. Similarly, the scale parameter $(\sigma)$ varied across regions, with higher values indicating a wider spread of exceedance magnitudes and lower values reflecting more uniform rainfall extremes.

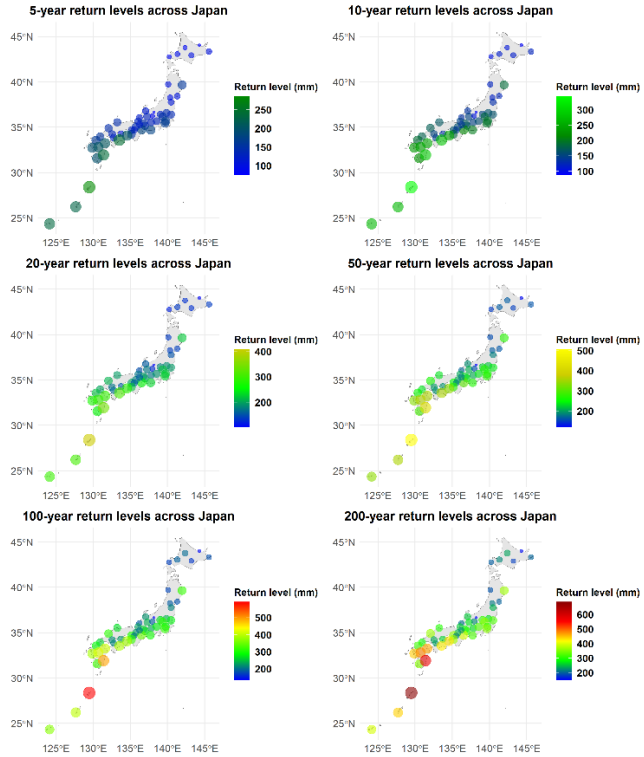


**Fig. 1. Return levels of extreme precipitation in Japan**

Estimated return levels for 5–, 10–, 20–, 50–, 100–, and 200-year periods exhibited a clear north–south gradient (Fig. 1). Southern Japan recorded design rainfall exceeding 600 mm day$^{-1}$ (e.g., Naze ≈ 686 mm for 200 years), while northern areas such as Abashiri showed below 200 mm day$^{-1}$ (≈ 155 mm for 200 years). This pattern aligns with Japan's climatic gradient, typhoon and monsoonal influences dominate in the south, while low-pressure and frontal systems govern the north. Compared with the JMA BM–GEV results (1901–2006), the present POT–GPD analysis (1901–2020) produced higher and more spatially detailed estimates, capturing recent extremes and improving representation of the upper tail behavior.

## 4 Conclusion

This study demonstrates the effectiveness of the POT approach with the GPD in modeling extreme precipitation across Japan, using data from 51 observation stations spanning 120 years. Temporal dependence at a few stations was addressed through selective 5-day blocking, ensuring robust and reliable modeling. Threshold selection via MRL plots and parameter estimation using MLE and L-moments further strengthened the framework. The spatial analysis of return levels revealed pronounced regional variability, with southern regions such as Kyushu and Okinawa–Amami experiencing much higher extremes than northern areas like Hokkaido, highlighting the influence of typhoons and monsoonal rains. These findings provide actionable insights for flood-risk assessment and emphasize the importance of region-specific mitigation strategies to enhance disaster preparedness across Japan.

## Reference

[1] Y. Miyabuchi, M. Torii, Landslide Disaster Triggered by July 2020 Heavy Rainfall in the Southern Part of Kumamoto Prefecture, Southwestern Japan, J. Geogr. (Chigaku Zasshi). 130 (2021) 107–116.
[2] H. Lee, K. Calvin, D. Dasgupta, G. Krinner, A. Mukherji, P. Thorne, C. Trisos, J. Romero, P. Aldunce, K. Barret, IPCC, 2023: Climate Change 2023: Synthesis Report, Summary for Policymakers. Contribution of Working Groups I, II and III to the Sixth Assessment Report of the Intergovernmental Panel on Climate Change [Core Writing Team, H. Lee and J. Romero (eds.)]. IPC, (2023).
[3] D. Hatsuzuka, T. Sato, Future Changes in Monthly Extreme Precipitation in Japan Using Large-Ensemble Regional Climate Simulations, J. Hydrometeorol. 20 (2019) 563–574.
[4] S. Watanabe, N. Utsumi, T. Kitano, E. Nakakita, A Discussion on Extreme Precipitation Under 2° C and 4° C Warming in d4PDF Focusing on the Inversion of Future Change, J. Japan Soc. Civ. Eng. Ser. B1 (Hydraulic Eng. 77 (2021) 1279–1284.
[5] H. Kawase, M. Nosaka, S.I. Watanabe, K. Yamamoto, T. Shimura, Y. Naka, Y.-H. Wu, H. Okachi, T. Hoshino, R. Ito, S. Sugimoto, C. Suzuki, S. Fukui, T. Takemi, Y. Ishikawa, N. Mori, E. Nakakita, T.J. Yamada, A. Murata, T. Nakaegawa, I. Takayabu, Identifying Robust Changes of Extreme Precipitation in Japan From Large Ensemble 5-km-Grid Regional Experiments for 4K Warming Scenario, J. Geophys. Res. Atmos. 128 (2023) e2023JD038513.
[6] S. Coles, An introduction to statistical modeling of extreme values, Springer, London, 2001.
[7] A.C. Davison, R.L. Smith, Models for Exceedances Over High Thresholds, J. R. Stat. Soc. Ser. B. 52 (1990) 393–425.
[8] A. Langousis, A. Mamalakis, M. Puliga, R. Deidda, Threshold detection for the generalized Pareto distribution: Review of representative methods and application to the NOAA NCDC daily rainfall database, Water Resour. Res. 52 (2016) 2659–2681.
[9] G.M. Ljung, G.E.P. Box, On a measure of lack of fit in time series models, Biometrika. 65 (1978) 297–303.
[10] J.R.M. Hosking, L-moments: Analysis and estimation of distributions using linear combinations of order statistics, J. R. Stat. Soc. Ser. B. 52 (1990) 105–124.
[11] W.Z. Wan Zin, A.A. Jemain, K. Ibrahim, The best fitting distribution of annual maximum rainfall in Peninsular Malaysia based on methods of L-moment and LQ-moment, Theor. Appl. Climatol. 96 (2009) 337–344.

# Flood Inundation Forecasting using Deep Learning Models

Weeraphat DUANGKHWAN[1] , ○Chaiwat EKKAWATPANIT[1*], Chanchai PETPONGPAN[1]& Duangrudee KOSITGITTIWONG[1]

[1]Department of Civil Engineering, King Mongkut's University of Technology Thonburi, Bangkok 10140, Thailand.

[*]E-mail: chaiwat.ekk@kmutt.ac.th

## Abstract

Effective flood prediction is crucial for disaster preparedness and mitigation. This study applies deep learning techniques, including Gated Recurrent Units (GRU), Long Short-Term Memory (LSTM) networks, and Convolutional Neural Networks (CNNs), to enhance flood forecasting in the Pattani River Basin. By integrating reservoir release flow, water level, and tidal data, these models aim to improve the accuracy of water level predictions and flood inundation mapping. The GRU and LSTM models were assessed across four scenarios with lead times of up to 24 hours, using Root Mean Squared Error (RMSE) and Nash-Sutcliffe Efficiency (NSE) as evaluation metrics. GRU models consistently outperformed LSTM models when all variables were considered, with LSTM models showing slightly higher RMSE and lower NSE values. For flood inundation mapping, CNNs trained on Sentinel-1 GRD imagery demonstrated the highest True Positive Rates (TPR) when integrating all variables, highlighting the importance of diverse data inputs. This research presents a computationally efficient, real-time flood prediction framework that delivers high accuracy, offering valuable insights for water resource management and flood risk reduction.

**Keywords:** Flood inundation; Flood forecast; Pattani Basin; Deep Learning; Sentinel-1.

## 1 Introduction

Flooding continues to be one of the world's most destructive natural disasters, inflicting significant environmental, economic, and social damage. The development of effective early warning systems and disaster management strategies hinges on two critical capabilities: accurate water level forecasting and the timely identification of flood-prone areas. Conventional approaches, such as rainfall-runoff and hydrodynamic models, are often inadequate for this task due to their demanding data requirements and computational intensity, rendering them impractical for real-time deployment.

Furthermore, mapping flood inundation presents its own set of challenges, primarily due to the scarcity of reliable ground observations. Although remote sensing, particularly cloud-penetrating Synthetic Aperture Radar (SAR) from satellites like Sentinel-1has revolutionized flood detection, automated systems that leverage this data often face limitations in temporal resolution.

To overcome these dual challenges of predictive modeling and spatial mapping, this study proposes a novel integrated deep learning framework for the Pattani River Basin. Our approach synergistically combines LSTM, GRU, and CNN architectures to simultaneously forecast water levels and predict flood inundation. The model integrates diverse data streams, including upstream discharge, river water levels, tidal data, and satellite imagery, to achieve a computationally efficient and accurate system designed specifically for real-time flood risk assessment and decision-making.

## 2 Study area and methods

This study focuses on the Pattani River Basin in southern Thailand. The watershed spans approximately 219 km², predominantly within Yala Province (94.43%), with the remainder in Pattani Province (5.27%). The 210 km-long Pattani River is divided into upper and lower sections. As Pattani Province experiences the most severe flooding, it served as the primary area of investigation (Fig. 1).

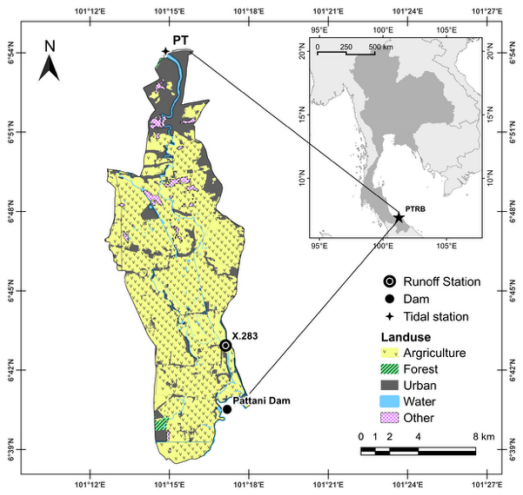


**Fig. 1 Study Area**

We developed an integrated deep learning framework to forecast river water levels and predict flood inundation. The models utilized input parameters including reservoir release flow, river water levels, and tidal levels.

**Water Level Forecasting:** Gated Recurrent Unit (GRU) and Long Short-Term Memory (LSTM) models were evaluated for their ability to forecast water levels across four different input scenarios (Fig. 2a).

**Flood Inundation Mapping:** A Convolutional Neural Network (CNN) model was employed to predict flood extents, using classified inundation maps derived from Sentinel-1 Ground Range Detected (GRD) imagery as the target output (Fig. 2b).

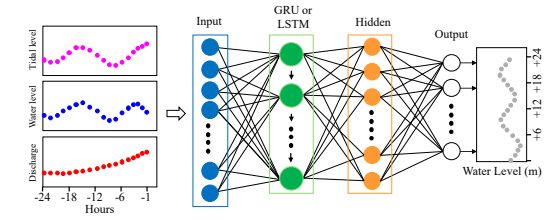


(a) Water level

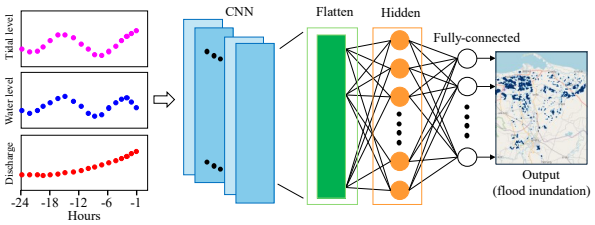


(b) Flood inundation map

**Fig.2 Structure of Flood Prediction Model**

## 3 Results and discussion

3.1 Water Level Prediction Model

Water level forecasting employed deep learning to model time-series data. To overcome the vanishing gradient problem inherent in standard Recurrent Neural Networks (RNNs), we implemented and compared Long Short-Term Memory (LSTM) and Gated Recurrent Unit (GRU) models. The GRU architecture offers a simplified alternative to the LSTM, utilizing an update gate instead of separate forget and input gates, which reduces parameters and training time.

Both models were configured with a single layer of 256 units. They were trained on a 70/30 split of data from 2019–2021, using a 24-hour sequence of historical data (reservoir release, river water level, and tidal level) to forecast future water levels. Model performance across different lead times was evaluated using Root Mean Square Error (RMSE) and Nash-Sutcliffe Efficiency (NSE) across four scenarios.

GRU models demonstrated superior performance during testing across all scenarios and lead times, despite LSTM showing a slight advantage during training. For instance, in Scenario 1 (SCN1), GRU achieved an RMSE of 0.17m at T+1, compared to 0.19m for LSTM. Scenarios 2 and 4 (SCN2-GRU and SCN4-GRU) yielded the best results, with SCN4-GRU achieving an RMSE of 0.08m at T+1.

3.2 Flood Inundation Prediction Model

For flood inundation mapping, a raster-based approach using a 1D Convolutional Neural Network (CNN) was developed. The model, comprising a single convolutional layer and two dense layers, used input features to predict flood maps derived from Sentinel-1 SAR imagery (100m resolution). The dataset of 93 images was split into 65 for training and 28 for testing.

Model performance was evaluated using the True Positive Rate (TPR) for flooded and non-flooded areas. Scenario 4 (SCN4), which integrated all input parameters (release flow, water level, tidal level), achieved the best performance with a TPR of 99.25% for non-flooded areas and 76.47% for flooded areas. A visual comparison between a predicted map and its corresponding Sentinel-1 observation from July 16, 2020, confirms the model's accuracy (Fig. 3).

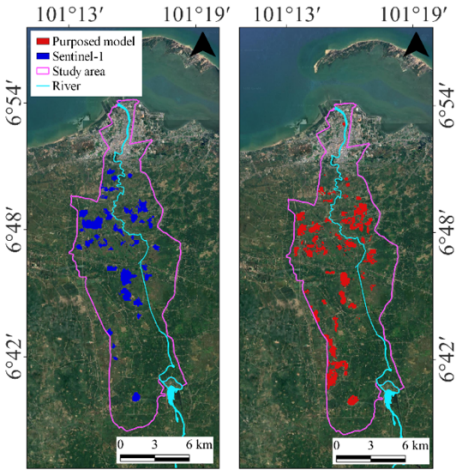


**Fig. 3 Comparison of flood inundation maps derived from Sentinel-1 SAR imagery and CNN results.**

## 4 Conclusion

This study confirms the efficacy of deep learning for flood prediction. The GRU model excelled in water level forecasting, while the CNN model achieved high accuracy in flood inundation mapping; both performed best when integrating release flow, water level, and tidal data.

These findings can enhance flood warning systems and risk management through more accurate, timely forecasts. Future work should focus on enabling long-term predictions and improving model accuracy by integrating additional data sources and refining neural architectures.

## Reference

[1] Yang, Q., Shen, X., Anagnostou, E. N., Mo, C., Eggleston, J. R., & Kettner, A. J., 2021. A high-resolution flood inundation archive (2016–the present) from Sentinel-1 SAR imagery over CONUS. Bulletin of the American Meteorological Society, 102(5), 1064-1079.

[2] Clement, M. A., Kilsby, C. G., & Moore, P., 2017. Multi-temporal synthetic aperture radar flood mapping using change detection. Journal of Flood Risk Management, 11(2), 152-168.

[3] Hieu, T. T., Chieu, T. Q., Quang, D. N., & Hieu, N. D., 2023. Water level prediction using deep learning models: A case study of the Kien Giang River, Quang Binh Province. River, 2(4), 468-473.

# An Assessment of Water Resources and Management in Bueng-Kan Province, Thailand: Sub-Mekong River Basin

Weerayuth PRATOOMCHAI*
Department of Civil Engineering, Faculty of Engineering, King Mongkut's University of Technology North Bangkok, Bangkok, Thailand
*E-mail: weerayuth.p@eng.kmutnb.ac.th

## Abstract

Bueng-Kan is the latest province in Thailand. It was located in Northeastern region, approximately 750 km faraway from Bangkok, and it is a tributary of the Mekong River basin. Based upon the observed data, there is 486 MCM (Million Cubic Meters) in total runoff volume. This study shows 88 MCM of water volume is annually water demand and will increase to 92.5 MCM in the next 20 years. Approximately13 MCM/year was found as the water shortage due to insufficient control structures for managing the natural water resources. In addition, the projections of changing climate show increasing in total rainfall and its intensity. Therefore, both water shortage and overwhelming flood-runoff in the dry and wet seasons are expected in the future. Using multiple-criteria analysis (MCA), eight water resources development projects are evaluate and proposed for Bueng-Kan for alleviating nowadays water stress and coping with the uncertainty accelerating by climate change.

**Keywords:** Climate change; Multiple-criteria analysis; Water Resources Assessment; Thailand.

## 1 Introduction

Flood and drought are two of the most natural disasters and dilemma water problems in Thailand, resulting in socioeconomic, ecological, and infrastructure damages [1]. These situations are worse in a remote area and lack of structural measures. The province named Bueng-Kan, the latest province of Thailand, is now facing with both uncontrol water surplus and unallocated water to meet the requirement in the wet and dry seasons.

Bueng-Kan province covers the area of 4,004 km$^2$ and is divided into 6 sub-basins. Office of the National Water Resources (ONWR) [2], in 2023 there were approximately 425,000 people living in this province and 80% of people living in agricultural sectors, e.g., rubber tree and paddy field (rainfed area). Thus, climate and proper amount of rainfall are two most important factors for the people and province productions. Using the latest last 30-year data, 2,170 mm is an average annual rainfall (89% and 11% are accounted in the wet and dry seasons, respectively). Due to the fact that huge temporal distribution of rainfall from season to season, river flood and dry-up water are main problems of water disaster. There is no dam-reservoir in this area and the changing climate is potential to amplify the imbalance water resources.

The aim objectives of this study are vividly understanding current water resources status and projections into the future using the advancement of mathematical models for proposing strategic water-managing plans/projects.

## 2 Materials and methods

The main data (**Table 1**) that were used in this study were provided by Royal Thai Irrigation Department (RID), Thai Metrological Department (TMD), Department of Groundwater Resources (DGR), Office of the National Economic and Social Development Council (ONESDC), and on-site survey. Under climate change conditions, forcing climate data were obtained from National Institute for Environmental Studies, Japan. Brief details of data used show in **Table 1**.

**Table 1 Data used**

| No. | Description | Stations/Points | Data source |
|---|---|---|---|
| 1 | River-runoff | 6 | RID |
| 2 | Climatological data | 22 | TMD |
| 3 | Geological data | Shapefile | DGR |
| 4 | Socioeconomic data | District | ONESDC |
| 5 | Future Climate data | Gridded data | CMIP5 |
| 6 | Flood and drought situations/ | Sub-district | On-site survey |

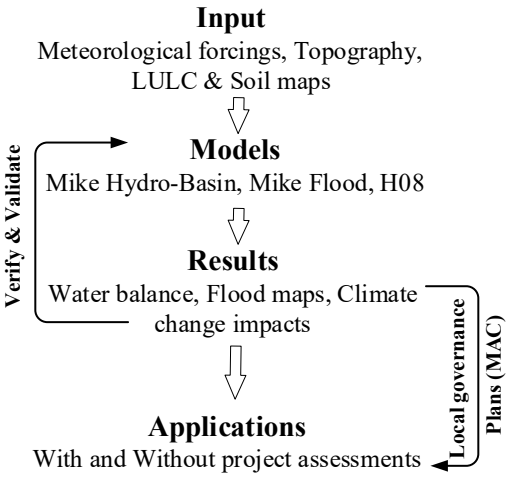


**Fig.1 Schematization of the study**

**Fig.1** shows the schematic procedures of this study. Input data were outlined in **Table 1**, and 3 mathematical models, namely, Mike Hydro-basin, Mike Flood and H08 models [3] were carried out for assessing status of water resources, flood

maps, and future climate change impacts, respectively. The models were verified and validated with available observed data, e.g., river discharge and on-site survey. Validated model parameters and MCA [4] were then applied for evaluating local governance water resources plans.

## 3 Results and discussion

The mathematical model of water balance showed 88 MCM of water volume is needed as the annual water demand for present condition. Under the impact of climate change, the total water demand will increase to 92.5 MCM annually, on average. In fact, this area has received 2,170 mm of rainfall that is above the country-rainfall average (1,250 mm) resulting by 486 MCM of runoff volume, but about 13 MCM/year was discovered as the average water shortage. The figure shows runoff volume is much more than the water demand (about 5.5 times), this shortage is due to extremely temporal distribution of precipitated water in the rainy and dry season. At present condition, there is no dam-reservoir for alleviating the water shortage.

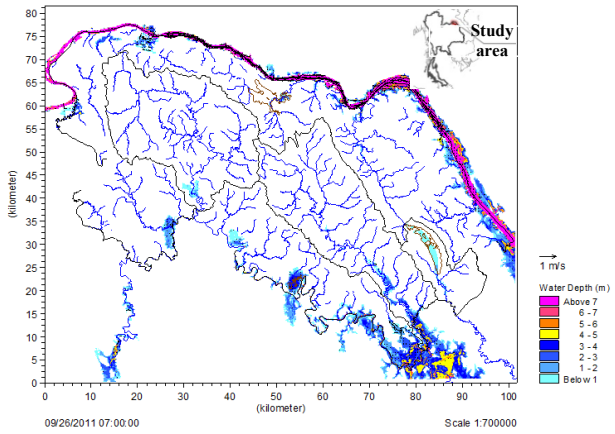


**Fig.2 Flood map simulation (2011 event)**

From May to October (wet season), especially for August to September, Bueng-Kan area is hit by tropical monsoon causing river flood across the province. The model results showed 510 km$^2$ (12.7% of total area) is subjected by flood inundation. This finding shows good agreement with the satellite data by GISDHA.

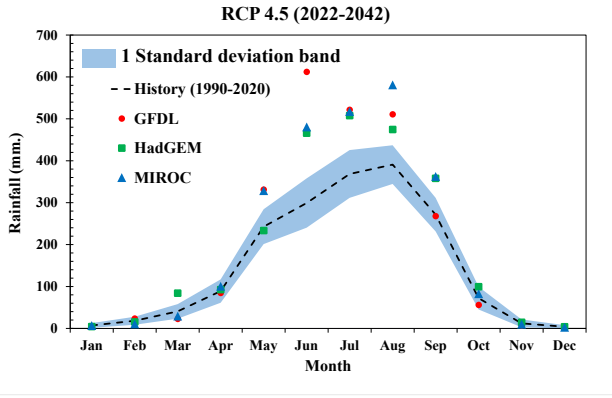


**Fig.3 Rainfall change under multiple GCMs (RCP 4.5)**

Using the ensemble average of climate change projection models (3 GCMs and 2 scenarios - RCP 4.5 and RCP 8.5) over the period 2022-2042, rainfall will increase by 180 mm in rainy season and no significant changing in the dry season (**Fig. 3**). And the projection of runoff (**Fig.4**) shows similar to the rainfall patterns. One standard deviation band using historical data were provided for comparing the degree of changing.

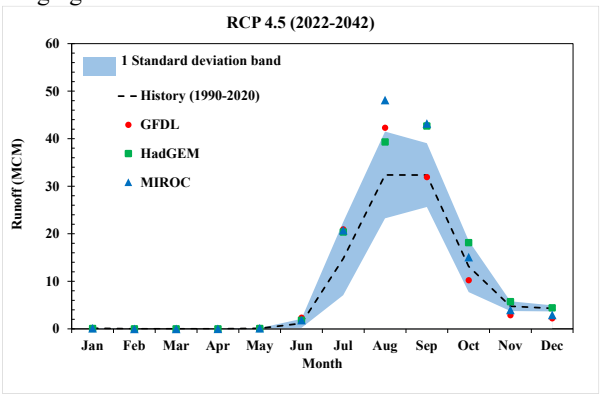


**Fig.4 Runoff change under multiple GCMs (RCP 4.5)**

For coping with the uncertainty of water resources in Bueng-Kan province, MCA [4] or weighting technique was applied in this stage. Engineering (40%), environmental (30%), and socioeconomic (30%) factors were considered. Because of this study focused on research and willing to implement, field survey and existing local governance water-resources plans were investigated (**Fig.5**). From 428 of total water projects in Bueng-Kan area, the first 8 areas (projects) with highest score suggesting by MCA were figure out.

**Fig.5 Public hearing for the propose projects**

## 4 Conclusions

This paper focus on current, future, and how to manage water resources for sustaining water security in a remote area of Thailand. The status of water resources including climate change impacts on rainfall and runoff are investigated. Field survey also used for identifying an appropriate water-resource projects supporting by the people.

## Reference

[1] Pratoomchai, W., Ekkawatpanit, C., Yoobanpot, N., Lee, K.T. A Dilemma between Flood and Drought Management: Case Study of the Upper Chao Phraya Flood-Prone Area in Thailand. Water, 2022.

[2] Office of the National Water Resources. Integrated water resources management plans in Bueng-Kan province (In Thai), 2023.

[3] Hanasaki N, Kanae S, Oki T, Masuda K, Motoya K, Shirakawa N, Shen Y, Tanaka K. An integrated model for the assessment of global water resources Part1: Model description and input meteorological forcing. Hydrology and Earth System Sciences 12:2008.

[4] Ahmad I, Verma MK, Application of Analytic Hierarchy Process in Water Resources Planning: A GIS Based Approach in the Identification of Suitable Site for Water Storage, Water Resources Management, 2018.

# Seasonal Variability and Climate Influence on Water Quality Parameters in the Kelani River Basin, Sri Lanka: A Two-Decade Analysis

○ Chaminda SP[1*] , Ekanayaka GEPP[1], Surabiga T[1], Wimalasena SGDM[1], and Gunawardhana HGLN[2]

[1]Department of Earth Resources Engineering, University of Moratuwa, Sri Lanka.
[2]Department of Civil Engineering, University of Moratuwa, Sri Lanka.

[*]E-mail: chaminda@uom.lk.

## Abstract

The Kelani River, Sri Lanka's critical freshwater source supplying over 80% of the drinking water for the capital, has experienced significant water quality degradation due to seasonal climate variability and land use changes. This study investigates monsoon-driven impacts on water quality from 2003 to 2023 across upstream, midstream, and downstream segments using GIS analysis and statistical correlation methods. Results reveal robust correlations between rainfall and turbidity, with coefficients ranging from 0.80 to 0.92 across all segments, establishing monsoon patterns as the primary driver of sediment transport. The Southwest Monsoon consistently delivered the highest rainfall, reaching 1035.67 mm upstream in 2019, coinciding with severe turbidity exceedances. Temperature showed significant positive correlations with biological oxygen demand at 0.73 midstream and 0.72 upstream, reflecting enhanced microbial decomposition during warmer periods. A spatial temperature gradient of 6-8°C from upstream to downstream creates distinct biogeochemical zones influencing oxygen dynamics. Land use analysis revealed dramatic transformations: downstream urbanization increased by around 25% while vegetation declined by around 20%, midstream agricultural land expanded by 24%. These changes have amplified seasonal water quality impacts by reducing natural buffering capacity. The synergistic interaction between intense Southwest Monsoon rainfall, elevated temperatures, and vegetation loss creates acute water quality crises during peak monsoon periods. The study demonstrates that effective watershed management requires season-specific strategies addressing monsoon-driven pollution dynamics, temperature effects on biological processes, and land use planning to restore natural buffering capacity in this monsoon-dominated tropical river system.

**Keywords:** Seasonal Variability; Monsoon Impact; Water Quality; Climate Change; LULC; Kelani River Basin

## 1 Introduction

Tropical rivers in monsoon regions show strong seasonal variations in flow, sediment, and pollutants. Understanding these dynamics is vital as climate change intensifies monsoon patterns and alters temperatures [1]. The Kelani River in Sri Lanka, which supplies water to over four million people, faces such challenges across four distinct monsoon periods. Originating from the Sri Pada Range, it flows 144 km through diverse landscapes, receiving about 2,400 mm of annual rainfall [2], [3], [4], [5]. Discharge ranges from 20–25 $m^3/s$ in dry seasons to over 1,500 $m^3/s$ during peak monsoons, with water quality affected by urbanization, agriculture, and vegetation loss[6].

This study investigates how rainfall, temperature, and land use changes influence key water quality parameters—turbidity, DO, BOD, COD, EC, and nutrients—across the river's segments over two decades, aiming to support climate-resilient watershed management.

## 2. Methodology

Water quality data (2003–2023) from the Central Environmental Authority were analyzed across nine Kelani River stations—upstream, midstream, and downstream. Ten parameters, including pH, turbidity, DO, BOD, COD, and nutrients, were examined for selected years (2003, 2007, 2011, 2015, 2019, 2023) based on data completeness and satellite availability.

Rainfall and temperature data from the Department of Meteorology were organized by monsoon season and spatially interpolated using Ordinary Kriging in ArcGIS Pro. Landsat imagery (TM and OLI/TIRS) was classified into five land cover types—developed, vegetation, agriculture, water, and others—with over 80% accuracy.

Pearson correlation analysis, conducted in Python, assessed relationships between climate, land use, and water quality across river segments, identifying significant seasonal and spatial patterns ($p < 0.05, 0.01$).

## 3. Results

### *3.1 Seasonal Climate Patterns*

The Southwest Monsoon contributed the highest rainfall in the upstream and midstream regions, reaching 1,035.67 mm, while the lowest rainfall was recorded in the upstream area during the First Inter-Monsoon of 2019, with only 206.82 mm. Downstream areas showed different patterns, with the Second Inter-Monsoon occasionally producing the highest rainfall at 773.63 mm. There was notable year-to-year variation in rainfall, with the Southwest Monsoon ranging from just 438.68 mm in 2011 to as high as 1,044.45 mm in 2007 in the upstream region, posing major challenges for water management.

Temperature exhibited a consistent 6-7 degree Celsius spatial gradient. During the Southwest Monsoon, upstream temperatures ranged 21.9-22.1°C, midstream 25.5-25.9°C, and downstream 28.0-28.3°C. Gradual warming trends appeared, particularly downstream, where 2019 recorded the highest temperatures.

### *3.2 Water Quality Variations*

Turbidity consistently exceeded standards during high rainfall, with 2011 and 2019 showing severe exceedances over 70 NTU at midstream and downstream stations during peak monsoon flow, demonstrating direct rainfall-sediment linkages. Dissolved oxygen maintained acceptable levels upstream but occasionally fell below 5 mg/L downstream during 2007. Biochemical oxygen demand remained low upstream at 1-2 mg/L but showed multiple exceedances downstream during 2003, 2007, and 2019, with elevated midstream values during 2007 and 2011.

Chemical oxygen demand paralleled biochemical oxygen demand with basin-wide spikes in 2007. Electrical conductivity and chloride exhibited dramatic spatial contrasts, with extreme downstream elevations at Japanese Friendship Bridge indicating industrial discharges and potential saltwater intrusion. Phosphate increased progressively downstream, peaking in 2015 but remaining within limits. Nitrate stayed consistently low despite extensive agriculture. pH remained stable between 6.5-8.5 throughout.

### *3.3 Land Use Changes*

Upstream developed land increased 3% while vegetation declined to 12%. Midstream experienced dramatic change with developed land rising 8% and agriculture expanding from 31% to 56%, while vegetation dropped from 62% to 30%. Downstream urbanization increased 25% with vegetation plummeting from 31% to 9%.

### *3.4 Climate–Water Quality Correlations*

Rainfall showed strong positive links with turbidity (up to $r = 0.92$ midstream, $p<0.01$), confirming it as the main factor driving sediment loads. It also correlated with higher BOD ($r = 0.58–0.67$) and COD ($r = 0.62$–downstream), suggesting rainfall-driven transport of organic matter. In contrast, electrical conductivity and chloride showed negative correlations ($r = –0.53$ to $–0.64$), indicating dilution during high rainfall.

Temperature correlated positively with BOD ($r \approx 0.72–0.73$, $p<0.01$), reflecting increased microbial activity, while DO showed weak negative trends due to lower oxygen solubility at higher temperatures. Overall, BOD was the most temperature-sensitive parameter ($r = 0.61$, $p<0.05$).

### *3.5 Land Use–Water Quality Correlations*

Developed areas had strong positive correlations with nutrients (nitrate $r = 0.91$, phosphate $r = 0.86$) and ions such as chloride and EC ($r \approx 0.89–0.95$). Vegetation showed the opposite trend, improving DO ($r = 0.76$) while reducing BOD, chloride, and EC. Agricultural land increased nutrient levels (nitrate $r = 0.96$, phosphate $r = 0.97$) but reduced DO ($r = –0.51$), highlighting its contribution to nutrient enrichment and oxygen depletion.

## 4. Discussion

Strong rainfall–turbidity correlations (0.80–0.92) confirm that monsoon rainfall is the main driver of sediment transport in the Kelani River. Heavy Southwest Monsoon rains exceeding 1000 mm cause intense runoff, soil erosion, and sediment movement downstream, while midstream areas are especially sensitive due to agricultural disturbance and vegetation loss. Rainfall also increases organic matter loads, raising BOD and COD levels, whereas dilution during heavy rains lowers conductivity and chloride temporarily. The downstream area shows stronger COD correlations because urban runoff carries accumulated pollutants during monsoon events.

Temperature strongly influences biological processes, with significant positive correlations (0.72–0.73) between temperature and BOD, indicating faster microbial activity at higher temperatures. Cooler upstream waters maintain better oxygen levels, while warmer downstream waters (26–28°C) face oxygen depletion. Although the temperature–DO relationship is not statistically significant, it still reflects oxygen loss at higher temperatures, partially offset by photosynthesis and natural aeration.

Land use changes have further intensified water quality problems. Vegetation loss—up to 25% downstream—has weakened natural buffering, increasing erosion and nutrient runoff. Vegetated areas generally improve DO and reduce BOD, chloride, and EC. Meanwhile, rapid development (20% increase downstream) and expanding agriculture (around 24% midstream) have increased pollutant and nutrient inputs, making the river more sensitive to rainfall events.

Climate and land use factors together amplify water quality degradation. Intense monsoon rains on cleared or cultivated lands wash sediments and organic matter into the river, while high temperatures boost decomposition and oxygen demand. The Southwest Monsoon period,

both warm and wet, produces the worst conditions—extreme turbidity, high nutrients, and low oxygen—as recorded in 2011 and 2019. In contrast, dry seasons reduce oxygen, creating different but equally severe challenges.

Looking ahead, climate change is expected to worsen these issues. Stronger monsoons and rising temperatures will increase sediment transport, organic pollution, and oxygen stress. Even a 1–3°C rise could push downstream areas beyond ecological limits. Observed warming of about 0.3°C since 2003 suggests that water temperatures may exceed 30°C within a few decades, further threatening aquatic life. Increasing rainfall variability will also cause more frequent extreme events, highlighting the need for adaptive watershed management and improved water treatment systems.

## 5. Conclusions and Recommendations

This study confirms that monsoon rainfall is the main factor shaping water quality in the Kelani River, showing very strong links with turbidity (0.80–0.92) and BOD (0.58–0.67). Temperature also plays an important role, increasing microbial activity and oxygen demand (0.72–0.73). Land use changes—especially major vegetation loss (up to 25%) and rapid urban growth (over 20%) further worsen seasonal impacts by reducing natural protection and increasing pollution sources.

Water quality gradually declines from the clean upstream areas to heavily impacted downstream regions, mainly due to monsoon-driven runoff and pollution transport. The combined effects of intense rainfall, high temperatures, and land disturbance create severe water quality issues during peak monsoon periods. Effective management should be both seasonal and location-specific. Pre-monsoon periods are ideal for maintenance and erosion control, while the Southwest Monsoon requires strong monitoring and strict pollution control. Post-monsoon seasons should focus on restoration and planning. Midstream areas need erosion and agricultural land management, downstream zones require urban and industrial controls, and upstream areas should be protected from future development.

## References

[1]A. A. D. Bello, N. B. Hashim, and M. R. M. Haniffah, "Predicting impact of climate change on water temperature and dissolved oxygen in tropical rivers," Climate, vol. 5, no. 3, 2017, doi: 10.3390/cli5030058.

[2]A. G. S. N. Rathnayake, R. Luxman, N. A. P. Udayanga, S. P. Chaminda, W. C. A. Ishankha, and L. Gunawardhana, "Assessment of Seasonal and Spatial Water Quality Changes in Kelani River, Sri Lanka," Moratuwa, 2024.

[3]H. Sawmika, G. Thusitha, and M. Samarakoon, "Impact of Land Use on Water Quality of Kelani River," KDUIRC-2019, 2019, Accessed: Mar. 24, 2025. [Online]. Available: http://ir.kdu.ac.lk/handle/345/2234

[4]N. M. DE. A. Abeysinghe and M. B. Samarakoon, "Analysis of Variation of Water Quality in Kelani River, Sri Lanka," International Journal of Environment, Agriculture and Biotechnology, vol. 2, no. 6, pp. 2770–2775, 2017, doi: 10.22161/ijeab/2.6.1.

[5]K. D. C. R. Dissanayaka and R. L. H. L. Rajapakse, "Long-term precipitation trends and climate extremes in the Kelani River basin, Sri Lanka, and their impact on streamflow variability under climate change," Paddy and Water Environment, vol. 17, no. 2, pp. 281–289, Apr. 2019, doi: 10.1007/s10333-019-00721-6.

[6]R. Makubura, D. P. P. Meddage, H. M. Azamathulla, M. Pandey, and U. Rathnayake, "A Simplified Mathematical Formulation for Water Quality Index (WQI): A Case Study in the Kelani River Basin, Sri Lanka," Fluids, vol. 7, no. 5, May 2022, doi: 10.3390/fluids7050147.

# Flood Resilience and Community Safety: Insights from a Case-study in the Kelani Basin, Sri Lanka

○Nilupul GUNASEKARA[1*], Sanduni ASHVINI[1], Kumari FERNANDO[1] & Raj PRASANNA[2]
[1]Department of Civil Engineering, General Sir John Kotelawala Defence University, 10390 Sri Lanka.
[2]Joint Centre for Disaster Research, Massey University, Wellington, New Zealand.
[*]E-mail: nilupul.gunasekara@kdu.ac.lk

## Abstract

This study highlights the community flood resilience measures employed in the Kaleni River Basin of Sri Lanka which was selected as a case-study due to the socio-economic significance of the basin. These resilience measures were evaluated by a Flood Resilience Index (FRI) which considers five dimensions: natural, physical, social, economic, and institutional, supported by 29 indicators. Appropriate measures for each area were selected based on geophysical conditions and their local flood types, for the selected Grama Niladhari Divisions, which include the National Flood Insurance Programme for Megoda Kolonnawa, elevated housing units for Pahala Bomiriya, and the Sponge City for Kerawalapitiya. All three GNDs showed increased FRI values when the resilience measure was in-place, compared to the scenario of not having it. The developed FRI can be used as a baseline for decision making on selection of different flood resilience measures in disaster management, in different parts of the world.

**Keywords:** Community Flood Resilience Index, Flood Insurance, Sponge City, Resilience Measures.

## 1 Introduction

Kelani River Basin (KRB) is the most flood-prone river in Sri Lanka which runs through Nuwara Eliya, Ratnapura, Kegalle, Gampaha, and Colombo [1; 2]. The lower KRB has a long history of flooding, and the region's socio-economic landscape is significantly impacted by flooding, primarily driven by heavy monsoon rains that cause the river to overflow its banks, inundating the surrounding areas [3]. The most significant flood event in recent history occurred in May 2016, affecting over one million people, resulting in approximately 100 fatalities and another 100 reported missing [4]. The KRB is home to more than 25% of the country's population and supplies around 80% of the drinking water for the greater Colombo area [1].

On top of these, Samarasinghe et al. [4] have shown that the basin is experiencing changes in climate extremes, which could exacerbate existing environmental and socio-economic challenges. Effective management strategies are essential to mitigate these impacts and ensure the long-term sustainability of the river basin [5]. Structural measures such as dams, levees, minor flood protection schemes, and flood bunds are ageing due to insufficient maintenance and upgrades [6]. The deterioration of these structures can lead to failures during critical flood events, exacerbating the impact on the community who has no other option than living with floods. Unplanned and unauthorized developments in flood-prone areas increase the risk of flooding. While effective land use planning and legislation can mitigate flood risk, the implementation of these measures remains a persistent challenge in densely populated river basins [7] such as KRB. Community involvement in flood risk management is essential for building resilience. However, a lack of awareness and preparedness among the public is often evident. Flood resilience refers to the capacity of communities, infrastructure, and ecosystems to anticipate, prepare for, respond to, and recover from flooding [8]. It encompasses a range of strategies and measures designed to mitigate the impacts of floods and facilitate swift recovery. This study identified the most plausible flood resilience measured the flood-prone communities adopt to enhance individual and community resilience. A flood resilience index (FRI) was employed to evaluate the effectiveness of the flood resilience measures considering with and without scenarios. The FRI also provides a baseline in community flood resilience for disaster management planning.

## 2 Materials and methods

**Fig. 1. The three GNDs chosen in KRB.In yellow-egoda Kolonnawa, in orange- Kerawalapitiya and in red-Pahala Bomiriya (The figure is nt to scale)**

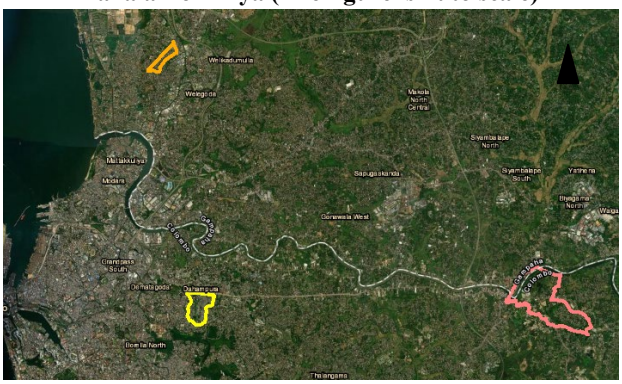

Megoda Kolonnawa, Pahala Bomiriya, and Kerawalapitiya are the selected highly flood-vulnerable Grama Niladari Divisions (GNDs) within the lower Kelani River Basin, evaluated against flood damage data and affected community data using the Analytical Hierarchy Process. Furthermore, flood-affected areas and flood-related causes were identified through a literature survey and analysis of rainfall patterns, Land Use and Land Cover changes, comparisons of flood inundation extents, and flood depth records at the Nagalagam Street gauging station during past severe flood events.

**Fig. 2. The composite FRI evaluated at the chosen three GNDs under the scenarios with (FRI_After) and without (FRI_Before) the flood resilience measures**

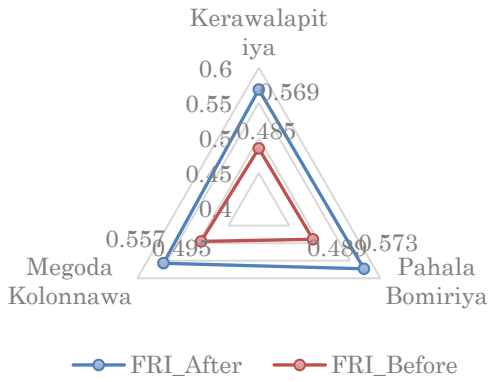


The National Flood Insurance Programme, the construction of elevated housing units, and the Sponge-City Concept were identified as flood resilience measures that can be easily adapted to the selected case study areas, enhancing the community's flood resilience through a comprehensive literature review.

Appropriate measures for each area were selected based on geophysical conditions and their local flood types, which include the National Flood Insurance Programme for Megoda Kolonnawa, elevated housing units for Pahala Bomiriya, and the Sponge City for Kerawalapitiya. These findings were validated using feedback from Grama Niladhari and disaster management officials.

Primarily, the methods employed include interviews, questionnaire surveys, and the development of a hydraulic model. The development of Community Flood Resilience Indices is based on five dimensions: natural, physical, social, economic, and institutional, supported by 29 indicators. Subsequently, it was decided to conduct questionnaire surveys among 120 households across all three Grama Niladhari divisions as a research tool to evaluate community flood resilience indices for each division. The questionnaire was constructed to gather information on ten key areas, each defined by an indicator, namely: demography, flood awareness, flood-causing factors, flood mitigation, flood preparedness, flood response, flood recovery, flood impacts, rules and regulations, and suggestions for flood protection measures. Reliability checks for the developed questionnaire were conducted using Cronbach's Alpha, yielding a result of 0.66, which exceeds the threshold value of 0.5.

The same questionnaire was used to evaluate community flood resilience indices before and after implementing the flood resilience measures introduced during an awareness session on the proposed strategies in the communities of the chosen three GNDs.

## 3 Results and discussion

Megoda Kolonnawa, Pahala Bomiriya, and Kerawalapitiya flood resilience were significantly increased by the proposed flood resilience measures for each of the GNDs (**Fig. 2**)- Megoda Kolonnawa (from 0.495 to 0.557), Pahala Bomiriya (from 0.489 to 0.573), and Kerawalapitiya (from 0.485 to 0.569).

## 4 Conclusions

This research developed flood resilience index for the Kelani River Basin, with a focus on case study areas Megoda Kolonnawa, Pahala Bomiriya, and Kerawalapitiya, and proposes key flood resilience measures tailored to the specific needs of the Kelani River basin. The National Flood Insurance Programme for Megoda Kolonnawa, elevated housing units for Pahala Bomiriya, and the Sponge City for Kerawalapitiya were proven to be effective in enhancing resilience of these GNDs, evaluated by the FRI.

In conclusion, the developed indices can serve as a baseline for disaster management planning, and the same methodological approach can assist other regions in creating more flood-resilient environments for living with floods.

## Reference

[1] CRIP, Strategic Environmental Assessment of Development of River Basin Level Flood and Drought Mitigation Investment Plans-Kelani River Basin (2018).

[2] JICA, Data Collection Survey on Disaster Risk Reduction Sector in Sri Lanka, Final Report (2017).

[3] Gunasekara, I.P.A., Flood Hazard Mapping in Lower Reach of Kelani River, Vol. XXXXI, (2008).

[4] Samarasinghe, J.T., Makumbura, R.K., Wickramarachchi, C., Sirisena, J., Gunathilake, M.B., Muttil, N., Teo, F.Y., et al., "The Assessment of Climate Change Impacts and Land-use Changes on Flood Characteristics: The Case Study of the Kelani River Basin, Sri Lanka", Hydrology, MDPI, Vol. 9 No. 10 (2022b), doi: 10.3390/hydrology9100177.

[5] Samarasinghe, J.T., Basnayaka, V., Gunathilake, M.B., Azamathulla, H.M. and Rathnayake, U., "Comparing Combined 1D/2D and 2D Hydraulic Simulations Using High-Resolution Topographic Data: Examples from Sri Lanka—Lower Kelani River Basin", Hydrology, MDPI, Vol. 9 No. 2, (2022a) doi: 10.3390/hydrology9020039.

[6] Perera, C. and Nakamura, S., "Conceptualizing the effectiveness of flood risk information with a socio-hydrological model: A case study in Lower Kelani River Basin, Sri Lanka", Frontiers in Water, Frontiers Media S.A., Vol. 5, (2023), doi: 10.3389/frwa.2023.1131997.

[7] Herath, H.M.M., Wijesekera, S. and Munasinghe, & jagath. MANAGING OF URBAN FLOOD RISK IN COLOMBO WITH SPATIAL PLANNING, (2016).

[8] Raub, K.B., Flynn, S.E., Stepenuck, K.F. and Hedderman, C., "Integrating resilience and nexus approaches in managing flood risk", Frontiers in Water, Frontiers Media SA, Vol. 6, (2024). doi: 10.3389/frwa.2024.1306044.

# Hydro-morphological controls on suspended sediment dynamics in the Abukuma River watershed, Japan

○ Sheikh Hefzul BARI[1] & Yoshiyuki YOKOO[1,2,3]

[1]Graduate School of Symbiotic Science and Technology, Fukushima University, Fukushima 960-1296, Japan

[2]Hydrogen Energy Research Institute, Fukushima University, Fukushima 960-1296, Japan

[3]Institute of Environmental Radioactivity, Fukushima University, Fukushima 960-1296, Japan

*E-mail: shbari.bd@gmail.com.

## Abstract

Sediment transport, a crucial phenomenon in riverine environments, plays a vital role in supplying nutrients, impacting nearby livelihoods, and shaping landscapes. However, the availability of riverine sediment is significantly influenced by natural controlling factors such as hydrology and the morphology of the watershed. Like other rivers, the Abukuma River watershed in northeastern Japan exhibits strong geomorphic and climatic controls on the suspended sediment generation and transport. This study integrates morphometric, hydrological, and sediment analyses to evaluate how watershed form, lithology, and rainfall patterns influence suspended sediment behavior. Results indicate that the granitic terrain and mature geomorphology govern sediment availability, while increasing rainfall intensity drives episodic sediment pulses. Such episodic events are drivers of the large quantity of suspended sand transport. The onset and crude estimation of this sand transport are proposed by suggesting a threshold discharge derived from the event based hysteresis analysis of suspended sediment. The findings highlight the need to incorporate both watershed morphology and hydroclimatic extremes in sediment management within similar mountainous basins.

**Keywords:** sediment dynamic; hydrology; morphology; Abukuma river.

## 1 Introduction

Watershed morphology and hydrology jointly dictate sediment production, transport, and deposition processes [1, 2]. Morphometric characteristics determine the potential for erosion as well as offers insights into the geomorphic evolution of a basin [3, 4, 5]. Hydrological dynamics, particularly rainfall intensity and discharge variability, control sediment mobilization and downstream export [6].

In the Abukuma river watershed of Japan, hydrological extremes have raised concerns about sediment delivery to coastal zones. Recent research by authors indicates that suspended sediment, the primary component of total sediment load, undergoes significant transportation during extreme weather conditions.

Therefore, in this study, the hydro-morphological characteristics of the Abukuma River basin were investigated to understand their influence on suspended sediment transport behavior. This study is a reconnaissance of a broader research to understand and comprehend the estuarine suspended sediment dynamics, with a focus on the Abukuma River.

## 2 Materials and methods

Digital Elevation Model (DEM) data were obtained from the Shuttle Radar Topography Mission (SRTM) with a 30 m spatial resolution via the OpenTopography platform. Hourly discharge records for the Iwanuma observatory from 1990 to 2025 were obtained from the Water Information System of the Ministry of Land, Infrastructure, Transport and Tourism (MLIT). Additionally, hourly rainfall data for Fukushima station operated by the MLIT were collected.

Quality control procedures of data included bi-directional interpolation for rainfall gaps of ≤ 4 h and discharge gaps of ≤ 6 h. Where available, remaining missing discharge values after interpolation were reconstructed using a rating curve based on concurrent water level data. Stations with more than 5% missing rainfall data were excluded from further analysis. Homogeneity tests for the discharge records were conducted using the pyHomogeneity Python package, which the first author contributed to. Morphometric parameters were derived from the DEM data using QGIS.

Sediment behavior was examined through sediment rating curve (SRC), linking discharge to suspended sediment concentration (SSC). Threshold discharge derived from event hysteresis analysis was applied to distinguish fine suspended sediment and suspended sand supply.

## 3 Results and discussion

The Abukuma River watershed covers approximately 5,400 km², with elevations upto 1,972 m (Fig.1). The basin perimeter and length are 727.5 km and 130.8 km, respectively. The watershed is predominantly underlain by granitic rocks, which yield quartz, feldspar, and mica-rich soils. This lithology influences sediment grain composition, favoring fine textured suspended sediment supply.

The calculated hypsometric integral of 0.206 indicates a geomorphologically mature, highly eroded landscape. Alternating steep and gentle slopes along the longitudinal profile reflect geological control, promoting localized erosion and deposition zones. In such settings, mechanical and chemical weathering becomes dominant.

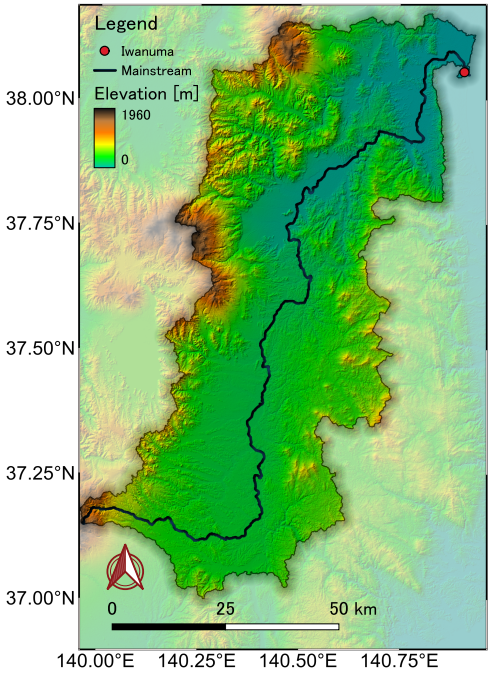


**Fig. 1. The Abukuma River watershed showing elevation and suspended sediment sampling location (red dot).**

Rainfall at Fukushima station averaged ~1,050 mm yr⁻¹ over 35 years, with interannual totals ranging from 707 mm to 1,401 mm. Maximum hourly rainfall averaged 27 mm, with extremes up to 56 mm. While annual rainfall totals exhibited a decreasing trend, maximum hourly intensities showed an increasing trend, suggesting a shift toward more extreme and localized events. These short-duration storms are major drivers of suspended sediment pulses, especially during wet seasons. The discharge shows a seasonal variation (Fig. 2) influenced by the typhoon season. The homogeneity test reveals a break point in the hourly discharge time series.

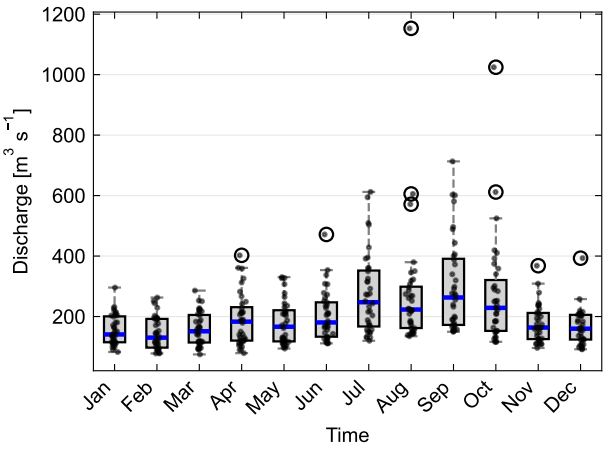


**Fig. 2. Monthly average discharge from 1990-2025 at Iwanuma sampling point. The circle indicates unusually high values.**

During intense rainfall events, sediment concentrations rise rapidly. Analysis revealed a complex hysteresis pattern for event-based SSC-discharge relationships. Based on the slope of the hysteresis loop, a threshold-based SRC is proposed. Such segmented rating curve offers the advantage of a more accurate fit and provides insights into the onset of sand transport.

## 4 Conclusions

The Abukuma River watershed exhibits a mature geomorphic structure characterized by granitic lithology and subdued relief, yet remains hydrologically dynamic. The morphological maturity and granitic substrate limit continious high sediment yield but response to the episodic events. This aligns with general understanding that decreasing mean rainfall with increasing intensity leads to more sporadic sediment delivery. Effective sediment management should therefore integrate both watershed morphology and changing rainfall extremes to predict and mitigate sediment driven hazards in similar mountainous systems.

## Reference

[1] Javed A, Hamshaw SD, Rizzo DM, Lee BS., Analysis of hydrological and suspended sediment events from Mad River watershed using multivariate time series clustering, ARXIV (2019).
[2] Joy MAR, Upaul S, Fatema K, Amin FMR., Application of GIS and remote sensing in morphometric analysis of river basin at the south-western part of great Ganges delta, Bangladesh, *Hydrology Research,* 6 (2023) 739–755.
[3] Sharma SK, Tignath S, Gajbhiye S, Patil R., Use of geographical information system in hypsometric analysis of kanhiya nala watershed, *International Journal of Remote Sensing & Geoscience,* 3 (2013) 30-35.
[4] Kumar S, Meshram S, Patil R, Tignath S., Hypsometric analysis using geographical information system of Gour River watershed, Jabalpur, Madhya Pradesh, India, *Current World Environment*, 1 (2016) 56-64.
[5] Abebe BK, Zimale FA, Gelaye KK, Gashaw T, Dagnaw EG, Adem AA., Application of hydrological and sediment modeling with limited data in the Abbay (Upper Blue Nile) basin, Ethiopia, *Hydrology,* 9 (2022) 167.
[6] Afolabi M., Long-term streamflow discharge from the Niger River Basin into the delta region, *Hydrological Sciences Journal,* (2025) 1038-1051.

# Fundamental Assessment of Failure Rates of Pre-Release in Virtual Reservoirs Representing Irrigation Reservoirs

○ Atsuya IKEMOTO 1*, So KAZAMA1
[1]Department of Civil and Environmental Engineering, Graduate of School of Engineering, Tohoku University, Miyagi 980-8579, Japan.*E-mail: ikemoto.atsuya.s1@dc.tohoku.ac.jp

## Abstract

In Japan, expectations for agricultural dams and irrigation ponds have increased as part of flood control strategies. However, pre-release operations without sufficient inflow raise risks for irrigation use. This study assessed failure rates tendencies of pre-release by applying long-term meteorological forecasts and water balance simulations. Using the d4PDF dataset (2000–2010), precipitation and six atmospheric variables were extracted, and a Support Vector Machine model generated forecasts up to 96 hours ahead. Forecasts for 55 years were concatenated to create an equivalent of 1,100 years. Based on a 100 mm rainfall threshold, 463 pre-release events were simulated. Most cases showed a 100% failure rates, with the lowest at 79.3%. Higher failure ratess occurred when full storage was released three days in advance, while larger catchment areas relative to irrigated areas reduced failure ratess. The study emphasizes balancing flood mitigation benefits with agricultural risks in future reservoir management.

**Keywords:** Irrigation reservoir, Pre-discharge, Flooding, Water resources, Weather Forecast

## 1 Introduction

In Japan, the basic policies for strengthening the flood control functions of existing dams and the formulation of basin-wide flood management plans have raised expectations for the use of water supply dams, agricultural dams, and irrigation ponds. However, if the assumed inflow cannot be secured, pre-release operations increase the risk to water utilization. In particular, for agricultural water facilities, such operations entail the danger of functional disruption, making it essential to evaluate the effectiveness and stability of flood damage reduction by irrigation ponds. Domestically and internationally, important knowledge has been accumulated from meteorological and flood management perspectives to avoid failure ratess of pre-release (e.g., [1], [2]). Nevertheless, because extreme rainfall events are rare and the actual implementation of pre-release has been limited, there have been no documented cases of failure ratess. Discussions on failure ratess have therefore been confined to a few cases or locations, highlighting the need for large-scale forecast-based evaluations to ensure statistically robust assessments. Given that heavy rainfall may occur even in locations with no prior experience of such events, the use of irrigation ponds in these areas will also be required. To enable pre-release regardless of rainfall experience, the accumulation of knowledge that assumes irrigation ponds with various specifications is crucial for flood control planning and land improvement projects. However, data on the hydrological quantities of irrigation ponds remain insufficient. To both reduce flood damage and avoid failure ratess in pre-release, it is necessary to compensate for this data scarcity and quantitatively evaluate the failure rates. This study aims to examine the tendencies of failure ratess in pre-release operations of irrigation ponds according to catchment area and irrigated area. Based on long-term, large-scale meteorological forecast data, water balance simulations were performed to estimate failure ratess.

## 2 Materials and methods

To generate forecast data, we used the Database for Policy Decision Making for Future Climate Change (d4PDF). In this study, we extracted precipitation from the 6-hourly mean two-dimensional data in the d4PDF historical experiment, as well as six atmospheric variables from the 6-hourly instantaneous three-dimensional atmospheric data: air temperature, specific humidity, geopotential height, cloud water content, meridional wind, and zonal wind. Data were obtained for 11 years (2000–2010) from five ensemble members (Member 1 to Member 5), with a temporal resolution of 6 hours. These data were used both as training datasets for constructing machine learning models and as application datasets for producing forecast values.

As a machine learning model, we employed the Support Vector Machine (SVM). The input variables at each time step and grid cell included precipitation, air temperature, specific humidity, geopotential height, cloud water content, meridional wind, and zonal wind at time steps $t–3$, $t–2$, $t–1$, and $t$. Among these, six meteorological variables were derived from the three-dimensional atmospheric data, consisting of 12 vertical layers per grid cell. While using six variables across 12 layers as features allowed for a faithful representation of grid-specific characteristics, the large number of variables also posed the risk of slower model training. Therefore, we standardized the full dataset for each grid cell to unify the variable scales, and created the input values accordingly. The target variables were the standardized values of all meteorological variables at $t+1$ for each grid cell. It should be noted that the objective of this study was not to construct a highly accurate forecasting model, but rather to use large-scale forecast data for water balance simulations and to quantify the failure rates of pre-release operations.

According to the pre-release guidelines, pre-release is implemented if the cumulative rainfall over 3–4 days is

predicted to exceed a threshold rainfall. First, using th e machine learning models developed for each grid cel l, the meteorological variables at *t+1* were predicted ba sed on input variables at *t–3, t–2, t–1,* and *t*. Next, *t– 2, t–1, t,* and the predicted *t+1* were used to forecast t he meteorological variables at *t+2*. By recursively feedi ng predictions into the trained models, meteorological v ariables at *t+1* through *t+16* were obtained at any give n time *t*. Given the temporal resolution of 6 hours, thi s corresponds to forecasts from 6 hours ahead up to 9 6 hours ahead. The small root mean square error (RM SE) confirmed that the forecasts were functional for ou r purposes. Forecasts for 55 years were concatenated ac ross all grid cells, yielding a synthetic dataset equivale nt to 1,100 years. Fig.1 showed that predicted value w hich is forecasted by the machine learning model and s tored value which is stored in d4PDF.

Following the pre-release guidelines, decisions to initia te or suspend pre-release operations were made. Since no observational data on water levels or catchment area s were available, the threshold rainfall was set at 100 mm for estimating the failure rates. To evaluate the ma ximum potential flood mitigation effect, the initial reser voir storage of the hypothetical reservoir was set to zer o. From the timing of pre-release initiation to the end of the rainfall event, the inflow volume into the reserv oir was calculated. Assuming that the forecast rainfall f ell uniformly across the defined catchment area, the irri gation area and catchment area of the hypothetical rese rvoir were parameterized and subjected to both forecast ed and observed rainfall inputs. For the periods of pud dling and heading, the required water demand per unit area was set at 200 mm. The required water to avoid yield loss, $W_{red}$, was calculated using Equation (1):

$$W_{red} = (W_{evap} + W_{soil}) \times 9 \qquad (1)$$

where $W_{evap}$[mm] represents the maximum evapotranspir ation used in agricultural water planning (approximately 8 mm/day), and $W_{soil}$[mm] represents the maximum so il infiltration given by the Ministry of Agriculture, Fore stry and Fisheries (approximately 86 mm/day). The fail ure rates was defined as the proportion of events in w hich the available storage capacity at the end of a rele ase was insufficient, relative to the total number of pre -release operations. We assumed that all irrigation areas assigned to each reservoir were to be covered, thereby providing a conservative (safety-oriented) evaluation fo r agricultural water use.

## 3 Results and discussion

For a threshold rainfall of 100 mm, the number of pr e-release operations was 463 over the 1,100-year datase t. Fig.2 presents a heatmap of the failure rates as a fu nction of irrigated area and catchment area. In most re gions, the failure rates reached 100%. In contrast, the minimum failure rates for the 100 mm threshold was 7 9.3%.

Pre-release of the entire reservoir volume initiated thre e days in advance exhibited consistently high failure ra tess. Nevertheless, for certain irrigation areas, a decreas ing trend in the failure rates was observed as catchmen t area increased. Specifically, when the irrigated area w as 1 ha, a reduction in failure rates was evident once t

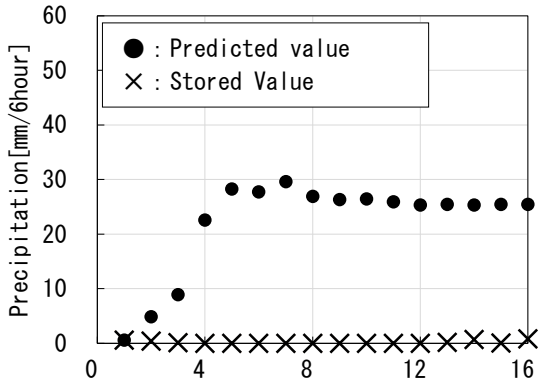


Fig.1 Predicted value and Stored value

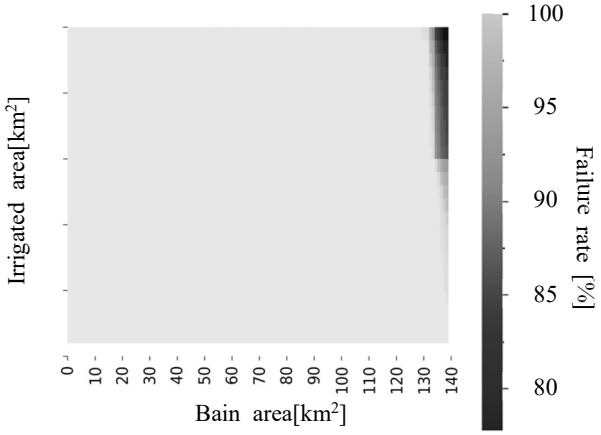


Fig.2 Failure rate of pre-release

he catchment area exceeded 4 × $10^{-2}$ km². Similarly, f or an irrigated area of 10 ha, a decline in failure rates was observed when the catchment area exceeded 5 km².

## 4 Conclusions

This study aimed to examine the tendencies of failure ratess in pre-release operations of irrigation ponds with respect to catchment area and irrigated area. It will be necessary to evaluate pre-release operations by consideri ng both the benefits of flood damage reduction, as de monstrated in previous studies, and the potential econo mic losses to rice production caused by failure ratess.

## Reference

[1] Kitani et al.: Verification of early decision to start preliminary release of reservoir and recovery potential using long-term ensemble rainfall forecast, vol.29, pp.497-502, 2023.

[2] Fujita et al. : Applicability of JMA MSM and GSM for pre-release at multi-purpose dams in Japan, Journal of Japan Society of Civil Engineers, Ser. B1 (Hydraulic Engineering), Vol.77, Issue 2, pp.I_85-I_90, 2021.

[3]Ikemoto et al.: Evaluation of an Adaptation Strategy for Flood Damage Mitigation Under Climate Change Through the Use of Irrigation Reservoirs in Japan. Water Resour Manage, Vol.37, pp.4159–4175 2023.

# Skiing in a Changing Climate: A CONUS404 Analysis of Historical Snowfall Trends for U.S. Skiing

○ Hiroto BAUER[1*] & Yusuke HIRAGA[1]
[1] Department of Civil and Environmental Engineering, Tohoku University, Miyagi 980-8579, Japan.
*hiroto.bauer.p2@dc.tohoku.ac.jp.

## Abstract

Climate change threatens the U.S. ski industry by reducing snow reliability. This study uses the CONUS404 reanalysis dataset to quantify historical trends in snowpack and ski season length from 1980 to 2022. We first validated CONUS404's snow water equivalent (SWE) and snow depth against the SNODAS dataset. We then applied the Mann-Kendall test to identify trends in SWE, snow depth, and the number of skiable days, defined as days with >30 cm snow depth. Validation revealed a strong agreement (Pearson R=0.7), with CONUS404 underestimating snowpack relative to SNODAS (RMSE: 20.4 mm SWE, 55.3 mm depth), yet confirming its suitability for trend analysis. Our examination identified significant decreasing trends in SWE, snow depth, and skiable days across much of the U.S., especially in western regions, where declines reached up to -2.1 skiable days per year. Conversely, some locations in the Northeast showed an increasing trend. These findings quantify the vulnerability of the U.S. ski industry to a warming climate and underscore the need for adaptation strategies to ensure resilience.

**Keywords:** Climate Change; Ski Industry; Historical Snowfall; Reanalysis; SWE; Snow Depth.

## 1 Introduction

In the context of a warming climate, snow's acute sensitivity to temperature changes renders the monitoring of related variables essential for assessing broader climate impacts. In addition, the susceptibility of the ski industry to variable snowfall and climate change [1] puts the industry at major risk. In the past, research has been constrained by reliance on point data from monitoring stations. This has limited analysis to specific resorts or regions. However, with the newest reanalysis tools available today, it is now possible to investigate historical data for trends in snow and ski season length across wide regions. This study will focus on CONUS404 which covers the contiguous United States at a 4 Km resolution from October 1979 to September 2021 [2]. However, as a recently developed dataset, its snow-related variables remain largely unvalidated against independent observations. As such, we aim to conduct an independent evaluation of SWE and snow depth from CONUS404 against the more established Snow Data Assimilation System (SNODAS) from the National Snow and Ice Data Center [3]. SNODAS is a modeling and data assimilation framework that estimates snow cover across the United States.

Previous research regarding trends in snowfall and ski viability has shown widespread negative impacts on the ski industry around the world with less snowfall, a shorter ski season, and more variable snowfall [1], [4], [5]. However, these studies are limited to specific regions or established ski resorts while there are currently no analyses that examines historical trends in snow over the entire contiguous United States. Furthermore, most studies related to climate change impacts on skiing focus on current ski resort locations while overlooking snow conditions in undeveloped or backcountry areas that also support recreation and may hold future potential for ski development.

Accordingly, this study has two primary objectives. First, to conduct a comprehensive validation of the CONUS404 snow depth and SWE variables across the contiguous United States. Second, apply the validated dataset to a continental-scale trend analysis of historical snowfall and ski viability, covering established resort areas, backcountry terrain, and other understudied regions.

## 2 Materials and methods

CONUS404 is reanalysis dataset created by downscaling fifth-generation European Centre for Medium-Range Weather Forecasts (ECMWF) atmospheric reanalysis of the global climate dataset (ERA5) [6] with the Weather Research and Forecasting (WRF) model [7].

To validate CONUS404, Snow Water Equivalent (SWE) and snow depth data were compared against the SNODAS dataset for the overlapping period of 2003-2022. SNODAS is a modeling and data assimilation framework that estimates snow cover across the United States. SNODAS can be broken down into two major processes: first, the snow cover and related variables such as SWE and snow depth are modeled. Then SNODAS integrates the modeled data with satellite, airborne and ground data to provide a more accurate estimate of snow related variables [3].

We evaluated the temporal mean and 99th percentile values using RMSE and Pearson correlation, upscaling SNODAS to a 4-km grid for direct spatial comparisons.

Following validation, we analyzed historical trends using the full 1979-2022 CONUS404 time period. The Mann-Kendall test with Sen's slope was applied to annual SWE and snow depth data to identify significant trends ($p \leq 0.05$) across the contiguous U.S.

To assess direct impacts on skiing, we analyzed trends in ski season length from 1979-2022. This was quantified using two metrics: the maximum number of skiable days and the longest continuous skiable period. A "skiable day" was defined as having ≥30 cm of snow depth. The Mann-Kendall test with Sen's slope was applied to both metrics to examine spatial trends. For all trend analyses, results were interpolated to 499 U.S. ski resort locations to inspect trends at resorts.

## 3 Results and discussion

Validation of CONUS404 against SNODAS indicates a strong agreement, with RMSE values of 20.4 mm for SWE and 55.3 mm for snow depth. A spatial plot of the difference in CONUS404 SWE and SNODAS SWE can be seen in Fig. 1. CONUS404 exhibits a negative bias, with the largest discrepancies occurring in the mountainous regions of the western United States. 99th percentile results showed a similar pattern to time averaged results. Pearson Correlation coefficient of 0.7 for both variables further supports this relationship, confirming that CONUS404 adequately represents snow conditions for the subsequent trend analysis.

The largest discrepancies in mountain regions are likely due to the model's coarse spatial resolution, which is insufficient to accurately capture the complex topography and orographic processes that occur in these areas [8].

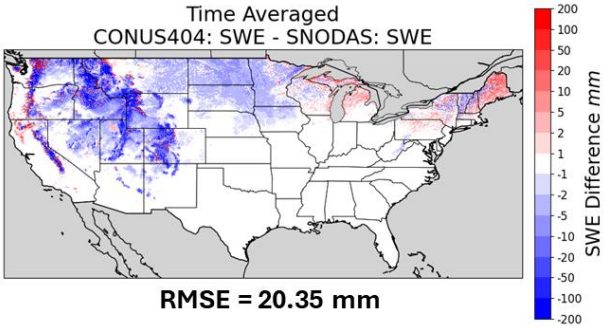


**Fig. 1: Spatial difference between time averaged CONUS404 and SNODAS SWE.**

Trend analysis of CONUS404 revealed a decreasing trend for snow depth and SWE across much of the contiguous United States. Increasing trends were seen in the northern United States and in lee of the Sierra Nevada Mountains. The maximum decreasing trend was -6.5 mm SWE per year, and the largest increasing trend was 1.7 mm SWE per year. All ski resort locations with statistically significant trends (>95%) exhibited a decreasing trend for SWE and all but one resort showed a decreasing trend for snow depth (Fig. 2).

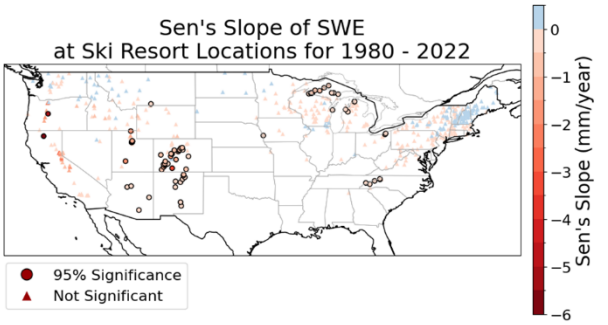


**Fig. 2: Sen's slope of CONUS404 SWE interpolated at ski resort locations. Outlined circular points represent greater than 95% significance in Sen's slope.**

Ski season duration analysis yielded decreasing ski season length for the majority of the United States. The maximum number of skiable days showed sporadic results with mostly decreasing trends across much of the U.S. with some increasing trends in Montana and Maine. The longest continuous skiable period showed a more clustered response with most of the U.S. showing no trend while mountainous regions in the west show largely decreasing trends and Main showing an increasing trend. Maximum increase is 1.2 consecutive days per year while maximum decrease is -2.5 consecutive days per year. At ski resort locations, all significant trends for continuous skiable days showed a decreasing trend. For maximum skiable days, all ski resorts in the west and Midwest showed a decrease while five resorts in the Northeast showed an increasing trend.

Results indicate that ski resorts are facing declining snowpack and shorter snow seasons. To mitigate these impacts, the industry has widely adopted snowmaking, which can offset some losses in natural snowfall. However, this strategy is resource-intensive, requiring significant water and energy, and its benefits are limited to on-piste terrain. Thus, the reduction in snow across the U.S. poses a major risk for increasing operational costs and reduced ski visitations at ski resorts. Backcountry skiing is put at even greater risk due to complete reliance on natural snow.

## 4 Conclusions

Validation of CONUS404 SWE and snow depth produced adequate results with good Pearson Correlation making the dataset viable for the subsequent trend analysis. The analysis identified a broad decline in snow depth and SWE across most of the United States. Skiable days analysis revealed a widespread decrease in both continuous and maximum skiable days across the United States, with especially impactful decrease at popular ski areas in the western mountainous regions of the United States.

## References

[1] B. Abegg, S. Agrawala, F. Crick, and A. de Montfalcon, Eds., *Climate change in the European Alps: adapting winter tourism and natural hazards management*. Paris: Organisation for Economic Co-operation and Development, 2007.

[2] R. Rasmussen *et al.*, "Four-kilometer long-term regional hydroclimate reanalysis over the conterminous United States (CONUS)." UCAR/NCAR - Research Data Archive, Jan. 10, 2023. doi: 10.5065/ZYY0-Y036.

[3] A. P. Barrett, "National Operational Hydrologic Remote Sensing Center SNOw Data Assimilation System (SNODAS) Products at NSIDC," Nov. 2003.

[4] D. Scott, G. McBoyle, and A. Minogue, "Climate change and Quebec's ski industry," *Global Environmental Change*, vol. 17, no. 2, pp. 181–190, May 2007, doi: 10.1016/j.gloenvcha.2006.05.004.

[5] R. Steiger, D. Scott, B. Abegg, M. Pons, and C. Aall, "A critical review of climate change risk for ski tourism," *Current Issues in Tourism*, vol. 22, no. 11, pp. 1343–1379, July 2019, doi: 10.1080/13683500.2017.1410110.

[6] H. Hersbach *et al.*, "The ERA5 global reanalysis," *Quarterly Journal of the Royal Meteorological Society*, vol. 146, no. 730, pp. 1999–2049, 2020, doi: 10.1002/qj.3803.

[7] W. C. Skamarock *et al.*, "A Description of the Advanced Research WRF Version 3," vol. 27, pp. 3–27, Jan. 2008.

[8] S. Sabetghadam, C. G. Fletcher, and A. Erler, "The importance of model horizontal resolution for improved estimation of snow water equivalent in a mountainous region of western Canada," *Hydrology and Earth System Sciences*, vol. 29, no. 4, pp. 887–902, Feb. 2025, doi: 10.5194/hess-29-887-2025.

# Physical Understanding of Parameters in a Large Woody Debris Discharge Model

Yunhao Liu[1*], Daisuke Komori[1,2], Sartsin Phakdimek[3] & Yuta Abe[1]
[1]Graduate School of Environmental Studies, Tohoku University, Miyagi 980-8572, Japan.
[2]Green Goals Initiative, Tohoku University, Miyagi 980-8572, Japan.
[3]School of Geotechnology, Institute of Engineering, Suranaree University of Technology, Nakhon Ratchasima 30000, Thailand.
[*]E-mail: liu.yunhao.r6@dc.tohoku.ac.jp.

## Abstract
This study advances a physical interpretation of parameters in a large woody debris (LWD) discharge model whose transport–storage component relies on a lumped storage-function framework, making parameter determination dependent on observation-rich basins and limiting applicability. We analyze 30 Japanese dam watersheds to build linear linkages between model parameters (*Z, b, k, p*) and measurable watershed characteristics via Principal Component Regression, thereby reducing reliance on LWD observations. The analysis highlights rainfall return levels and steep-area metrics as dominant controls on *Z* and *b*, and river density and topographic/forest proportions as key controls on k and p, respectively. As an undammed application, we estimate parameters for the Gofukuya River (Marumori, Miyagi) and, after reducing an overestimated storage-capacity parameter *Z*, reproduce the 2019 typhoon LWD peak (simulated 1,486 m³ vs. reported 1,710 m³), illustrating both the promise and the scale-sensitivity of the approach. These results support parameter predictability from physical descriptors, enabling deployment to data-scarce mountainous basins.
**Keywords:** Large Woody Debris; Storage-Function Model; Physical Parameterization

## 1 Introduction
Large woody debris (LWD) affects ecosystems and flood risk (Gurnell et al., 1995). While it provides habitat and aids nutrient cycling, extreme events can mobilize volumes that block channels and damage infrastructure. In recent decades, increasing monsoon rainfall has intensified landslide hazards (Chaithong et al., 2017). A previous study described LWD discharge by coupling rainfall-triggered shallow-landslide recruitment with a lumped double storage-function model for entrainment (Komori et al., 2022). As a statistical model, Storage-function parameters (*Z, b, k, p*) are inferred from observed LWD, which limits their applicability to data-scarce areas. Therefore, this study attempts to link model parameters to watershed physical characteristics through Principal Component Regression, using data from 30 Japanese dam watersheds. Applicability was tested in the undammed Gofukuya watershed in Marumori Town, Miyagi Prefecture (24.17 km², 22.45 km river length), by predicting model parameters from watershed descriptors and evaluating performance during the 2019 extreme event. This study aims to reduce dependence on LWD observations while retaining interpretability of storage and transport.

## 2 Materials and methods
Following Komori et al. (2022), this study adopts a double storage-function LWD model whose parameters *Z, b, k*, and *p* present annual discharge dynamics. Simulation was implemented in Fortran (NGA Fortran Builder 7.0), and the model's accuracy was evaluated with NSE, with NSE > 0.4 treated as acceptable.

30 dam watersheds that were successfully reproduced by the double-tank model (Abe et al., 2024) as the base sample for the regression analysis. The model's structural framework is Fig. 1.

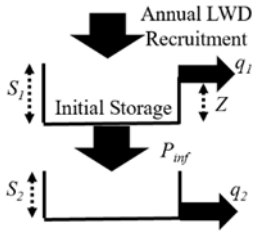


**Figure 1. Conceptual framework of the Storage-function model**

Where $S_1$ and $S_2$ are storage volumes in the first and second tanks (m³), respectively. $Z$ is the capacity of the first tank, which is one of the model parameters determined by the NSE method. The sum of $q_1$ and $q_2$ is the annual LWD discharge volume (m³). The governing equations and parameter definitions are presented below.

$$q_1 = S_1(n) - Z \quad (S_1(n) \geq Z)$$
$$q_1(n) = 0 \quad (S_1(n) < Z)$$
$$P_{inf} = b \cdot S_1(n)$$
$$S_1(n+1) = S_1(n) + P - P_{inf}(n)$$

Where $b$ is a parameter and $n$ is time (in years).

$$\frac{dS_2}{dt} = P_{inf} - q_2(n)$$
$$S_2 = k \cdot q_2^p$$

Where $k$ and $p$ are parameters. All parameters and the simulated volume ($q_{sim} = q_1 + q_2$) were determined by the NSE method.

To relate (*Z, b, k, p*) to watershed physical characteristics (including precipitation return levels, Area of watershed, Forest Cover, etc.), this study standardized predictors (while Mean = 0, Standard Deviation = 1), computed Pearson correlations, and retained features with $|r| \geq 0.3$ prior to PCR, a method which correlated predictors onto a few orthogonal principal components that capture most variance, then

regresses the response on these components. Jackknife resampling was used to further evaluate the linear equation's predictive accuracy. The framework of this study was shown in Fig. 2.

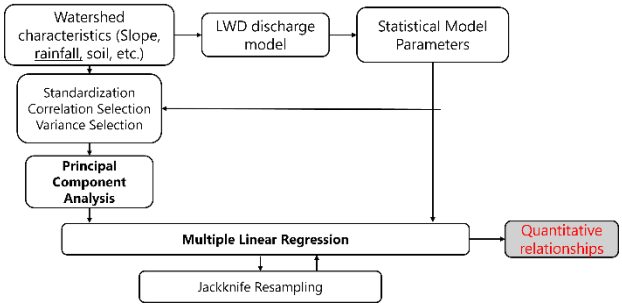


**Fig. 2. Conceptual framework of parameterization**

## 3 Results and discussion

After the principal component regression analysis, the watershed physical characteristics with the strongest influence on the four model parameters are presented in Table 1.

**Table 1 Summary of the most contributing variables**

| Parameters | Physical characteristics |
|---|---|
| Z | Precipitation return levels, Steep Area |
| b | Steep Area |
| k | River density |
| p | Percentage of Steep area and forest cover |

In summary, steep area is the dominant watershed attribute influencing most parameters, especially *Z* and *b*, while precipitation return levels primarily affect Z, river density affects *k*, and forest cover contributes jointly with steep terrain to *p*. The accuracy of the principal component regression analysis is presented in Table 2.

**Table 2 Summarization of regression result**

| Parameters | $R^2$ | Mear $R^2$ | Standard error of $R^2$ |
|---|---|---|---|
| Z | 0.9301 | 0.9639 | 0.0236 |
| b | 0.5689 | 0.6791 | 0.1522 |
| k | 0.5416 | 0.6871 | 0.1452 |
| p | 0.2357 | 0.3676 | 0.1233 |

The regression results demonstrate that parameter Z can be reliably explained by watershed characteristics ($R^2$ = 0.93, mean $R^2$ = 0.96), indicating strong model stability and explanatory power. In contrast, b and k exhibit only moderate explanatory performance ($R^2 \approx 0.54$–$0.57$), suggesting that additional controlling factors beyond the selected physical indicators may be involved. Parameter p shows very low explanatory power ($R^2$ = 0.24), implying that the current watershed descriptors cannot sufficiently capture its variability and may require either finer-scale predictors or a different model structure.

As a further step, this study selected one dam from the source sample set (Obe Dam in Shimane Prefecture) as a validation case. Using the parameters estimated through the regression analysis, the model produced an LWD discharge of 2,889 m³, compared with the recorded value of 2,040 m³. Although the difference amounts to several hundred cubic meters, the result demonstrates that the regression-based approach is feasible, while indicating that the remaining error requires further examination.

However, when the regression equation derived from PCR was applied to the Gofukuya basin, the predicted value of parameter Z reached 8,698 m³, which is unrealistically high for a watershed of only 24.17 km². In combination with the remaining three parameters, this resulted in a failure to reproduce the observed 2019 peak discharge (1,710 m³). To further explore the applicability of this approach, Z was manually reduced to 500 m³ while retaining the other estimated parameters in the storage function model. Under this adjustment, the simulated peak in 2019 reached 1,486 m³ (Figure 4), which is much closer to the observed value.

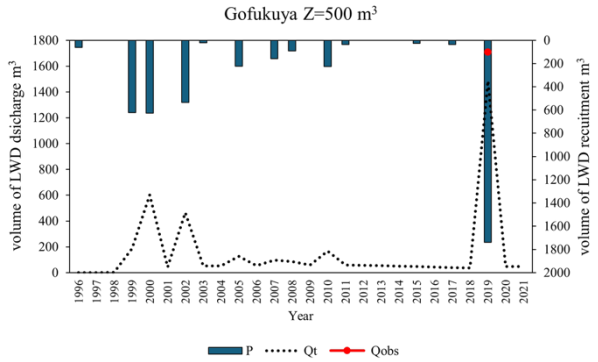


**Fig. 3. Simulation result using parameters from principal component regression**

Where $P$ is annual LWD recruitment volume(m³), $Q_t$ is simulation discharge volume(m³), and $Q_{obs}$ is observed volume(m³). This result suggests that the current regression relationship for Z is not scalable to small basins. The average *Z* in the calibration samples exceeds 10,000 m³, which causes systematic overestimation when extrapolated to catchments with substantially smaller drainage areas. Therefore, expanding the sample set, particularly by including more small watersheds or developing an alternative regression framework, will be a necessary direction for future work.

## 4 Conclusions

This study advances a physical interpretation of parameters in a double storage-function model for LWD export. Using 30 dam watersheds reproduced with acceptable NSE, principal component regression links parameters to measurable watershed attributes. Although the approach was successfully validated at Obe Dam within the source sample set, applying the regression-derived relationship to an out-of-sample site, a small undammed basin (Gofukuya), resulted in an unrealistically high predicted Z and consequently an underestimation of LWD. The simulation results, after adjusting Z to align more closely with observations, revealed the effects of watershed area scale. These findings indicate that area-dependent scaling, nonlinear formulations, and expanded small-basin samples are needed for enhancement of the model's applicability. Overall, the approach reduces reliance on LWD observations and is promising for data-scarce mountainous regions, although Z's applicability remains a key limitation.

## Reference

[1] Komori, D., Sukegawa, Y., Chaithong, T., & Kazama, S. (2022). Modelling of large wood export at a watershed scale. Earth Surface Processes and Landforms, 47(2), 688-696.

# Assessing Climate Change Impacts on Extreme Precipitation using Large-Ensemble Data and Stochastic Storm Transposition: A Case Study for the Arakawa Watershed, Japan

○ Wasitha DILSHAN[1*], Yusuke HIRAGA[1], Daniel B. WRIGHT[2] & Jose Angelo HOKSON[1]
[1]Department of Environmental Engineering, Environmental University, Miyagi 980-8579, Japan.
[2] Department of Civil and Environmental Engineering, University of Wisconsin-Madison, USA.
[*]E-mail: c4td9605@dc.tohoku.ac.jp.

## Abstract

The Probable Maximum Precipitation (PMP) is a critical benchmark for designing hydraulic structures against extreme floods, yet traditional estimation methods often fail to account for climate non-stationarity. This study aims to quantify the impact of climate change on extreme 24-hour rainfall in the Arakawa watershed, Japan, by integrating Stochastic Storm Transposition (SST) with the d4PDF large-ensemble climate dataset. Results indicate a clear intensification of extremes under warming; for instance, at a 10,000-year return period (AEP=$10^{-4}$), precipitation depth increased from 311.74 mm (historical) to 394.41 mm (+4K). The sensitivity, measured as percent increase per Kelvin, varied with event rarity, peaking at 7.3% $K^{-1}$ for very rare events, aligning with Clausius-Clapeyron scaling in some cases. These findings demonstrate that SST provides a robust framework for deriving non-stationary precipitation frequency estimates, which are essential for updating engineering design standards and enhancing climate resilience in flood risk management. Future work will expand this analysis by incorporating multiple ensemble members to better characterize uncertainty.

**Keywords:** Probable Maximum Precipitation; Stochastic Storm Transposition; d4PDF; Climate Change.

## 1 Introduction

The Probable Maximum Precipitation (PMP), which is defined as the greatest depth of precipitation for a specified duration that is meteorologically possible over a particular area at a given time, is widely applied as a design standard for estimating the Probable Maximum Flood (PMF) in hydrological engineering. Accurate estimation of PMP is therefore crucial for the safe design and risk assessment of hydraulic structures, as it supports the evaluation of maximum flood scenarios and helps prevent possible infrastructure failures. Traditional methods often rely on stationary climate assumptions and are limited by the short length of historical records [1].

To address this, advanced techniques like Stochastic Storm Transposition (SST) have been developed, which synthetically expand the record of extreme events by spatially transposing observed storms within a region, thereby providing more robust frequency analyses [2,3]. Concurrently, large-ensemble climate datasets like d4PDF have emerged as powerful tools for characterizing internal climate variability and projecting future hydrometeorological extremes, with recent studies applying them to assess climate change impacts on PMP [4].

However, no study to date has deterministically integrated the SST framework with large-ensemble climate data, as previous studies often used a single storm event for transposition. In contrast, SST employs multiple extreme storms within rainfall-homogeneous regions, enabling a more robust and comprehensive assessment of precipitation extremes.

Therefore, this study aims to apply Stochastic Storm Transposition using the d4PDF large-ensemble dataset to assess the sensitivity of extreme precipitation frequencies in the Arakawa watershed to global warming. By comparing historical, +2K, and +4K warming scenarios, this study aims to quantify the change in precipitation depth per degree of warming for multiple durations and return periods, providing a statistically robust, scenario-based perspective on future flood risks.

## 2 Materials and methods

### 2.1 Study Area & Data

This study utilized the first ensemble member of the d4PDF dataset, which provides high-resolution (5 km) hourly precipitation data under historical climate conditions for the 60-year period from 1950 to 2011.

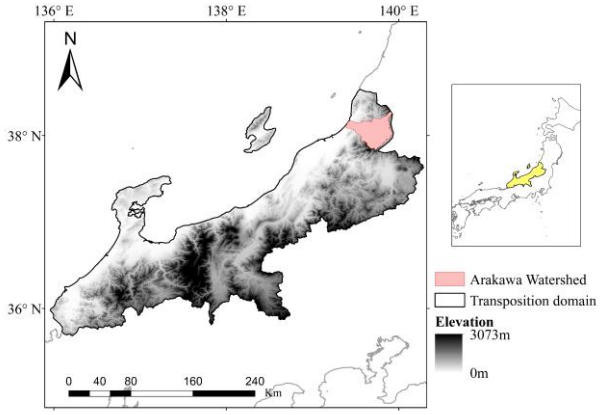


**Fig. 1. Study area and storm transposition domain.**

The future climate simulations cover 60 years each, spanning 2030–2090 for the +2 K scenario and 2050–2110 for the +4 K scenario. The Arakawa watershed, covering approximately 1,150 km² in the Hokuriku region, is a nationally designated Class-A River system in Japan. The area receives intense rainfall averaging about 2,210 mm annually, with major flood risks during the Baiu rainy season, typhoons, and autumn precipitation. Key infrastructure such as the Iwafune Dam and Takanosu sediment control dam was

constructed following the devastating 1967 floods but has yet to be updated for projected future climate conditions. The Hokuriku region (≈40,620 km²), classified by MLIT (2015) as one of Japan's 15 rainfall-homogeneous regions, was selected as the storm transposition domain, meeting SST's key requirement of rainfall homogeneity [3].

### 2.2 SST and climate-driven Rainfall Frequency Analysis

SST pools observed extreme rainfall events from the entire transposition domain and repositions them spatially and temporally to the target watershed, generating a long, synthetic record of extreme rainfall possibilities. This SST process was applied to both historical and future warming scenarios from the d4PDF dataset. Subsequently, Rainfall Frequency Analysis (RFA) was conducted on this expanded data to estimate precipitation depths for Annual Exceedance Probabilities (AEPs) such as $10^{-3}$, $10^{-4}$. Finally, the resulting changes in precipitation intensity between historical and future climates were quantified as a percentage increase per Kelvin, enabling a direct comparison with thermodynamic scaling rates like the Clausius-Clapeyron relationship.

## 3 Results and discussion

The RFA results for the 24-hour accumulation period reveals a distinct increase in precipitation depths across warming scenarios (Fig.2). At an annual exceedance probability (AEP) of $10^{-4}$, the ensemble median precipitation depths show a clear trend: 311.74 mm for the Historical data (HPB), increasing to 335.36 mm under +2K warming, and further rising to 394.41 mm under +4K warming. The range presented reflects the ensemble variability inherent in the stochastic generation of synthetic storm events. This progressive intensification aligns with physical expectations that warmer climates enhance atmospheric moisture capacity, resulting in more intense extreme rainfall.

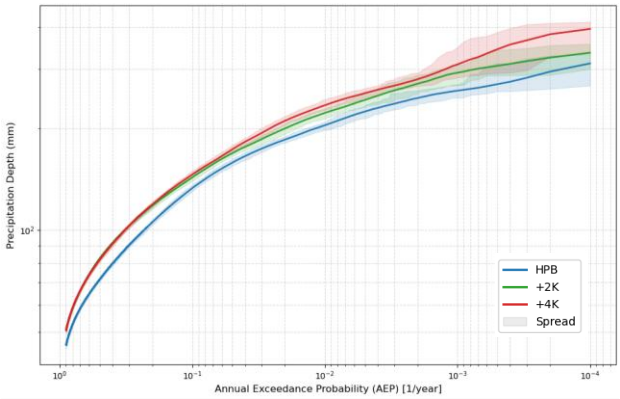


**Fig. 2. RFA for historical, +2K and +4K scenarios.**

The % difference in precipitation depth per-K, relative to the HPB, indicates higher sensitivity at rare events (Fig.3). For example, at an AEP of $10^{-3}$, the increase per -K is 6.5% under +2K and 4.9% under +4K scenarios. The incremental rise varies with return period, suggesting nonlinearity in temperature-precipitation scaling for extreme events. The slightly lower per-K amplification under +4K compared to +2K for some AEPs may reflect competing factors such as changes in large-scale atmospheric dynamics or moisture availability limits under extreme warming conditions.

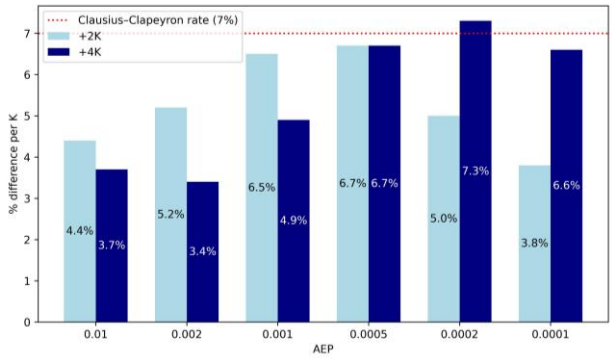


**Fig. 3. Relative Increase in Precipitation per Kelvin**

Interestingly, the greatest per-K value of 7.3% occurs at an AEP of $2\times10^{-4}$ in the +4K scenario, indicating amplified changes in rare, high-impact rainfall events. These findings illustrate that the SST-based framework can capture the complex interplay between climate warming and precipitation extremes, yielding physically consistent and statistically robust frequency estimates.

Comparison with theoretical climate warming rates, such as Clausius-Clapeyron scaling (7% per-K), highlights reasonable agreement, particularly for the rarest events. This conformity highlights the potential of SST combined with large-ensemble data to inform climate-resilient design standards by realistically encompassing warming-driven intensification across the full range of return periods.

## 4 Conclusions

This study applied the SST method to estimate extreme precipitation in the Arakawa watershed under historical and future warming scenarios. Results demonstrate clear increases in precipitation depth with rising temperatures, consistent with thermodynamic expectations. The SST framework, combined with large-ensemble d4PDF data, enables robust frequency analysis across a range of return periods, capturing spatial and temporal variability. However, the current approach used only one ensemble member, limiting depiction of full climate variability. Future work should utilize multiple ensemble members to better quantify uncertainty and enhance reliability. This integration of SST with full ensemble datasets will improve resilience assessments and inform climate-adaptive flood risk management.

## Reference

[1] NASEM, Modernizing probable maximum precipitation estimation, National Academies Press (2024).

[2]D. B. Wright, J. A. Smith, G. Villarini, M. L. Baeck, Estimating the frequency of extreme rainfall using weather radar and stochastic storm transposition, Journal of Hydrology, 488 (2013) 150–165.

[3]D. B. Wright, G. Yu, J. F. England, Six decades of rainfall and flood frequency analysis using stochastic storm transposition: Review, progress, and prospects, Journal of Hydrology, 585 (2020) 124816.

[4]Y. Hiraga, S. Watanabe, T. Yamashita, H. Takizawa, Climate Change Effects on Probable Maximum Precipitation (PMP) of Mesoscale Convective Systems: Model-based Estimation and Large Ensemble-based Frequency Analysis, Journal of Hydrology, 661 (2025) 133724

# Grain size and Riparian Vegetation Survey in a vegetated river

○ Tao YAMAMOTO[1*], Takaya KANEKO[1], Tomoaki MATSUURA[1], Takuya MATSUMOTO[1], Haruki TAMAKAWA[2], Shimon SUZUKI[1] & So KAZAMA[1]

[1]Department of Civil and Environmental Engineering, Tohoku University, Miyagi 980-8579, Japan.
[2]Department of Civil Engineering and Architecture, School of Engineering, Tohoku University, Miyagi 980-8579, Japan.
[*]E-mail: yamamoto.tao.t8@dc.tohoku.ac.jp

## Abstract

Riparian vegetation has expanded within the channel of the Sagae River, Japan, over the past several decades, altering the fluvial morphology and presenting new challenges for river management. To understand the interaction between vegetation growth and sediment dynamics, field surveys of riverbed grain size and riparian plant species were conducted at five sites in July 2025. The results showed that median grain size (D50) increased upstream, from 35.8 mm at the downstream site to 109 mm near the upper site. At cross-channel locations, finer sediments were found within vegetated areas, suggesting that vegetation traps fine materials during flood events. The dominant species observed were Salix spp., Phragmites japonica, Robinia pseudoacacia, and Amorpha fruticosa. Phragmites japonica colonized frequently disturbed zones near water edges, while Salix and Robinia established in higher and more stable areas, indicating successional processes supported by sediment deposition. The spread of introduced species such as Robinia pseudoacacia and Amorpha fruticosa may be related to slope protection works in the upstream basin. These findings highlight the role of vegetation in modifying sediment environments and promoting the encroachment of late-successional and invasive species in the Sagae River.

**Keywords:** riparian vegetation; grain size; sediment deposition; Sagae River; invasive species.

## 1 Introduction

Over the last 70 years, riparian vegetation has encroached and expanded the colonies in the channel of the Sagae River, Yamagata, Japan. Rapid changes to the riverine landscape can cause multiple issues in river management, including flood control and riparian biodiversity [1][2]. It is essential for river management to understand the reasons why riparian vegetation has expanded rapidly. The grain size of the riverbed material indicates fundamental information about the vegetation substrate. The species of the riparian vegetation show how riparian vegetation grows with succession. This study reports our field survey in the Sagae River and clarifies the interaction between vegetation and fluvial geomorphology in a vegetated gravel-bed river.

## 2 Methods

The Sagae River is situated in northeast Japan and is a tributary of the Mogami River. The catchment area is 478.4 km$^2$ and the main channel length is 55.7 km [3], forming an alluvial fan at its confluence with the Mogami River. The average annual precipitation is approximately 2,543 mm at Oisawa (upstream area) and 1,368 mm at Aterazawa (downstream area) respectively [4]. This is a temperate climate, but it also has a lot of snowfall in the winter season. The Sagae River is dammed approximately 25 km upstream from its confluence with the Mogami River for flood protection, hydroelectric power generation, agricultural water provision, and other services. Downstream of the Sagae Dam, the riverbed slope is approximately 0.68%. The land surface in this catchment is mainly covered by forest.

Surveys of riverbed material sizes and riparian vegetation species were conducted at multiple locations along the study reach in July 2025. Five sites in **Figure 1** were selected for the grain size analysis. St.1 (0 km from the confluence) is located at the waterfront near the confluence with the Mogami River, where the flow is relatively gentle. St.2 (0 km) is situated on an elevated, vegetated floodplain adjacent to St.1. St.3 (1.4 km) is located on the right-bank waterfront near the Mizonobe Bridge. St.4 (5.2 km) is positioned on the left-bank waterfront midway between the Sagaegawa Bridge and the Jionji Bridge. St.5 (6.5 km) is located on the left-bank waterfront near the Jionji Bridge, beside the 5th groundsill. At St.1 and St.2, bed material sizes were measured using the bulk sampling and sieving method. For particles larger than 53 mm, weights were estimated from the cube root of the product of the shortest, longest, and intermediate diameters, and grain-size distributions were expressed as passing percentages by weight. At St.3–St.5, where coarser sediments were observed, the line grid method was applied [5]. At each site, 101 particles were measured by the three diameters, the cube root of their product was calculated, and passing percentages were determined by count. At the same sites where riverbed material was surveyed, riparian vegetation species within the river channel were recorded. Species associated with characteristic riverbed morphologies were documented by walking along the cross sections.

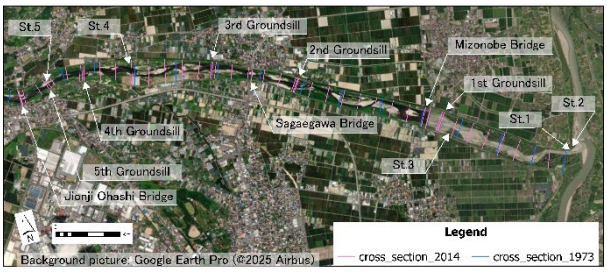


**Figure 1 Map of the survey sites**

## 3 Results and discussion

**Figure 2** shows the passing percentage of the grain size at every site. D50 at St.1 was 35.8 mm. The percentage of gravel (2 mm~75 mm) was approximately. 70 %. D50 at St.2 was 5.33 mm. The percentage of sand (0.075 mm~2 mm) was approximately. 37 %, and the other was gravel. D50 at St.3 was 51.9 mm. D50 at St.4 was 109 mm. D50 at St.3 was 69.6 mm. The longitudinal distribution of bed material grain size can be seen from a comparison of St.1, St.3, St.4, and St.5, and is basically composed of gravel and boulders, with grain size increasing the further upstream. On the other hand, as seen in the comparison of St.1 and St.2, there is a significant change in grain size across the river, which is thought to be influenced by the frequency of flooding due to differences in bed elevation.

In the riparian vegetation survey, Salix spp., Phragmites japonica, Robinia pseudoacacia, and Amorpha fruticosa were the dominant species (**Figure 3**). The grain size at St.2 was smaller than that at St.1, which could come from the vegetation function to capture fine sediment because St.2 was surrounded by the colony of Phragmites japonica. Phragmites japonica was observed along the water edges. They prefer a frequently disturbed area compared with other riparian species [1]. The water edges are exposed to high water flow, and their substrates are exchanged, creating new bare land that is suitable for pioneer plants.

In the same or higher elevation sites, Salix spp. created their colonies. Salicaceae also prefers bare land and water availability [6]. Behind the Salicaceae and Phragmites japonica, Pseudoacacia was established. Pseudoacacia prefers bare land and fine sediment. Phragmites and Salix trees deposited fine sediments and provided Pseudoacacia with a suitable environment. Amorpha fruticosa was seen close to the saplings of Pseudoacacia, but there was no mature population.

Pseudoacacia and Amorpha fruticosa were introduced in 1873 and 1912, respectively, to be planted as slope protection (Sabo work) [7][8]. The seeds of these species can be spread by water flow. The upstream of the Sagae River is a target of the national Sabo work. Thus, this Sabo work can cause the encroachment of these species.

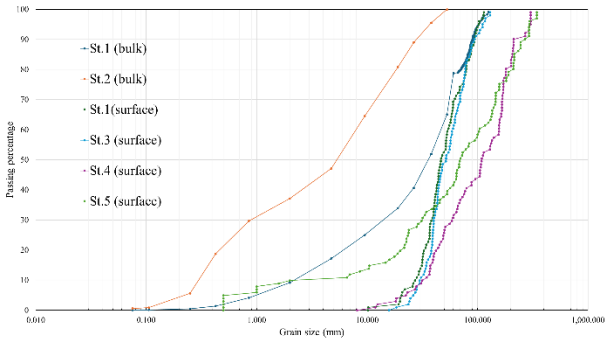


**Figure 2 Grain size distribution**

## Conclusions

We observed that vegetation caught the fine sediment, and the deposited sediment provided the late successional vegetation, such as Pseudoacacia, to establish. Some invasive plants have encroached upon the Sagae River; therefore, more attention should be paid to the tendency of these species.

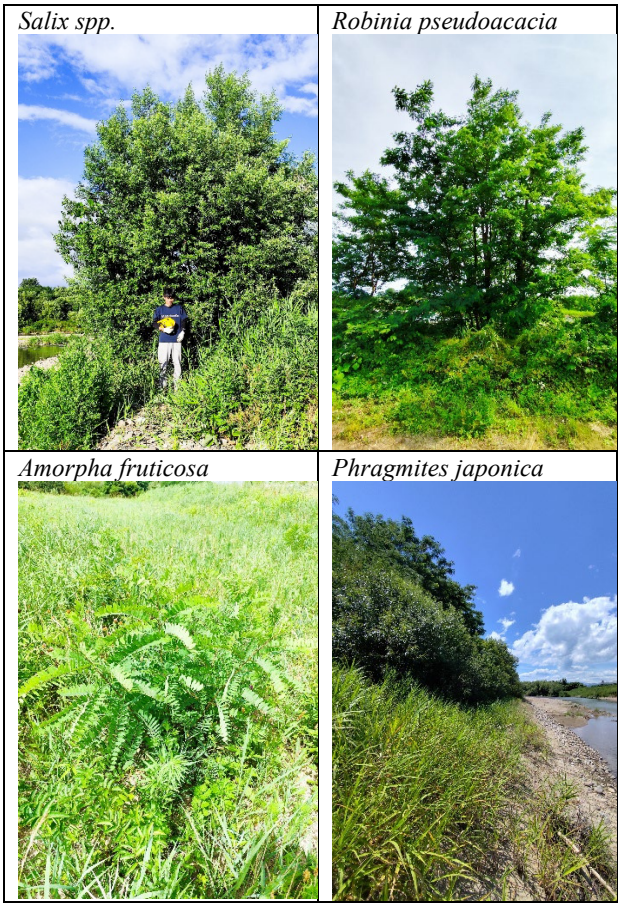


**Figure 3 The dominant species of the riparian vegetation in the Sagae River**

## Reference

[1] Asaeda, T., Gomes, P. I. A., & Takeda, E. River Research and Applications, 26(8), (2010) 960–976.

[2] Asaeda, T., García de Jalón, D., O'Hare, M., & Rahman, M. International Journal of River Basin Management. (2023).

[3] Ministry of Land, Infrastructure, Transport and Tourism, (2025) https://www.thr.mlit.go.jp/mogami/sagae-info/vision_sagae/01rinen/gaiyo.html

[4] Japan Meteorological Agency, 2025. Meteorological data, https://www.data.jma.go.jp/stats/etrn/

[5] Hakoishi, N., Fukushima, M., & Sakurai, T. 土木技術資料 53-11(2011)

[6] Nakamura, F., Ecology and Civil Engineering, Volume 2, Issue 2, (1999), Pages 125-139.

[7] Hioki, Y., Iwanaga, F., & Yamamoto, F. Journal of the Japanese Society of Revegetation Technology, Volume 40, Issue 3 (2014) Pages 472-478

[8] Sakio, H., Journal of the Japanese Society of Revegetation Technology, Volume 40, Issue 3 (2014) Pages 465-471

## Acknowledgement

This research was partially supported by the Ministry of Education, Science, Sports and Culture, Grant-in Aid for Scientific Research(A), 2024-2028（24H00329, So Kazama）and JSPS KAKENHI Grant Number 23KJ0183.

# Assessing agricultural drought vulnerability in Indonesia using 1-km gridded crop yield dataset

○ Amalia Nafisah Rahmani IRAWAN[1,2*] & Daisuke KOMORI[1,2]
[1] Green Goals Initiative, Tohoku University, Miyagi 980-8572, Japan.
[2]Graduate School of Environmental Studies, Tohoku University, Miyagi 980-0845, Japan.
[*]E-mail: amalia.nafisah.rahmani.irawan.e2@tohoku.ac.jp

## Abstract

Climate change is intensifying drought conditions worldwide, posing serious threats to agricultural production, food security, and rural livelihoods—particularly in developing countries like Indonesia. This study assesses agricultural drought vulnerability across Indonesia by integrating drought hazard and crop-yield risk indicators at a 1-km spatial resolution from 2001 to 2021. A comprehensive gridded dataset of paddy crop yield during the dry season was developed using a hybrid approach that combines census-based government statistics with model-based remote sensing data derived from MODIS vegetation indices (NDVI) and shortwave radiation to estimate Net Primary Productivity (NPP). The resulting dataset shows strong agreement with the Earthstat Crop Yield dataset ($R^2$ = 0.79), confirming its reliability. Drought hazard was quantified using the Standardized Precipitation and Evapotranspiration Index (SPEI) computed from ERA5-Land precipitation and evapotranspiration data. Agricultural risk was evaluated through yield anomalies obtained by detrending the long-term yield time series, representing drought-induced productivity losses. The combination of these indicators enabled the identification of drought vulnerability hotspots, particularly in major agricultural regions such as Java, South Sumatra, and South Sulawesi. The findings demonstrate the value of high-resolution satellite-based datasets for accurately mapping drought vulnerability and understanding spatial variability in crop responses. This research provides essential insights for developing targeted drought adaptation strategies and strengthening agricultural resilience to climate change, contributing to sustainable food production and risk-informed agricultural planning in Indonesia.

## 1 Introduction

Agricultural drought remains one of the most critical challenges affecting food security and rural livelihoods in developing countries like Indonesia. Climate change, water scarcity, and shifting rainfall patterns intensify drought frequency and severity, threatening crop productivity. Crop yield—expressed as the amount harvested per unit area—is a key indicator for understanding agricultural productivity and resilience under such stresses. Over the last fifty years, yield growth has been the primary driver of increased production, rather than the expansion of harvested areas (Blomqvist et al., 2020). Although global crop yields have generally improved through technological and management advancements, regional disparities persist, especially in data-scarce areas. Existing global yield datasets often rely on coarse resolutions and fixed cropping calendars that fail to capture local variability.

Therefore, this study develops a high-resolution (1 km) paddy crop yield dataset for Indonesia's dry cropping seasons (2001–2021) by integrating census-based agricultural data from government sources with model-based estimates derived from remote sensing products. Indonesia was selected as the study area due to its intensive agricultural activities, characterized by three cropping seasons—two of which occur during the dry season and contribute approximately 55% of the nation's annual rice production. Furthermore, by combining the risk index, derived from yield anomalies, with the hazard index, represented by the Standardized Precipitation and Evapotranspiration Index (SPEI), this study examines the spatial pattern of agricultural drought vulnerability across Indonesia.

## 2 Materials and methods

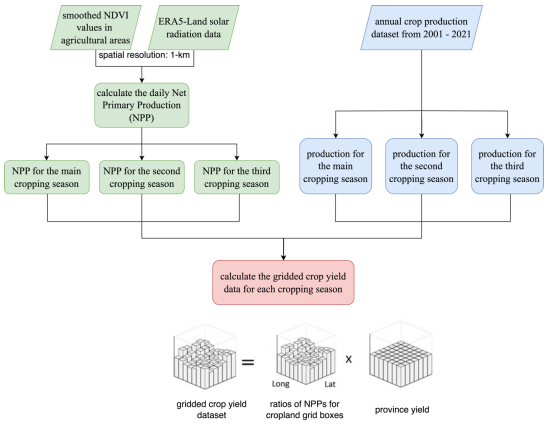


**Fig. 1. Flowchart to develop gridded crop yield dataset.**

**Fig. 1.** show the flowchart to develop the gridded crop yield dataset at 1-km resolution. Generally, the methodology is adapting the same approach used to develop the GDHY dataset (Iizumi et al., 2006; Iizumi & Sakai., 2020), but the observed yield dataset was obtained from the Ministry of Agriculture and the Statistic Bureau of Indonesia at the regency level instead of FAO dataset at the country level. Additionally, the Net Primary Productivity (NPP) is used as an indicator for estimating the crop yield on a grid cell. NPP was selected mainly because it quantifies the amount of biomass produced by plants, which directly relates to the amount of crop yield. Higher NPP typically means more biomass, and consequently, more potential crop yield.

## 3 Results and discussion

### 3.1 Development of Dry-Season Crop Yield Dataset

This study produced a 1-km resolution gridded crop yield dataset for Indonesia's dry cropping seasons (2001–2021). The dataset represents the second (February–May) and third (June–October) cropping seasons, accounting for over half of the country's annual rice production. **Fig.2.** illustrate spatial variability in rice production across Indonesia for 2003, 2010, and 2019, with detailed views provided for Java Island, the nation's most intensively cultivated region.

No existing dataset matches this study's combined spatial and temporal resolution. Validation was conducted by comparing the derived yield data with global datasets, specifically the Global Dataset of Historical Yields (GDHY) and EarthStat. The 1-km yield dataset exhibited strong consistency with the EarthStat 2005 rice yield data ($R^2$ = 0.79), confirming its robustness. Spatial correlation with GDHY also demonstrated similar trends, though variability was observed in heterogeneous regions due to differences in data scale and reference inputs.

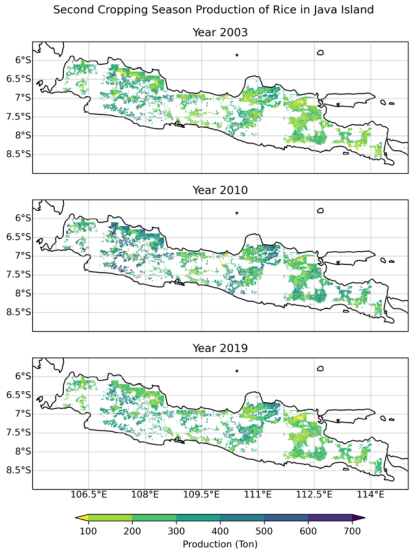


**Fig. 2. Example of the second cropping season production in Java Island.**

### 3.2 Agricultural Drought Vulnerability Assessment

Using the developed crop yield dataset, agricultural drought vulnerability was quantified by combining the risk index (normalized yield anomalies) with the hazard index (cumulative SPEI-3) for both dry cropping seasons. The resulting maps (**Fig. 3.**) reveal distinct spatial patterns of drought vulnerability across Indonesia. High-vulnerability areas are concentrated in Java, South Sumatra, and South Sulawesi—regions characterized by dense rice cultivation and limited irrigation resilience. The second cropping season shows broader areas of elevated vulnerability, while the third season exhibits more scattered patterns, reflecting variable planting schedules and residual soil moisture.

A quadrant-based classification was applied to categorize agricultural areas into four groups:

a. High vulnerability–Low drought (Yellow) – regions with substantial yield loss under moderate drought, indicating low adaptive capacity.
b. High vulnerability–High drought (Red) – critical hotspots where intense drought and severe yield loss coincide.
c. Low vulnerability–Low drought (Green) – resilient zones maintaining productivity under mild conditions.
d. Low vulnerability–High drought (Black) – areas showing strong adaptive response despite frequent drought.

This classification highlights spatial contrasts in exposure, sensitivity, and adaptive capacity. Red and yellow zones emphasizing the need for targeted interventions such as improved irrigation infrastructure and farmer support systems. Conversely, black and green zones suggest effective drought adaptation strategies, which may serve as resilience models for other regions.

Overall, the integration of high-resolution yield and climatic data provides new insights into the spatial dynamics of agricultural drought vulnerability in Indonesia. The dataset offers a valuable foundation for long-term drought risk monitoring, guiding region-specific adaptation and sustainable agricultural planning under future climate uncertainty.

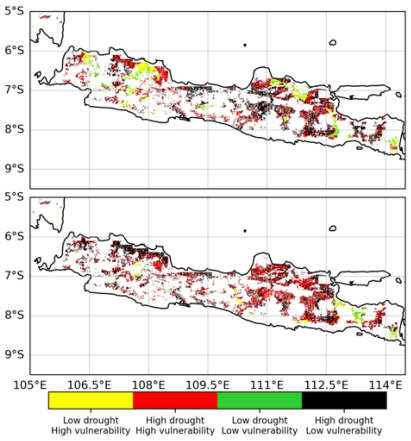


**Fig. 3. Agricultural area category based on the drought and vulnerability index for the second (upper image) and third (lower image) cropping season in Java Island**

## 4 Conclusions

This study developed a 1-km resolution paddy crop yield dataset for Indonesia's dry cropping seasons (2001–2021) by integrating MODIS-based NDVI, ERA5-Land radiation, and official agricultural statistics. The dataset, validated against global references ($R^2$ = 0.79), enables detailed assessment of agricultural drought vulnerability by combining yield anomalies with the Standardized Precipitation and Evapotranspiration Index (SPEI). Results revealed pronounced drought vulnerability hotspots in Java, South Sumatra, and South Sulawesi, where high exposure and limited adaptive capacity coincide. The analysis also identified resilient regions that sustain productivity under frequent droughts, underscoring the role of irrigation and adaptive practices. Overall, this study provides a robust foundation for data-driven drought monitoring and targeted adaptation planning to enhance agricultural resilience under increasing climatic stress.

## References

[1] Blomqvist L, Yates L and Brook B W 2020 Drivers of increasing global crop production: a decomposition analysis Environ. Res. Lett. 15 0940b6
[2] Iizumi, Toshichika, Masayuki Yokozawa, Gen Sakurai, Maria Isabel Travasso, Vladimir Romanenkov, Pascal Oettli, Terry Newby, Yasushi Ishigooka, and Jun Furuya. "Historical changes in global yields: major cereal and legume crops from 1982 to 2006." Global ecology and biogeography 23, no. 3 (2014): 346-357.
[3] Iizumi, T.; Sakai, T. The global dataset of historical yields for major crops 1981–2016. Sci. Data 2020, 7, 1–7.

# Municipality-level future assessment of exposed population due to heavy rainfall disasters

○ Tomoaki MATSUURA[1*], So KAZAMA[1]
[1]Department of Environmental Engineering, Environmental University, Miyagi 980-8579, Japan.
[*]E-mail: matsuura.tomoaki.p7@dc.tohoku.ac.jp

## Abstract

Future changes in the population exposed to fluvial flood, pluvial flood, and slope failure due to climate and population change were evaluated for SSP1-1.9, SSP1-2.6, SSP2-4.5, SSP3-7.0, and SSP5-8.5, respectively. Exposed population due to fluvial flood and pluvial flood was defined as the population residing in the area where 45 cm or more of inundation occurred. Exposed population to slope failure was defined as the population living in the area where the probability of slope failure exceeded 80%. Exposed population change rate was higher for all SSPs in the order of pluvial flood, fluvial flood, and slope failure, and exposed population increase change for pluvial flood was particularly pronounced for SSPs 5-8.5. Exposed population was shown to be more strongly affected by population change than by climate change.

**Keywords:** *exposed population, municipality, climate change, population change, JSSP*

## 1 Introduction

Heavy rainfall disasters not only cause physical destruction to houses, infrastructure, and farmland, but also lead to the loss of livelihoods and long-term socioeconomic impacts. Such events have been expanding globally amid the increasing trend of extreme precipitation associated with climate change. According to the Sixth Assessment Report of the Intergovernmental Panel on Climate Change (IPCC AR6), the frequency and intensity of extreme precipitation events are projected to further increase as anthropogenic global warming progresses. Tellman et al. (2021) reported that between 2000 and 2015, the global population residing in flood-affected areas increased by 20–24%, which is nearly ten times higher than previously estimated. These quantitative findings indicate that heavy rainfall disasters will likely become more severe not only in terms of physical damage but also due to the expansion of the exposed population. In Japan, tax revenues are expected to decline due to population decrease, while social welfare expenditures will rise as the population ages, leading to a contraction of public investment. Under such conditions, it is essential to make effective use of land with low disaster risk and implement cost-effective disaster-prevention measures within limited financial resources. To achieve this, quantitative evaluation of the relationship between the spatial distribution of flood risk and future population distribution across the entire country is crucial. Therefore, this study aims to construct a scientific basis for effective disaster-risk reduction and sustainable national land planning by quantitatively estimating the future changes in exposed population in Japan under multiple Japan-specific Shared Socioeconomic Pathways (JSSPs), considering climate and population changes related to heavy-rainfall-induced hazards such as fluvial flooding, pluvial flooding, and slope failures.

## 2 Data set

### 2.1 Population data

The second version of the Japan-specific Shared Socioeconomic Pathways (JSSP) population scenarios, developed by the National Institute for Environmental Studies (NIES), was used. These data are provided at a tertiary mesh resolution of approximately 1 km × 1 km. For future population projections, data for the year 2100 were used under three SSPs: SSP1, SSP2, and SSP5. The baseline population data for 2015 were also obtained from the same version of the tertiary mesh population scenarios.

### 2.2 Rainfall and climate scenario data

For the fluvial flood analysis, rainfall data developed by Yamamoto et al. (2023) were used. These datasets consist of rainfall distributions with a spatial resolution of approximately 250 m × 250 m that generate design discharges corresponding to specific return periods at any given location. These datasets are hereafter referred to as probable flood-contributing rainfall distributions. In this study, the distributions corresponding to the 30-, 50-, 100-, and 200-year return periods were employed. For the estimation of hazard data related to pluvial flooding and slope failures, the extreme rainfall datasets developed by Kawagoe et al. (2023) were used. These datasets have a spatial resolution of 1 km and include extreme rainfall values corresponding to return periods of 5, 10, 30, 50, 100, and 200 years. As the climate data, the NIES2020 bias-corrected climate scenario datasets for Japan were utilized. These datasets were produced using the Cumulative Distribution Function-based Downscaling Method (CDFDM) based on the Coupled Model Intercomparison Project Phase 6 (CMIP6) framework. Five global climate models (GCMs) were used: MRI-ESM2-0, MIROC6, ACCESS-CM2, IPSL-CM6A-LR, and MPI-ESM1-2-HR, all provided at a tertiary mesh resolution. This study employed three climate scenarios—JSSP1-2.6, JSSP2-4.5, and JSSP5-8.5—and analyzed two time periods relative to the baseline climate (1981–2000) and the late-21st-century period (2081–2100).

## 3 Analysis Method

The fluvial flood analysis was conducted based on the method developed by Yanagihara et al. (2023). The analysis was performed at a spatial resolution of approximately 250 m (fifth mesh). For further methodological details, readers are referred to Yanagihara et al. (2023). Similarly, the pluvial

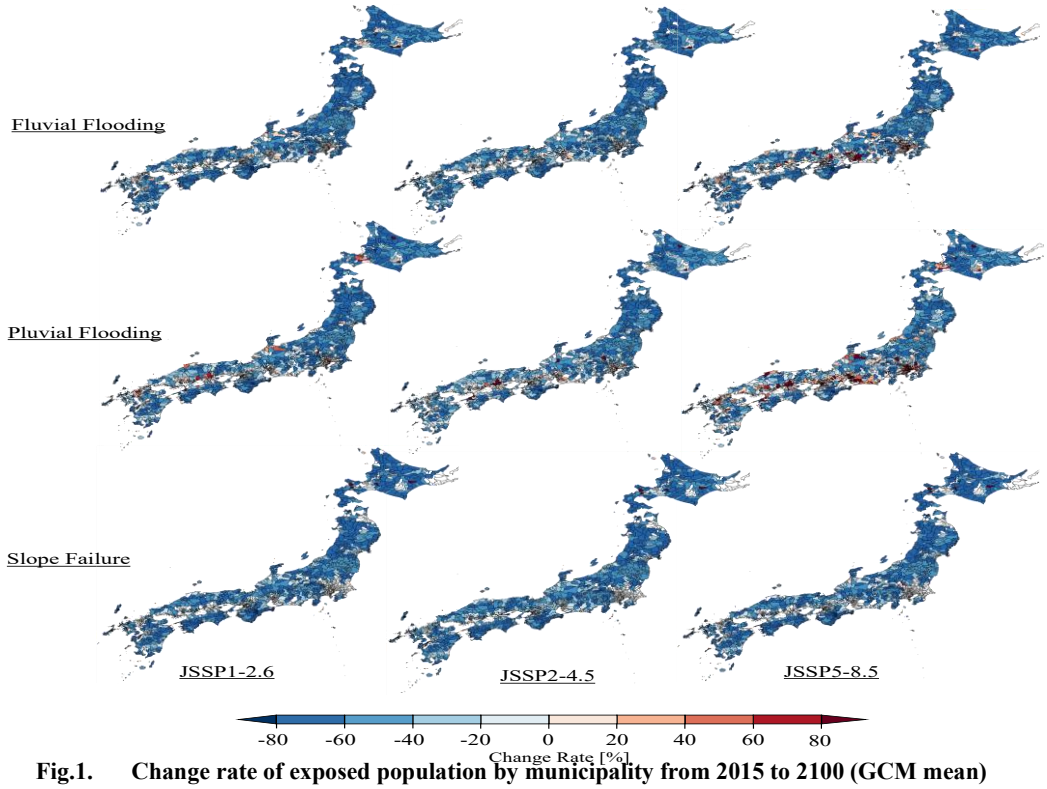


**Fig.1. Change rate of exposed population by municipality from 2015 to 2100 (GCM mean)**

flood analysis was carried out following the approach proposed by Yanagihara et al. (2023), with the same spatial resolution of fifth mesh. Detailed descriptions of the analytical framework can be found in the same reference. For slope failure hazard assessment, the probability of slope failure occurrence developed by Kawagoe et al. (2023) was employed. This dataset provides nationwide slope failure probabilities corresponding to daily rainfall amounts of 0, 50, 100, 150, 200, 250, 300, and 500 mm, with a spatial resolution of 1 km (tertiary mesh). In this study, slope failure probabilities corresponding to the 5-, 10-, 30-, 50-, 100-, and 200-year return period extreme rainfall values (also provided by Kawagoe et al., 2023) were derived through linear interpolation. The exposed population due to fluvial and pluvial flooding was defined as the population residing in areas where inundation depth exceeded 45 cm (above-floor flooding). The exposed population due to slope failures was defined as the population living in areas where the slope failure probability exceeded 80%. The exposed population was evaluated in terms of its annual expected value.

## 4 Results and Discussion

Figure 1 shows the municipality-level change rates of the exposed population due to fluvial flooding, pluvial flooding, and slope failures. The results indicate that in most parts of Japan, the exposed population is projected to decrease. This finding suggests that Japan's overall population decline and rural depopulation are dominant factors determining future exposure, outweighing the effects of hazard changes driven by climate change. In mountainous regions in particular, depopulation leads to a general decrease in the number of people exposed to hazard risks. n contrast, for fluvial and pluvial flooding, localized increases in exposed population were observed in major metropolitan areas such as Tokyo, Osaka, and Nagoya. This tendency is especially pronounced under the JSSP5-8.5 scenario, which assumes strong population concentration in urban areas and represents the most severe climate scenario. Consequently, exposure increases in these regions are likely driven by both demographic concentration and intensifying climate hazards. These findings highlight the necessity of region-specific disaster risk reduction strategies rather than uniform nationwide measures. Maintaining community-based disaster resilience in depopulating rural areas, together with implementing advanced adaptation measures in densely populated urban regions, will be essential for effective and sustainable disaster management in the future.

## REFERENCES

[1] IPCC: Summary for Policymakers. In: Climate Change 2021: The Physical Science Basis. Contribution of Working Group I to the Sixth Assessment Report of the Intergovernmental Panel on Climate Change, p.4, Cambridge University Press, 2021.

[2] Tellman, B., Sullivan, J.A., Kuhn, C., Kettner, A. J., Doyle, C.S., B., S Brakenridge, G.R., Erickson, T.A. and Slayback D.A.: Satellite imaging reveals increased proportion of population exposed to floods. Nature, Vol.596, pp.80-86, 2021.

[3] Yamamoto, T., Kazama, S., Touge, Y., Yanagihara, H., Tada, T., Yamashita, T. and Takizawa, H.: Evaluation of flood damage reduction throughout Japan from adaptation measure taken under a range of emissions mitigation scenarios. Climate Change, Vol. 165, Issue 60, 2021.

[4] Kawagoe, S., Kazama, S. and Sarukkalige, R.: Probabilistic modeling of rainfall induced landslide hazard assessment, Hydrology and Earth System Sciences, Vol. 14, pp. 1047-1061, 2010.

[5] Yanagihara, H., Kazama, S., Yamamoto, T., Ikemoto, A., Tada, T. and Touge, Y.: Nationwide evaluation of changes in fluvial and pluvial flood damage and the effectiveness of adaptation measures in Japan under population decline, International Journal of Disaster Risk Reduction, Vol. 110, 104605, 2024.

# Verification of the Reproducibility of Extreme Precipitation in the Japanese Regional Reanalysis Data RRJ-Conv

○Sachio IWABU[1], Yusuke HIRAGA[1], Ryotaro TAHARA[1], Ryota OHARA[2], and Junshi ITO[2]
[1]Graduate School of Engineering, Tohoku University; [2]Graduate School of Science, Tohoku University

**Abstract**

This study evaluates the reproducibility of extreme precipitation in the long-term Japanese regional reanalysis dataset RRJ-Conv by comparing it with ground-based AMeDAS observations. Approximately 800 AMeDAS stations without missing data from 1976 to 2020 were analyzed. RRJ-Conv precipitation was interpolated to each observation site using the Inverse Distance Weighting (IDW) method, and both the correlation and long-term trends of annual maximum daily precipitation were examined.The nationwide mean correlation coefficient was approximately 0.4, indicating a moderate level of reproducibility. Regionally, higher correlations were observed in Hokkaido and the Kinki region, whereas lower correlations were found in Kyushu and Okinawa.Trend analyses using Sen's slope and the Mann–Kendall test revealed a statistically significant increasing trend ($p \leq 0.05$) across Japan, suggesting that RRJ-Conv successfully captures the large-scale trends in extreme precipitation. However, RRJ-Conv tended to underestimate the magnitude of increase, particularly in Kyushu and Okinawa, where reproducibility was limited.These results suggest that RRJ-Conv is effective for identifying nationwide trends in extreme precipitation over Japan, although regional bias correction and further investigation into related climatic mechanisms remain necessary.

**Keywords: RRJ-Conv, precipitation extremes, long-term trend**

## 1. Introduction

Estimation of extreme precipitation plays a fundamental role in flood control and water management planning for individual river basins. Such estimations and their robustness strongly depend on the sample size. Conventional ground-based rain gauges are limited in number, making it difficult to accurately represent local hydrological characteristics, particularly in small and medium-sized river basins.

Although radar-based rainfall products (e.g., Radar–AMeDAS) provide spatially continuous information over wide areas, their record lengths are relatively short, and the estimation accuracy in mountainous regions remains insufficient. Consequently, in recent years, regional reanalysis data have been increasingly utilized to estimate extreme precipitation [1].

In Japan, the use of long-term regional reanalysis datasets is expected to enhance hydrological and climatological applications. However, the accuracy of such data, especially in terms of extreme precipitation, has not been thoroughly validated [2]. Therefore, this study aims to verify the reproducibility of extreme precipitation in RRJ-Conv through a comparison with ground-based AMeDAS observations.

## 2. Data and Methods

The Japanese Regional Reanalysis (RRJ-Conv), developed jointly by the Japan Meteorological Agency and Tohoku University, is a high-resolution (5 km grid) reanalysis dataset. This study targeted approximately 800 AMeDAS stations with no missing data for the period 1976–2020.To compare RRJ-Conv with station observations, the precipitation at each AMeDAS site was estimated by applying Inverse Distance Weighting (IDW) interpolation using the four surrounding RRJ-Conv grid points.The comparison focused on annual maximum daily precipitation, for which correlation coefficients were calculated. Additionally, long-term trends were analyzed for about 143 stations with continuous data from 1958 to 2020, using Sen's slope and the Mann–Kendall test.

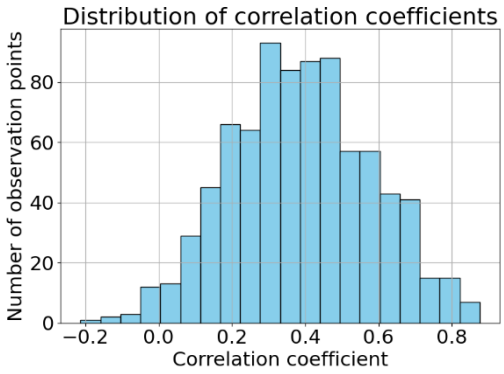


**Figure 1.** Histogram of correlation coefficients between RRJ-Conv and AMeDAS.

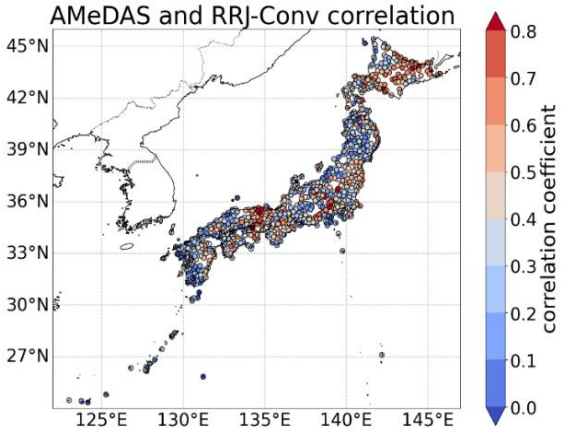


**Figure 2.** Spatial distribution of correlation coefficients across Japan (1976–2020).

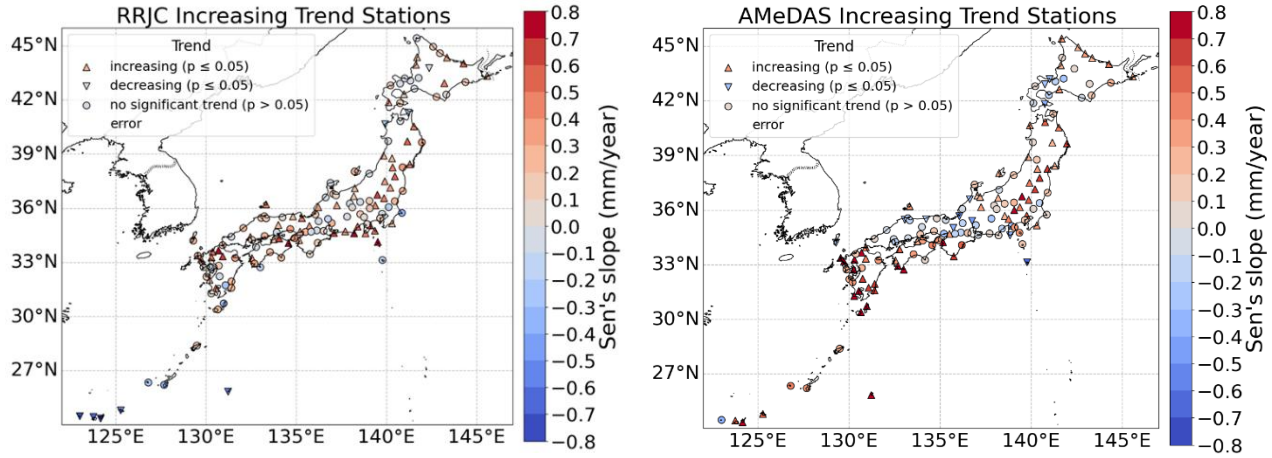


**Figure 3.** Spatial distribution of long-term trends in annual maximum daily precipitation during 1958–2020: (a) RRJ-Conv and (b) AMeDAS.

**Table 1.** Mean correlation coefficients and mean trend slopes for Japan and each region, and the proportions of stations showing statistically significant increasing, decreasing, or no trends.

| | | RRJC | | | | AMeDAS | | | | Number of locations |
|---|---|---|---|---|---|---|---|---|---|---|
| Area | Correlation | Slope | Increase | Decrease | Constant | Slope | Increase | Decrease | Constant | |
| All Areas | 0.389 | 0.173 | 0.364 | 0.056 | 0.580 | 0.248 | 0.427 | 0.084 | 0.490 | 143 |
| Hokkaido | 0.504 | 0.139 | 0.364 | 0.045 | 0.591 | 0.078 | 0.364 | 0.136 | 0.500 | 22 |
| Tohoku | 0.332 | 0.257 | 0.563 | 0.125 | 0.313 | 0.373 | 0.750 | 0.000 | 0.250 | 16 |
| Kanto | 0.417 | 0.229 | 0.429 | 0.000 | 0.571 | 0.260 | 0.429 | 0.071 | 0.500 | 14 |
| Chubu | 0.363 | 0.202 | 0.345 | 0.000 | 0.655 | 0.039 | 0.241 | 0.138 | 0.621 | 29 |
| Kinki | 0.508 | 0.210 | 0.455 | 0.000 | 0.545 | 0.144 | 0.273 | 0.091 | 0.636 | 11 |
| Chugoku | 0.350 | 0.179 | 0.231 | 0.000 | 0.769 | -0.004 | 0.154 | 0.154 | 0.692 | 13 |
| Shikoku | 0.405 | 0.307 | 0.444 | 0.000 | 0.556 | 0.519 | 0.556 | 0.000 | 0.444 | 9 |
| Kyushu | 0.291 | 0.229 | 0.318 | 0.000 | 0.682 | 0.617 | 0.636 | 0.045 | 0.318 | 22 |
| Okinawa | 0.206 | -0.556 | 0.000 | 0.714 | 0.286 | 0.457 | 0.571 | 0.000 | 0.429 | 7 |

## 3. Results

### 3.1 Correlation

The nationwide correlation coefficients of annual maximum daily precipitation between RRJ-Conv and AMeDAS showed a mean of approximately 0.4, following an approximately normal distribution (Fig.1).Regional variability was evident: Hokkaido and the Kinki region exhibited relatively high correlations (≥ 0.5), while Kyushu and Okinawa displayed lower correlations (Table1). Furthermore, variations among nearby stations were also observed, suggesting local differences in reproducibility (Fig. 2).

### 3.2 Trend Analysis

Long-term trends in annual maximum daily precipitation were evaluated for both AMeDAS and RRJ-Conv data using Sen's slope and the Mann–Kendall test (Fig.3, Table1). Both datasets revealed widespread statistically significant increasing trends ($p \leq 0.05$). Many stations along the Pacific coast from western to eastern Japan exhibited upward trends that were generally consistent between the two datasets. However, the average rate of increase in RRJ-Conv was smaller, indicating an underestimation of the magnitude of change.Regionally, RRJ-Conv slightly underestimated changes in Hokkaido, Tohoku, and Kanto, while overestimating them in Chubu, Kinki, and Chugoku. In contrast, Kyushu showed a large underestimation, and Okinawa even displayed a statistically significant decreasing trend, revealing distinct regional differences in reproducibility.

## 4. Conclusions

This study examined the reproducibility of extreme precipitation in the RRJ-Conv dataset through comparison with AMeDAS observations. The main findings are summarized as follows:

1. The nationwide average correlation of annual maximum daily precipitation between RRJ-Conv and AMeDAS was about 0.4, indicating moderate reproducibility, with higher values in Hokkaido and the Kinki region.
2. Long-term trend analyses revealed increasing trends across Japan, which RRJ-Conv generally reproduced, although it underestimated the magnitude of changes, particularly in Kyushu and Okinawa.

In summary, RRJ-Conv effectively reproduces large-scale trends in extreme precipitation across Japan, though regional biases remain. Future work will examine the causes of these biases such as tropical cyclones and other climatic factors and reassess the interpolation method (IDW) used in this study.

## References

[1] Bukovsky, A., Barsugli, J., Hoerling, M., et al. (2021): *Bull. Amer. Meteor. Soc.*, 102, E1859–E1880.

[2] Fukui, K., Sato, Y., Seko, H., et al. (2024): *Q. J. R. Meteorol. Soc.*, Early View.

# A Distributed Physically Based Modelling Approach for Identifying Pollutant Sources in Surface Waters

○ Kanchana WIJERATNA[1*], So KAZAMA[1*], Kumudu Madhawa KURUGAMA[1]
[1]Department of Civil and Environmental Engineering, Tohoku University, Miyagi 980-8579, Japan.
[*]E-mail: wanasuriya.mudiyanselage.kanchana.dasunpriya.wijeratna.q8@dc.tohoku.ac.jp

## Abstract

Tracing pollutant sources in complex river networks remains a challenging task for effective water quality management. Inverse modeling provides a theoretical basis for this purpose, but its practical application is often limited by ill-posedness and data constraints. This study presents the development of a distributed, physically based modeling framework designed to simplify the inverse problem under realistic field conditions. The framework integrates a forward pollutant transport model, based on the 1-D conservative advection equation and finite volume discretization, with an inverse component employing Non-Negative Least Squares (NNLS) for identifying contributing source branches at confluences. The approach is designed for systems where discharge, flow velocity, and pollutant signatures of potential sources are known or can be estimated. The framework is being developed and tested using simplified synthetic catchments to verify its stability and feasibility, and it is planned to be applied to the Kelani River Basin, Sri Lanka, as a case study. Preliminary implementations demonstrate how conservative mass balance and pollutant signature concepts can be combined to infer upstream sources from downstream observations. The framework provides a scalable foundation for data-informed pollutant source tracing in river basins.

**Keywords:** Surface water quality; Inverse modeling; Pollutant source identification; River network; Heavy metals; NNLS; Finite volume method; Hydrological modeling.

## 1 Introduction

Identifying pollutant sources along waterways is essential for effective water quality management [1]. However, tracing downstream pollutant signals back to their upstream origins is challenging in complex river networks with multiple confluences. While 'Inverse modeling' concepts provides a theoretical framework for this task, it is often ill-posed, leading to unstable or non-unique solutions that limit practical application [2].

Unlike conventional inverse models that rely solely on optimization, this study simplifies the problem to make it more applicable to real-world conditions, aiming to pinpoint potential pollutant sources responsible for observed downstream concentrations. The approach is suited to areas where major pollutant sources (e.g., industries or commercial zones) and their pollutant signatures, as well as hydrological characteristics such as discharge and flow velocity, are known or can be estimated.

The method focuses on heavy metals that behave conservatively, using a mass balance framework within a distributed hydrological model to estimate source strengths. It will be first tested on synthetic catchments and later applied to the Kelani River Basin, Sri Lanka, for validation using monitoring and industrial activity data [3], [4].

## 2 Materials and methods

This study considers two types of problems: (1) a single-channel problem and (2) a bifurcation problem. In the single-channel case, the objective is to identify the discharge characteristics of an upstream pollutant source based on downstream concentration signals. In the bifurcation case, the task is to determine which upstream branch contributes to the observed pollutant load at a confluence. Both setups combine forward transport simulations with inverse modeling to establish a general framework for source identification. The forward model describes pollutant transport using the one-dimensional conservative advection equation [5]:

$$\frac{\partial}{\partial t}(AC) + \frac{\partial}{\partial x}(QC) = S$$

Here, $A$ is the cross-sectional area [m²], $Q = Au$ is the discharge [m³/s], $u$ is the mean flow velocity [m/s], $C$ is the pollutant concentration [mg/L], and $S$ represents the source input [mg/(m·s)]. The model assumes pollutants behave conservatively, neglecting adsorption, decay, and lateral mixing, with each control volume treated as a perfectly mixed cell.

The finite volume method is used for spatial discretization. For a cell $i$ with length $\Delta x$, the mass balance is expressed as:

$$M_i^{n+1} = M_i^n - \frac{\Delta t}{\Delta x}(F_{i+1/2}^n - F_{i-1/2}^n) + \Delta t S_i^n$$

where $M_i = A_i C_i$ is the pollutant mass per unit length, $F$ denotes intercell flux, and $S_i$ is the integrated source term. The flux term is evaluated using an upwind scheme, ensuring numerical stability and preserving the physical flow direction.

### 2.1 Method at a Bifurcation for Apportionment:

At bifurcation points, pollutant signals from multiple branches are analyzed using their **chemical signatures**. Each source is assumed to have a distinct composition ratio of heavy metals (e.g., Cd, Cr, Pb, Cu, Zn), forming a unique signature vector. The measured downstream concentration vector $c$ is represented as a linear mixture of upstream sources:

$$c \approx x_A s_A + x_B s_B$$

where $s_A, s_B$ are source signatures and $x_A, x_B$ denote their respective contribution factors. Instantaneous mixing at the confluence is assumed, allowing the downstream concentration to be determined directly from upstream inputs and discharges (Fig.1).

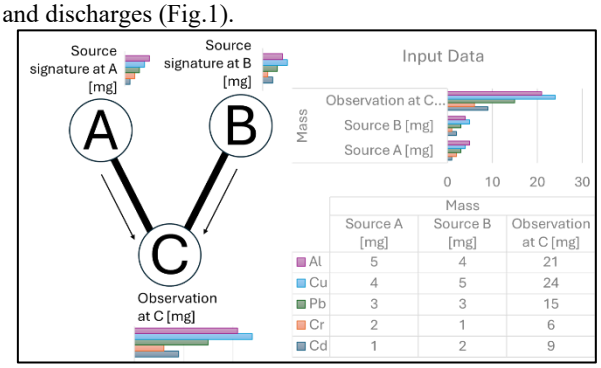


**Fig. 1. Schematic representation of Pollutant signatures and observations (example).**

The system is solved using the Non-Negative Least Squares (NNLS) method, which minimizes the residual $\| Sx - d \|_2^2$ under the constraint $x \geq 0$. The approach effectively identifies dominant sources, though it cannot distinguish between branches with identical signatures which is a condition rarely encountered in practice. The solution can be obtained using python operators (eg. *scipy.optimize.nnls)*, and the approach is easily extendable to handle multiple time series and complex river.

For model implementation, a two-step inverse procedure is followed: (1) solve for contributions at each bifurcation, and (2) evaluate upstream cells sequentially until the next confluence is reached.

The framework will first be tested on a synthetic 100 × 100 grid domain (1 km²) to verify stability and performance, then will be extended to the Kelani River Basin, Sri Lanka, for real-world evaluation. Furthermore, this approach ensures computational efficiency during the developmental stage, thereby reducing numerical cost while capturing the essential transport dynamics. The forward model is coded in Python, employing PCRaster framework [5], with future integration planned with the LISFLOOD [6] model to enable distributed-scale applications.

## 3 Results and discussion

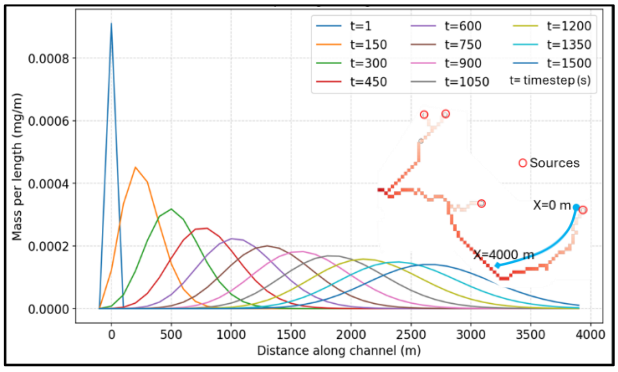


**Fig. 2. Simulated pollutant mass per unit length along the channel showing diffusive effect of first-order upwind scheme.**

The forward simulations were tested under steady pollutant discharge for first four time-steps, with a uniform velocity of 1.8 m/s across all channels. One time-step is assigned to 1 sec and grid size is 100mx100m in space.

Results showed a stable mass balance with negligible cumulative error, confirming the conservation property of the finite volume scheme (Fig.2).

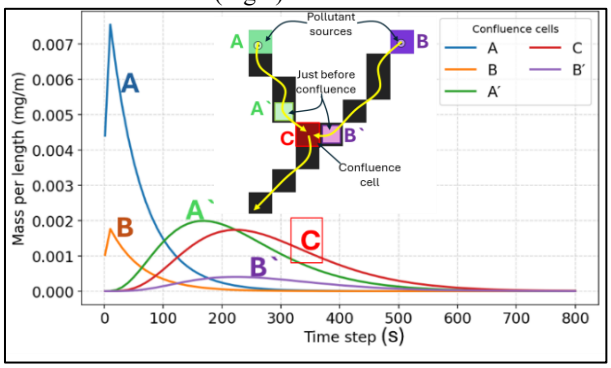


**Fig. 3. Pollutant mass near confluence vs. source cell.**

However, the use of a first-order upwind discretization introduced noticeable numerical diffusion, smoothing the pollutant fronts and limiting the model's ability to capture sharp plumes typical of heavy metal transport (Fig.2) . These results highlight the need for improved spatial accuracy. Future developments will focus on adopting higher-order schemes such as the Cubic Interpolated Propagation (CIP) method, assessing its performance under varying source conditions, and incorporating dispersion and adsorption processes for more realistic pollutant dynamics.

## 4 Conclusions

The proposed framework combines forward and inverse modeling to identify pollutant sources in river networks through a physically based, mass-conservative approach. The forward model provides stable transport simulations, while the NNLS-based inverse solver offers a practical means to resolve pollutant contributions at bifurcations. Ongoing improvements include extending the framework to handle multiple sources, variable discharges, and uncertainty, ensuring broader applicability for real-world river basin analyses such as the Kelani Basin.

## Reference

[1]Guidelines for drinking-water quality. WHO, 2011.

[2]M.B.Moghaddam, M.Mazaheri, J.M.V.Samani, "Inverse modeling of contaminant transport for pollution source identification in surface and groundwaters: a review," Groundwater for Sustainable Development, 2021, 100651.

[3]N.Wijayaweera, LN Gunawardhana, S Kazama, L Rajapakse, C.S. et al. Exploring spatial and seasonal water quality variations in Kelani River, Sri Lanka: a latent variable approach. Environ Monit Assess. 2024, 1063.

[4]A.Gunawardena, E.M.S.Wijeratne et al., "Industrial pollution and the management of river water quality: a model of Kelani River, Sri Lanka," Env. Monit Assess, 2017, 457.

[5]D. Karssenberg, O. Schmitz, P. Salamon, K. de Jong, and M. F. P. Bierkens, "A software framework for construction of process-based stochastic spatio-temporal models and data assimilation," Env. Modelling and Software, 2010, 489–502.

[6]L. Feyen, J. A. Vrugt, B. Ó. Nualláin, J. van der Knijff, and A. De Roo, "Parameter optimization and uncertainty assessment for large-scale streamflow simulation with the LISFLOOD model," J Hydrol (Amst), 2007, 276–289.

# Effects of River Management Abandonment on Aquatic Insect Diversity in Small and Medium Rivers

○ Keita KUBO[1*], So KAZAMA[1] & Yusuke HIRAGA[1]

[1]Department of Civil Engineering, Tohoku University, Miyagi 980-8579, Japan.
[*]E-mail: kubo.keita.r6@dc.tohoku.ac.jp

## Abstract

This study evaluated the impact of watershed changes associated with depopulation on biodiversity in three small river. The diversity of riverine animals was quantified using the Habitat Suitability Index (HSI) model. River management abandonment scenarios were simulated, leading to changes in hydrological parameters such as flow velocity, water depth, and water temperature. Field results showed that species composition was affected by canopy cover, but overall species diversity was not. The simulation revealed spatially varied impacts; habitat suitability increased in some tributaries under the abandonment scenario, linked to increased distance from urban areas. We conclude that management extensification alters community structure rather than overall diversity, with location-dependent outcomes. Future work will refine the HSI model for broader applicability.

**Keywords:** *management abandonment, aquatic insects, habitat suitable index model, species diversity*.

## 1 Introduction

In recent years, the maintenance and management of small and medium rivers across Japan have become increasingly difficult due to budget and personnel shortages, driven by depopulation and the impacts of climate change. In response to this situation, "management abandonment", a strategy that involves intentionally reducing the intensity of river maintenance, has been proposed[1)]. Changes in the river environment resulting from management abandonment, such as the formation of in-stream tree communities and the collapse of revetments, have been reported. However, much remains unclear about the effects of such extensification on river ecosystems. In particular, the increase in in-stream tree communities is known to affect flow regimes and has been suggested to potentially impact the community structure of aquatic insects, which play a crucial role in river ecosystems [2)]. The objective of this study is to evaluate the effects of river environment extensification, associated with management abandonment, on the habitat of aquatic insects and the flow regime.

## 2 Materials and methods

### 2.1 Study areas and Dataset

The study areas are the Sukawa River basin in Yamagata Prefecture, and the Dangozawa and Otanigawa River basins in Mishima Town, Fukushima Prefecture (Fig.1). The data used for the runoff analysis are shown in Table.1. Flow velocity and water depth were calculated using the discharge rates estimated by Chiba *et al.*[3)]. The aquatic insect data included samples collected in the target basins from 2022 to 2024, in addition to data collected by Hamamoto *et al.*[4)] in the Natori River in 2006.

### 2.2 Sampled data

Sampling sites within the study basins were visually classified into two categories: sites with canopy cover ("covered") and sites without canopy cover ("uncovered"). We examined the differences in species composition and species diversity between the covered and uncovered sites.

**Table.1. Dataset**

| Data | References |
|---|---|
| Rainfall | Rader-AMeDAS composite precipitation |
| Temperature, Wind speed, Sunshine duration, Humidity | Sukawa: Yamagata AMeDAS Observatory<br>Ohtani: NIES Observatory |
| Flow rate | Chiba *et al.* [3)] |
| Elevation | Basic map information |
| River, Landuse | National land value information |

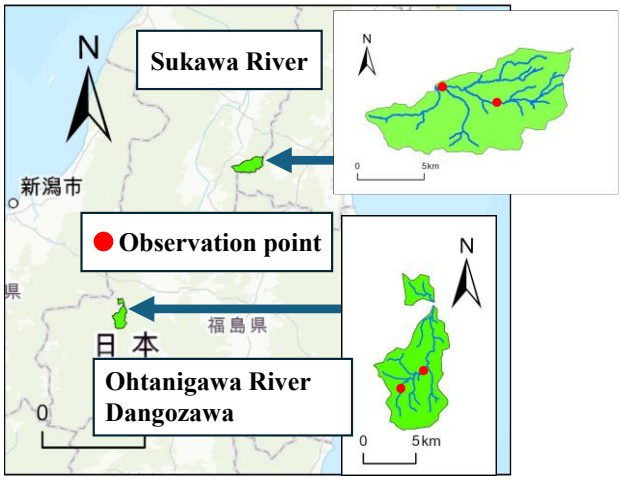


**Fig.1. The study area**

The Shannon-Wiener diversity index ($H'$) was used to assess species diversity. H' index was calculated using equation (1):

$$H' = -\sum_{i=1}^{S} \frac{n_i}{N} log \frac{n_i}{N} \quad (1)$$

Here S is the total number of species, $n_i$ is the number of individuals of the i-th species, and N is the total number of individuals of all species. A significance test was conducted to determine the difference in species diversity between the covered and uncovered sites.

### 2.3 Numerical model

A distributed runoff and water temperature model was used in the runoff analysis to simulate the river's hydrological environment. The estimated values based on 2022 data were considered the current scenario. The abandonment scenario assumed that all land use in the basin had changed to forest.

### 2.4 Habitat Suitability Index (HSI) model

The habitat suitability for aquatic insects was evaluated using the Habitat Suitability Index (HSI) model. The HSI is calculated from equation (2) using Suitability Index (SI) models, which evaluate habitat suitability for each environmental index on a scale from 0 (completely unsuitable) to 1 (optimal).

$$HSI = \left(\prod SI_j\right)^{\frac{1}{n}} \quad (2)$$

where $SI_j$ is the suitability index for the target species for environmental index j, and n is the total number of environmental indices. Based on the sampled data and the values of the environmental indices, frequency distribution tables were created to regressively develop the SI models. The environmental indices, categorized by the aspects they represent (a) disturbance, (b) water quality, and (c) food resources.

## 3 Results and discussion

### 3.1 Based on sampled data

The classification of the sampling sites resulted in four "covered" sites and five "uncovered" sites. A comparison of the H' index between the sites is shown in Fig. 2.

*Mataeopsephus japonicus*, which were found only at uncovered sites, are known to prefer environments with high canopy openness[2], a finding consistent with our results. The results of this study suggest that species composition differs between environments with and without canopy cover. Although the uncovered sites showed a tendency for slightly higher diversity than the covered sites, the difference was not statistically significant ( $p > 0.05$ ), suggesting that the presence or absence of canopy cover has a limited impact on species diversity.

### 3.2 Numerical analysis

The spatial distribution of the change in H' index (ΔH') in the Sukawa River basin from the current to the abandonment scenario is shown in Fig. 3.

Focusing on the southern tributary of the Sukawa River where $\Delta H' \geq 2.0$, the HSI value for the target species increased. This was because the land-use change associated with extensification resulted in a greater distance to urban areas. The distance to urban areas is one of the environmental indices that affects water quality. While these results suggest that an increased distance from urban areas enhances the habitat suitability for the target species, the impact of land use in mountainous river basins on water quality needs to be evaluated in future work.

## 4 Conclusions

This study yielded the following findings:

・Species composition differs depending on the presence or absence of canopy cover.

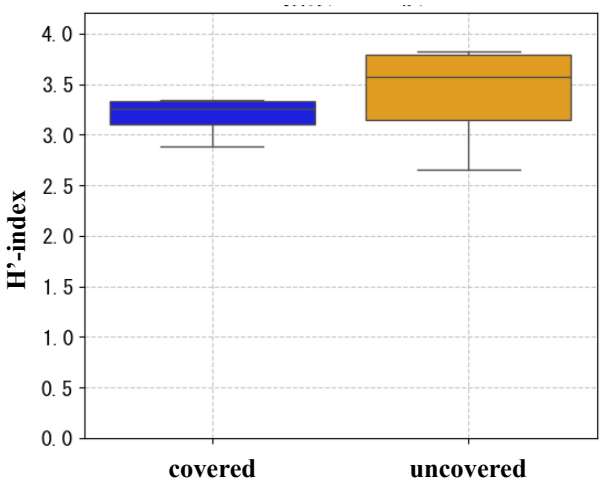


**Fig.2. H' index difference between covered and uncovered sites**

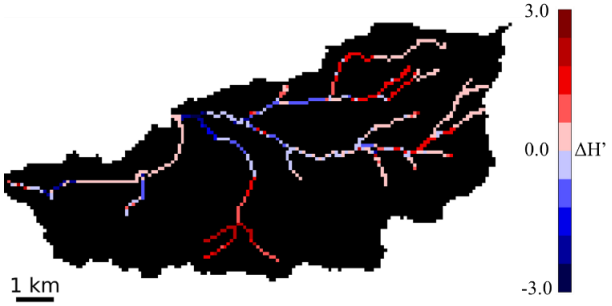


**Fig.3. The spatial distribution of the change in H' index (ΔH'), current to abandonment**

・There is no significant difference in species diversity between sites with and without canopy cover.

・The trend of changes in species diversity due to extensification varies among different river basins and tributaries.

In the future, we will reconstruct and improve the habitat suitability model to enable the evaluation of impacts from a wider variety of environmental changes. Furthermore, we will discuss the applicability of the habitat suitability model to larger river basins.

## Reference

[1] Kazama, S., Harada, M., and Hori, T.:Future Design of Small and Medium Sized Rivers Under Population Decline, *Japan Society of Hydrology and Water Resources*, Vol.37, No.3, pp.265-269, 2024.

[2] Mori, T., Miyake, H., and Shibata.E.:Impacts of riparian forest logging on stream invertebrate assemblages, *The Ecological Society of Japan*, Vol.55, No.2, pp.377-386, 2005.

[3] Chiba, K. and Kazama, S.:Assessment of changes in the flow of small river basins due to depopulation using a distributed runoff model, *JSCE B1*, Vol.78, No.2, pp.535-540, 2022.

[4] Hamamoto, H., Kazama, S., Watanabe, K., Sawamoto, M. and Omura, T.:Hierarchical Spatial Structure of Species Diversity Ofriverrine Benthic Faunal Community in South-central Miyagi Prefecture, *Annual Journal of Hydraulic Engineering, JSCE*, Vol.52, pp.1171-1176, 2008.

# Optimizing the Updating Frequency and Spatial Configuration of Streamflow Gauges for Improved Data Assimilation Performance in Poorly Gauged Basins

○ Kumudu Madhawa KURUGAMA[1*], So KAZAMA[1] & Yusuke HIRAGA[1]
[1]Department of Civil and Environmental Engineering, Tohoku University, Miyagi 980-8579, Japan.
[*]E-mail: kurugama.arachchige.kumudu.madhawa.r4@dc.tohoku.ac.jp

## Abstract

Flood modelling remains challenged by uncertainties in model structure, parameters, and observation availability, particularly in poorly gauged basins. To address these challenges, this study developed and evaluated a spatially distributed Hydrological Data Assimilation Framework (LISFLOOD-HDAF) that integrates the LISFLOOD, a distributed hydrological model with an Ensemble Kalman Filter (EnKF). The framework was utilized to assess how observation network characteristics: gauge density, spatial configuration, and assimilation frequency affect streamflow prediction skill. Observing-system simulation experiments (OSSE) were conducted in the Upper Po River Basin, Italy, covering six representative hydrological events (wet and dry), three update intervals (6, 12, and 24 h), and eight contrasting gauge network layouts. The EnKF consistently improved streamflow simulations relative to open-loop runs, with the largest gains observed downstream during wet events, where KGE assimilation indices reached 0.80–0.90 and RMSE reductions exceeded 50%. Assimilation frequency exhibited a non-monotonic influence: 12 h updates yielded the most stable basin-wide performance, while 6 h and 24 h updates were optimal for wet and dry headwater conditions, respectively. Dense or strategically balanced networks enhanced accuracy but with diminishing returns; five gauges with 12 h updates achieved near-optimal wet-season performance, whereas three to four gauges with 24 h updates sufficed in dry periods. The LISFLOOD-HDAF framework provides a robust, transferable tool for improving streamflow prediction and optimizing observation network design under data-scarce conditions.

**Keywords:** Ensemble kalman filter (EnKF); LISFLOOD; Distributed hydrological model ; Hydrological data assimilation; Flood forecasting.

## 1 Introduction

Floods are among the most frequent and destructive natural hazards, accounting for nearly 40% of weather-related disasters and causing severe human and economic losses globally [1]. Their increasing intensity, driven by climate change and urbanization, demands more reliable hydrological modelling for effective risk management. Despite advances in numerical weather prediction and early warning systems, flood modelling accuracy remains limited by uncertainties in model structure, parameters, and initial states. Accurately defining model initial conditions is particularly challenging in data-scarce basins, where sparse observations lead to poorly constrained soil moisture and groundwater states [2]. Data assimilation (DA) offers a robust solution by integrating observations with model simulations to improve state estimation and quantify uncertainty. While remote-sensing datasets provide broad spatial coverage, they often lack temporal precision, whereas in-situ discharge data directly represent catchment response and remain critical for improving streamflow prediction.

This study developed a spatially distributed Hydrological Data Assimilation Framework (LISFLOOD-HDAF) that integrates the LISFLOOD rainfall–runoff model with an Ensemble Kalman Filter (EnKF). Through synthetic experiments, it evaluates how gauge network design and assimilation frequency influence streamflow prediction skill, aiming to guide efficient, regime-specific observation network design in both gauged and poorly gauged basins.

## 2 Materials and methods

### 2.1 Study area

The study was conducted in the Upper Po River Basin, northern Italy. A 4,975 km² sub-catchment upstream of Pieve del Cairo was modelled using the open-source LISFLOOD dataset. The basin exhibits strong seasonal variability, with snowmelt–rainfall floods in spring, rainfall-driven floods in autumn, and low flows in summer and winter. Model simulations (2010–2017) included six representative hydrological events (wet; E1, E2, E3, E4 and dry; E5, E6) for evaluating LISFLOOD-HDAF performance.

### 2.2 Observing-System Simulation Experiments (OSSEs)

The EnKF is a sequential data assimilation technique that updates model states by optimally merging ensemble forecasts with observations while accounting for uncertainty [3]. In this study, Synthetic experiments were performedover 2010–2017, comprising deterministic, open-loop (OLS), and data assimilation simulations. The deterministic run generated “true” discharge, while OLS (without DA) and EnKF runs (with DA) used 30 ensemble members with stochastic perturbations to meteorological forcings. A network of 12 synthetic gauges was established, of which 9 were used for assimilation and 3 for validation (G2–upstream, G7-mistream, G12-outlet). Eight network configurations were tested, ranging from sparse to dense spatial coverage, alongside three assimilation intervals (6, 12,

and 24 h). These experiments enabled systematic assessment of how gauge density, placement, and update frequency influence hydrological performance under varying flow regimes.

Model performance was quantified with RMSE, NSE, and KGE, with normalized assimilation indices (RMSEAI, NSEAI, KGEAI) that scale gains relative to the "distance-to-perfection."

## 3 Results and discussion

The EnKF markedly improved model performance across all validation gauges and events relative to open-loop simulations (Fig. 1). The most substantial gains occurred at the downstream gauge (G12) during wet events, where RMSE reductions exceeded 50% and KGEAI/NSEAI values approached 0.8–0.9, particularly for multi-peak floods. Midstream performance (G7) also improved consistently, while upstream gains (G2) were smaller and more variable, reflecting the sensitivity of headwater catchments to localized errors and rapid hydrological responses.

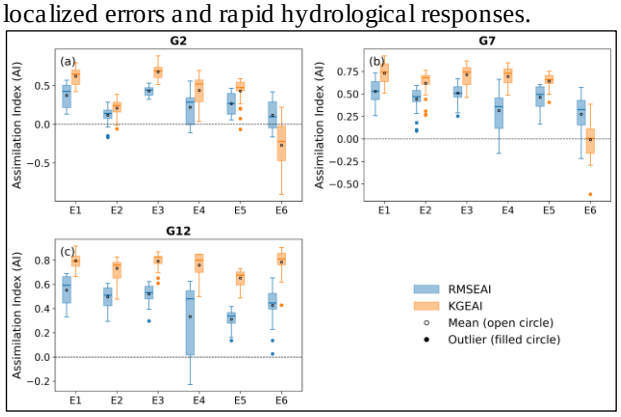


**Fig. 1. Event-level normalized assimilation indices**

Assimilation frequency showed a non-monotonic influence on performance. Basin-wide, 12 h updates provided the most consistent improvements, especially at G7–G12. In contrast, 6 h updates better captured rapid headwater responses during wet events, while 24 h updates were more effective in dry periods by reducing noise and over-correction. These trends were statistically validated using Friedman and Wilcoxon tests.

Gauge network design strongly influenced assimilation performance. Dense and strategically balanced networks outperformed sparse or poorly placed configurations, though performance gains diminished with each additional gauge. Downstream skill accumulated basin-wide, while headwater improvements were more sensitive to gauge placement. Statistical analyses ranked full or near-full networks highest, yet balanced hybrid layouts achieved comparable performance with reduced observational demand.

Interactions between assimilation frequency and network design revealed complementary effects. Dense or balanced networks amplified optimal-frequency benefits and reduced penalties under sub-optimal settings. Wet-season performance peaked with 12 h updates at mid- and downstream sites and 6 h at headwaters, while dry-season differences between 12 and 24 h were minimal. Performance–cost analysis identified efficiency thresholds: five gauges (12 h) achieved ~90% of maximum wet-season skill, and three to four gauges (24 h) sufficed in dry regimes (Fig. 2).

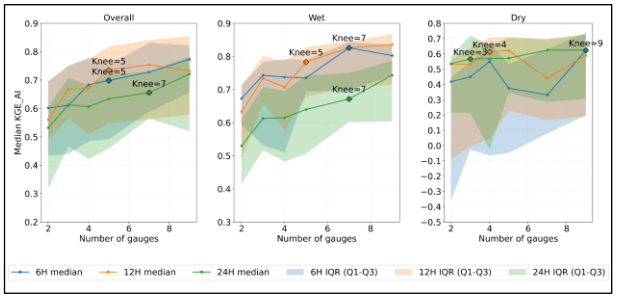


**Fig. 2. Performance–cost relationships between observation gauge density and assimilation frequency,**

The findings offer actionable guidance for operational hydrological management. Agencies can optimize assimilation strategies by aligning update frequency and gauge density with hydrologic regimes: 12 h updates with balanced networks maximize basin-wide reliability, 6 h intervals suit flashy headwaters during wet events, and 24 h updates suffice in dry periods. Normalized assimilation indices (AI metrics) enable consistent cross-site comparisons, while the knee-point analysis translates statistical improvements into cost-effective network design strategies.

## 4 Conclusions

The LISFLOOD-HDAF effectively enhanced streamflow prediction across varying hydrological regimes by assimilating distributed discharge observations using the EnKF while maintaining physical consistency. Assimilation frequency showed regime- and location-specific behavior: 12 h intervals yielded optimal basin-wide performance, whereas 6 h and 24 h updates were preferable in wet and dry headwater conditions, respectively. Network density and spatial configuration influenced accuracy, though improvements plateaued beyond moderate densities five gauges (12 h) during wet periods and three to four (24 h) during dry periods achieved near-optimal skill. The framework introduces a transparent, cost-effective workflow integrating OSSEs, normalized indices, and statistical analysis to guide observation network design. Future research should extend LISFLOOD-HDAF to multi-sensor assimilation and coupled hydro-hydraulic systems to enhance predictive resilience in data-scarce environments.

## Reference

[1] Gong, J., Weerts, A.H., Yao, C., Li, Z., Huang, 792 Y., Chen, Y., Chang, Y., Huang, P., 2023. State updating in a distributed hydrological model by ensemble Kalman filtering with error estimation. J. Hydrol. 620, 129450.

[2] Lahoz, W.A., Schneider, P., 2014. Data assimilation: making sense of Earth Observation. Front.Environ. Sci. 2. https://doi.org/10.3389/fenvs.2014.00016.

[3] Evensen, G., 2003. The Ensemble Kalman Filter: theoretical formulation and practical implementation. Ocean Dyn. 53, 343–367.

# Ensemble-Based Analysis of Line-Shaped Mesoscale Convective Systems

○ Ryotaro TAHARA[1*] & Yusuke HIRAGA[1]
[1]Department of Civil and Environmental Engineering, Tohoku University, Sendai 980-8579, Japan.
[*]E-mail: tahara.ryotaro.q7@dc.tohoku.ac.jp

## Abstract

Line-shaped mesoscale convective systems (LS-MCSs), known as “Senjo-Kousuitai” in Japan, frequently cause severe flooding and landslide disasters across the country. However, due to our limited understanding of their mechanisms, forecasting these systems remains difficult, particularly in the western part of northern Japan where prediction accuracy is low. This study aims to investigate how differences in atmospheric environments influence the intensity and location of precipitation associated with the LS-MCS that occurred over the western part of northern Japan in August 2022, using ensemble numerical simulations. A 288-member ensemble experiment using the WRF model was conducted. Empirical Orthogonal Function (EOF) analysis was applied to the 24-hour precipitation distribution to classify ensemble members according to variations in precipitation intensity and position. The first EOF mode (EOF1) represented variability in precipitation intensity, while the second mode (EOF2) captured north–south shifts in precipitation location. In the PC1-High subgroup representing stronger rainfall, the mid-level troughs and low-level cyclonic circulations were located farther east than PC1-Low, whereas EOF2 patterns corresponded to differences in the southward extension of the trough. These environmental differences likely enhance and shift the convergence zones, thereby determining the intensity and placement of precipitation.

**Keywords:** Line-shaped MCSs; Weather Research and Forecasting model (WRF); EOF.

## 1 Introduction

The line-shaped mesoscale convective systems (hereafter LS-MCSs), called “Senjo-Kousuitai” in Japanese, cause disasters almost every year in Japan. Due to the insufficient understanding of their mechanisms, forecasting LS-MCSs remains challenging, with particularly low prediction accuracy reported in the western part of northern Japan.

Previous studies have mainly conducted case analyses of LS-MCSs that occurred in those regions, examining the environmental conditions that contributed to the heavy rainfall in each case. Tochimoto and Hirokawa (2024) analyzed the LS-MCS that occurred in the northern part of Japan in August 2022 and showed that a meso-α-scale low over the Sea of Japan and strong low-level moisture flux contributed to heavy rainfall [1]. While previous studies have mainly focused on analyzing the atmospheric environmental characteristics when they occurred, it remains unclear what differences exist in atmospheric conditions and how they influence rainfall intensity and location caused by LS-MCSs.

The ensemble-based analysis can reveal the key controlling factors affecting differences in the targeted meteorological phenomena that occur under similar synoptic background environments [2]. Therefore, this study aims to investigate how differences in atmospheric environments influence the intensity and location of precipitation associated with the LS-MCS that occurred over the western part of northern Japan in August 2022 based on ensemble numerical simulations.

## 2 Materials and methods

### 2.1 Case Overview

A LS-MCS caused a persistent heavy rainfall event with a 24-hour total exceeding 600mm over the western part of northern Japan (the Sea of Japan side, especially Yamagata and Niigata Prefectures, Figure 1a). This rainfall was caused by a quasi-stationary front associated with a low-pressure system extending from the Sea of Japan, which stagnated over the Yamagata and Niigata Prefectures [3]. Moreover, warm and moist air originating from the edge of the Pacific High and typhoons flowed from the Tsushima Strait and Sea of Japan toward the front, resulting in heavy rainfall.

### 2.2 Numerical Weather Model

The Advanced Research version of the Weather Research and Forecasting Model (WRF-ARW) version 4.6.0 was used in this study [4]. Figure 1b shows the model domains. A two-way nesting configuration was used, consisting of domain 01 (horizontal resolution: 12 km) covering the whole of Japan and domain 02 (4 km) covering northern Japan. The model parameterizations followed Hiraga and Tahara (2025) [5]. The FNL 0.25-Degree Global Tropospheric Analyses and Forecast Grids (temporal resolution: 6 hours; spatial resolution: 0.25°) were used as the initial and boundary conditions. In this study, a 288-member ensemble simulation was conducted based on the Lagged Average Forecasting (LAF) method. Initial and boundary conditions were

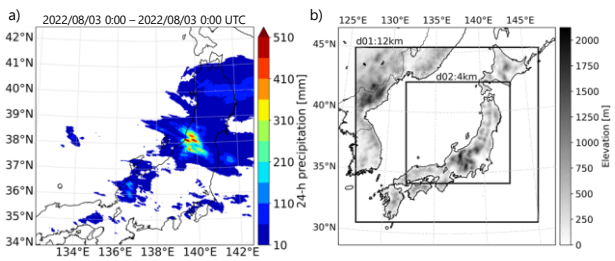


**Fig.1. a) radar/rain gauge observed 24-hour accumulated precipitation, b) WRF domain**

prepared every 10 minutes from 00:00 UTC 31 July to 00:00 UTC 2 August 2022 using linear interpolation of the FNL reanalysis data, resulting in 288 ensemble members. The analysis period was from 12:00 UTC 2 August to 00:00 UTC 4 August 2022.

### 2.3 Analysis Procedure

Empirical Orthogonal Function (EOF) analysis is a statistical technique that condenses information from a large dataset to examine its dominant patterns of variability [6]. In ensemble forecast, this method helps identify regions of low and high forecast uncertainty and extracts the main modes of spread or differences among members while removing redundant information. In this study, to classify the members exhibiting differences in precipitation intensity and location, EOF analysis was applied to the 24-hour precipitation distribution (from 00:00 UTC 3 August to 00:00 UTC 4 August 2022). Members within the upper and lower 5 percentiles of the principal component (PC) scores corresponding to the two leading EOF patterns (15 members each) were defined as representative subgroups of each EOF pattern (e.g. PC1-High). Figure 2 shows composite precipitation distributions of the subgroups derived from the two leading EOF patterns associated with the target case. EOF1 represents the variability in precipitation intensity, while EOF2 represents location differences of the precipitation along north-south direction.

## 3 Results and discussion

Figure 3 shows geopotential height (contours) and its differences (shading) at 500hPa and 850hPa (Z500 and Z850). A small-scale mid-level trough (Z500) and a low-level cyclonic circulation (Z850) are present over the Sea of Japan, moving eastward toward northern Japan. In the PC1-High group (red contours), the trough and low-level cyclonic circulation are located farther east compared to the ensemble mean (not shown), whereas in the PC1-Low group (black contours), they are located farther west, indicating a difference in the passage timing of these disturbances between PC1-High and PC1-Low. For PC2, PC2-High with the northern precipitation area shows a weaker southward extension of the trough and a more northward position of the cyclonic circulation, while PC2-Low with the southern precipitation area shows a stronger southward extension of the trough and a more southward position of the cyclonic circulation (not shown). The positional differences in the low-level cyclonic circulation may shift the convergence zone between the northwesterly flow behind the low and the southwesterly inflow from the southwestern Sea of Japan, thereby influencing the location of the precipitation area.

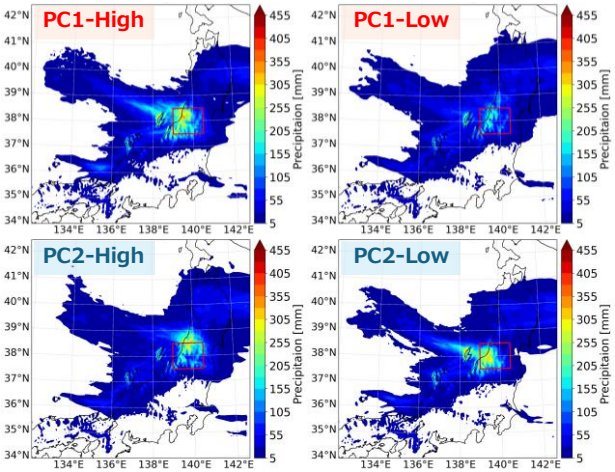


**Fig. 2. Composite precipitation distribution of the EOF subgroups**

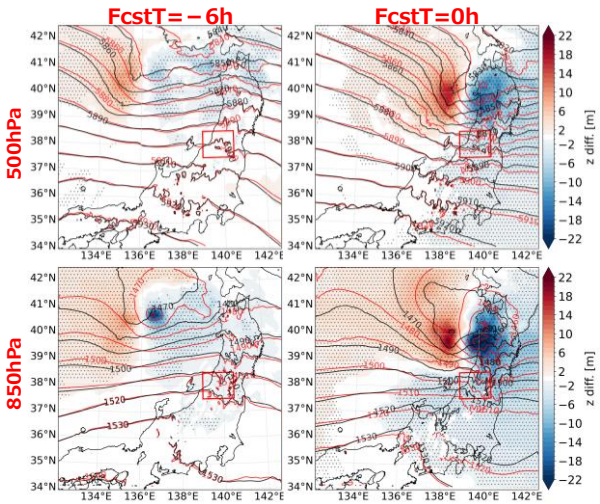


**Fig. 3. Z500 and Z850 of PC1-High (red contours) and PC1-Low (black contours), FcstT represents the time offset from the start of the 24-hour precipitation accumulation.**

## Reference

[1] Tochimoto, E., & Hirockawa, Y. (2024). Environmental Characteristics of an Extreme Rainfall Event in Yamagata-Niigata Prefectures, Japan, on 3-4 August 2022. SOLA, 20A-003.

[2] Shen, Y., Du, Y., & Chen, G. (2020). Ensemble sensitivity analysis of heavy rainfall associated with three MCSs coexisting over southern China. Journal of Geophysical Research: Atmospheres, 125(2), e2019JD031266.

[3] Japan Meteorological Agency (JMA). 2022. Heavy rainfall caused by the front from August 1 to 6. https://www.data.jma.go.jp/obd/stats/data/bosai/report/2022/20220822/jyun_sokuji20220801-0806.pdf (accessed 15 July 2025).

[4] Skamarock, W. C., Klemp, J. B., Dudhia, J., Gill, D. O., Barker, D. M., Wang, W., & Powers, J. G. (2005). A description of the advanced research WRF version 2 (No. NCARTN468STR).

[5] Hiraga, Y., & Tahara, R. (2025). Sensitivity of localized heavy rainfall in Northern Japan to WRF physics parameterization schemes. Atmospheric Research, 314, 107802.

[6] Hannachi, A., Jolliffe, I. T., & Stephenson, D. B. (2007). Empirical orthogonal functions and related techniques in atmospheric science: A review. International journal of climatology, 27(9), 1119-1152.

# Characteristics of Atmospheric River Driving Heavy Rainfall in Japan

○ Sohta TADAKI[1*], Yusuke HIRAGA[1] & Jose Angelo HOKSON[2]
[1]Hydro-Enviroment System Laboratory, Department of Civil Engineering,
Tohoku University, Miyagi 980-8579, Japan.
[*]E-mail: sota.tadaki.r5@dc.tohoku.ac.jp

## Abstract

In recent years, East Asia has experienced a significant increase in the frequency and intensity of heavy rainfall events. Such events are often driven by strong moisture transport in the form of atmospheric rivers (ARs). While previous studies investigated the association of ARs with rainfall events (i.e., rainfall-centric), our understanding of the physical characteristics of ARs causing heavy rainfall (i.e., AR-centric) remained unclear. Previous AR-centric studies in the region have primarily been event-based, making it difficult to generalize the physical characteristics of ARs responsible for heavy rainfall. In this study, we examined the characteristics of ARs from the AR perspective, using data from 1989 to 2023. We used the Global Atmospheric Rivers Dataverse, Version 4 for the detected Atmospheric Rivers. We then extracted the overlap between the detected ARs and our target area, which is Tohoku and Hokuriku region of Japan. The overlap for each AR events that was detected, we calculated the precipitation, Integrated Water Vapor Transport (IVT), Convective Available Potential Energy (CAPE), and Moisture convergence. We ran these values for each events into Machine Learning, with precipitation as the objective variable, and other variables as the explanatory variable to see which variable have the most impact on the precipitation. Our results revealed that each AR characteristic value exhibited a moderate level of correlation with precipitation, particularly moisture convergence. However, our model's score for the Machine Learning approach remained relatively low. To address this, we intend to enhance the model by employing more advanced Deep Learning models and incorporating a broader range of variables related to AR characteristics.

**Keywords:** Atmospheric River, IVT, extreme precipitation, Senjo-Kousuitai, Machine Learning.

## 1 Introduction

Recent years have witnessed a significant increase in frequency and intensity of heavy rainfall in East Asia[1)]. Such heavy rainfall events were shown to be driven by large water vapor transport in a phenomenon called Atmospheric Rivers (ARs)[2)]. ARs are flow of water vapor with a width of few hundred kilometers, and a length of few thousand kilometers. It is well established that ARs affect many regions of the world, particularly the west coast of North America and Europe, with heavy rainfalls[3)]. Their impacts on heavy rainfalls in East Asia are projected to be more pronounced under global warming[4)]. Kamae et al.[5)] comprehensively analyzed the proportion of the heavy rainfall caused by ARs in East Asia. They found 20-90% of heavy rainfall events were caused by ARs. Despite a growing understanding of the proportion of heavy rainfall events associated with ARs, our knowledge of the physical characteristics of ARs that trigger heavy rainfall events remains limited. In relatively moist regions such as Japan, the landfall of ARs does not necessarily lead to heavy rainfall, primarily due to the influence of complex topography and a convectively unstable atmospheric environment. Studies unraveling the physical characteristics of the ARs may contribute to better understanding of the occurrence of "Senjo-Kousuitai", which is a quasi-stationary band-shaped precipitation system[6)].

Building on previous studies, this study analyzed AR events over the past 35 years to examine their physical characteristics when associated with heavy rainfall in Japan. Through this analysis of the 35-year AR–rainfall relationship using the Global Atmospheric River Dataverse Version 4, we aim to identify key characteristics of ARs that contribute to heavy rainfall, including Integrated Water Vapor Transport (IVT) magnitude, Convective Available Potential Energy (CAPE), Mean Veryical Integral Moisture Convergence, and event duration.

## 2 Materials and methods

In this study, we used the Global Atmospheric Rivers Dataverse, Version 4, created by Guan and Waliser[7)] for the detected ARs.This is a dataset that detected the ARs globally using the ERA-5 reanalysis data from 1940 to 2023. We also used the ERA-5 reanalysis data for each IVT, CAPE, and Moisture Convergence. For the precipitation, we used the RadarAMeDAS data, which has a higher spatial resolution than ERA-5. Since this precipitation data only exists from 1988 onwards, our study period is 1988-2023.

Utilizing the Atmospheric River dataset, we delineated our study area. We determined the intersection between the identified Atmospheric Rivers and the target region, encompassing the Tohoku and Hokuriku areas of Japan. Subsequently, we computed each variable, including precipitation, within the intersection. By executing this process for each detected Atmospheric River, we obtained a three-dimensional dataset for each event. To facilitate the comparison of the impact of Atmospheric River characteristics on precipitation across different events, we calculated the maximum and average values for spatial and temporal resolution.

We put these values into Machine Learning, with Precipitation as objective variable, and IVT, CAPE, and Moisture Convergence as the explanatory variables. As the Machine Learning model, we chose Random Forest and XGBoost. These are both decision-tree based models, which will be

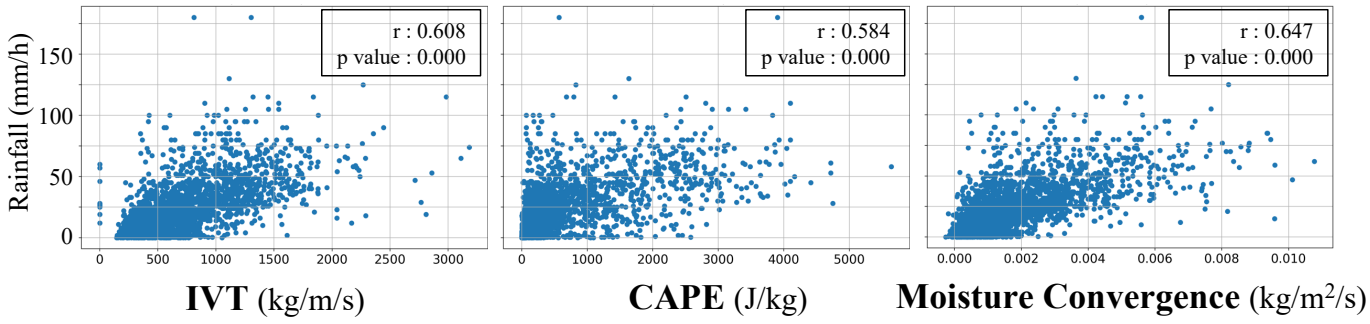


**Fig. 1.** Correlation of each variable against precipitation. Each plot represents different AR events, and r is correlation coefficient.

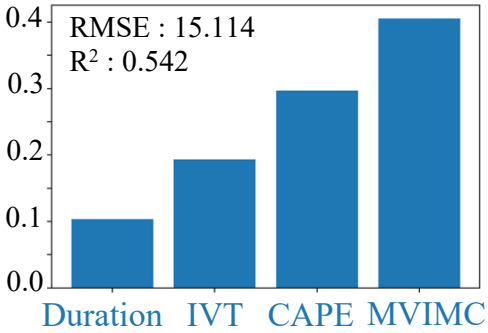


**Fig. 2.** Feature Importance in the XGBoost model of each variables representing AR characteristics

able to give us the importance of each feature. This will show us which variables has more impact on the increase of the precipitation caused by the ARs.

## 3 Results and discussion

We first compared the correlation between each variable and precipitation separately to look at the correlation coefficient (**Fig. 1**). Due to space constraints, we have presented only the results of the maximum spatial and temporal resolution. Notably, all three variables exhibited a moderate correlation with precipitation, with Moisture Convergence demonstrating the highest correlation coefficient.

**Fig. 2** shows the results of feature importance of each variable after running it through XGBoost Machine Learning model. We omitted the results of the Random Forest due to the lack of space. This result showed that moisture convergence had the highest importance. This analysis revealed that moisture convergence exhibited the highest importance. When compared to the findings of Figure 1, while moisture convergence remains the most significant variable, CAPE holds the second highest importance in the XGBoost model, which diverges from the earlier results. We can theorize that there are some specific conditions like the water vapor content, where the CAPE start to have an impact on the precipitation.

## 4 Conclusions

In this study, we analyzed the physical characteristics of ARs, including their IVT magnitude, CAPE, Moisture Convergence, and duration, with their association with the rainfall amount. Unlike previous rainfall-centric studies or event-based studies, this study is AR-centric and based on the long-term record (i.e., 35 years), using Machine Learning algorithms to analyze multiple characteristics at the same time and compare each importance.

Our results showed that Moisture Convergence has the most impact on the increase of the precipitation, both individually and combined with other variables at the same time. Meanwhile, CAPE showed different results between the individual correlation and Machine Learning. This indicates that it has an effect on the precipitation on a specific condition, which we need to analyze deeper.

Furthermore, the test scores of both Machine Learning models fell short of our expectations. This may be the result of the oversimplification of the AR event data, which we are reducing to a single value despite its original three-dimensional nature. We intend to incorporate a more sophisticated Deep Learning model to account for the data as it is detected and enhance the scores.

## Reference

[1] Takahashi, H. G., & Fujinami, H. : Recent decadal enhancement of Meiyu–Baiu heavy rainfall over East Asia. *Scientific Reports*, *11*(1), 13665, 2021.

[2] Guan, B., & Waliser, D. E. : Detection of atmospheric rivers:Evaluation and application of an algorithm for global studies. *Journal of Geophysical Research: Atmospheres*, *120*(24), 12514-12535, 2015.

[3] Ralph, F. M., Neiman, P. J., Wick, G. A., Gutman, S. I., Dettinger, M. D., Cayan, D. R., & White, A. B. : Flooding on California's Russian River: Role of atmospheric rivers. *Geophysical Research Letters*, *33*(13), 2006.

[4] Kamae, Y., Imada, I., Kawase, H. & Mei, W. : Atmospheric Ri vers Bring More Frequent and Intense Extreme Rainfall Events Over East Asia Under Global Warming. *Geophysical Research Letters*, Volume 48, 2021.

[5] Kamae, Y., Mei, W. & Xie, S. P. : Climatological Relationship between Warm Season Atmospheric Rivers and Heavy Rainfall over East Asia. *Journal of the Meteorological Society of Japan*, 95(6), pp.411-431, 2017.

[6] Kato, T. : Quasi-stationary band-shaped precipitation systems, named “Senjo-Kousuitai”, causing localized heavy rainfall in Japan. *Journal of the Meteorological Society of Japan. Ser. II*, *98*(3), 485-509, 2020.

[7] Guan, B., & Waliser, D. E. : A regionally refined quarter-degree global atmospheric rivers database based on ERA5. *Sci. Data* 11, 440, 2024

# An Integrative Assessment of Flood Control Efficacy and Maladaptation Risks Associated with Riparian Vegetation Clearing

○ Takaya KANEKO[1*], So KAZAMA[1]

[1]Department of Civil Engineering, Environmental Tohoku University, Miyagi 980-8579, Japan.
[*]E-mail: kaneko.takaya.q2@dc.tohoku.ac.jp.

## Abstract

The clearing of riparian vegetation is an increasingly prevalent climate change adaptation strategy to mitigate flood risk. This study provides a comprehensive assessment of this practice by addressing two critical knowledge gaps. First, we developed a two-dimensional unsteady flow model for the Natori River system that, unlike conventional models focused solely on channel roughness, incorporates the hydraulic effects of changes in channel conveyance caused by vegetation. Second, a nationwide flood analysis was conducted across Japan to quantify the municipal-level impacts on flood damage reduction and to identify the regional characteristics of maladaptation—a paradoxical outcome where the intervention exacerbates flood damage. Our hydrodynamic modeling reveals that accounting for channel conveyance provides a more realistic simulation of hydraulic responses, particularly concerning flow velocity and upstream overbank flow. The nationwide assessment demonstrates that while vegetation clearing reduces flood-related damages in a majority of municipalities (60.7%), it leads to increased damages in a significant minority (10.1%), predominantly in downstream areas and during large-scale flood events. These findings underscore that riparian vegetation clearing should not be uniformly applied as a flood control measure. Instead, its implementation necessitates careful, model-based planning tailored to specific watershed characteristics and flood scenarios to avert potential maladaptive consequences.

**Keywords:** Riparian Vegetation; Flood Risk Management; Hydraulic Modeling; Maladaptation.

## 1 Introduction

In recent years, frequent record-breaking rainfall events associated with climate change have intensified the need for effective flood control measures. The clearing of in-channel vegetation is gaining attention as a countermeasure that can enhance river flow capacity. This practice is considered a co-beneficial policy, contributing to both climate change adaptation (flood control) and mitigation (by maintaining carbon sinks). However, methods for evaluating its effectiveness are not well-established, with few studies distinguishing between the impact of vegetation on channel conveyance and its effect on channel roughness. Furthermore, there is a recognized risk of "maladaptation," where such interventions may inadvertently increase damage, yet related knowledge remains scarce. This study, therefore, evaluates the effects of riparian vegetation clearing through two approaches. First, we develop a 2D unsteady flow model for the Natori River system that incorporates changes in channel conveyance due to vegetation and compare its flood simulation results with those from a model considering only roughness. Second, we conduct a nationwide flood analysis for Japan to calculate the damage reduction effects of vegetation clearing by municipality and to identify the regional characteristics where maladaptation may occur.

## 2 Materials and methods

### 2.1 Model Comparison in the Natori River System

A flood analysis was conducted for the Natori River system using a 2D unsteady flow model with a 250 m mesh. The influence of vegetation was modeled in three scenarios: (1) as Manning's roughness coefficient, (2) accounting for changes in channel conveyance using a permeability coefficient for tree groups, and (3) accounting for conveyance changes using a drag coefficient for tree groups. The vegetation status was determined using tree height prediction data, while the Normalized Difference Vegetation Index (NDVI) derived from satellite imagery was used to calculate the roughness coefficient. The rainfall data was based on a probable flood-contributing rainfall distribution dataset.

$$\gamma g n^2 \frac{N\sqrt{N^2+M^2}}{D^{7/3}} \quad (1)$$

$$\frac{1}{K^2} g \frac{N\sqrt{N^2+M^2}}{h_a} \quad (2)$$

$$\frac{1}{2} C_D \frac{1-\gamma}{B} \frac{N\sqrt{N^2+M^2}}{D} \quad (3)$$

### 2.2 Nationwide Assessment in Japan

A nationwide flood analysis was conducted using a 2D unsteady flow model that incorporates the effect of vegetation into the roughness coefficient. The presence of vegetation was determined using NDVI from Sentinel-2 satellite imagery to calculate the pre-clearing roughness coefficient. The post-clearing roughness was set to 0.03, sassuming the presence of stumps. The annual expected damage was calculated using rainfall data for 30, 50, 100, and 200-year return periods, and the damage mitigation rate from before and after clearing was evaluated for each municipality.

Damage estimation was based on the "Manual for Economic Survey of Flood Control."

## 3 Results and discussion

### 3.1 Impact of Different Vegetation Evaluation Models

In the 200-year return period flood analysis for the Natori River system, no significant differences were observed in the distribution of maximum inundation depth among the models. However, an analysis of the differences in inundation depth revealed that models considering channel conveyance tended to show increased inundation upstream and decreased inundation downstream compared to the roughness-only model (Fig.1). This phenomenon is likely attributable to the fact that considering conveyance makes the upstream sections more prone to overflowing. The maximum flow velocity was higher in the models that considered channel conveyance than in the roughness-only model. The model using the drag coefficient, which can account for detailed flow changes due to tree groups, produced the highest velocity, suggesting it may better represent the actual hydraulic effects of in-channel vegetation. The estimated annual expected damage mitigation rate was 0.12% for the roughness model, whereas it was 0.37% for the channel conveyance model, indicating a more substantial mitigation effect.

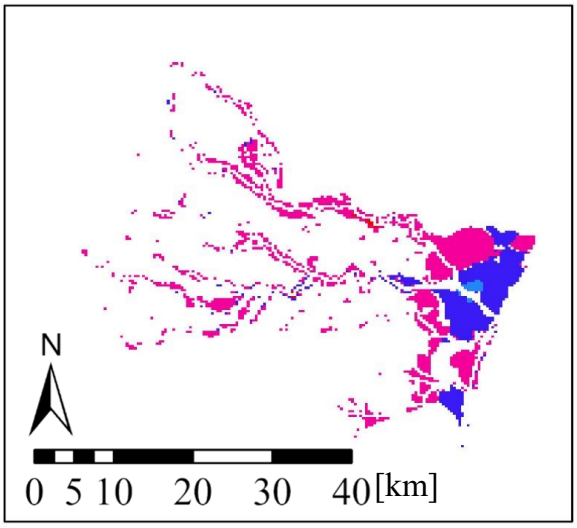


Fig.1 Difference in Flood Depth Between Roughness and channel conveyance

### 3.2 Occurrence of Maladaptation from Clearing

The nationwide analysis revealed that clearing riparian vegetation does not always mitigate damage (Fig.2). Areas with increased inundation depth after clearing were observed, particularly in the downstream parts of basins, a trend that became more pronounced with larger-scale floods. Maladaptation, where inundation depth increased in large-scale floods even in areas where it decreased in smaller floods, was confirmed. An analysis of annual expected damage by municipality showed that while 60.7% experienced a reduction in damage, 10.1% saw an increase. This indicates that improved flow capacity upstream can concentrate water downstream, potentially increasing damage. The results show that the effects of clearing are highly region-specific, requiring careful consideration of where to implement such measures.

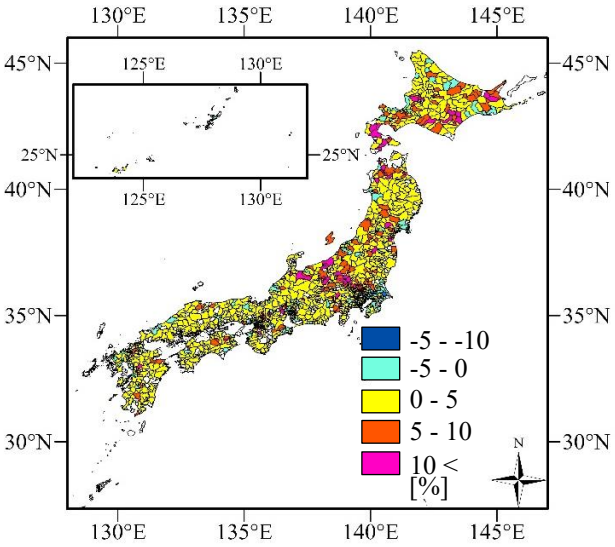


Fig.2 Damage Reduction Rate by Municipality

## 4 Conclusions

This study yielded the following insights:

1) When evaluating the impact of in-channel vegetation in flood analyses, considering changes in channel conveyance—in addition to the conventional roughness coefficient—can lead to more realistic simulations of phenomena such as flow velocity and overflow susceptibility.
2) While clearing riparian vegetation is effective in reducing flood damage in many regions, it was quantitatively shown that it can cause maladaptation, increasing damage in other areas, such as downstream portions of a watershed.
3) The effectiveness of clearing also varies with the scale of the flood; it may be effective for small- to medium-scale floods but counterproductive for large-scale floods.

These results suggest that future river management should not uniformly implement vegetation clearing as an adaptation measure. Instead, it requires careful planning based on detailed model-based assessments that consider the characteristics of the entire watershed and various flood scales.

## Reference

[1] Kaneko, K. et al., Quantitative evaluation of adaptation and mitigation effects of in-channel tree clearing against global warming, JSCE Journal B1 (Hydraulic Engineering), Vol. 81, No. 16, 2025.

[2] Koma T. et al., How should river embankments be spatially developed, from the upstream section or the downstream section?, Journal of Flood Risk Management 16, 2022.

# Assessment of Agricultural Suitability under Climate Change with Consideration of Disasters: The Case Study in California

○ Takuya MATSUMOTO[1*] & Yusuke HIRAGA[1]
[1] Department of Civil Engineering, Environmental Tohoku University, Miyagi 980-8579, Japan.
[*]E-mail: matsuoto.takuya.s2@dc.tohoku.ac.jp.

## Abstract
Climate change is recognized to influence the frequency and severity of disasters, making it essential to evaluate and discuss its effects on agricultural productivity and disasters simultaneously. The aim of this study was to estimate the viticulture suitability and to assess wildfire danger spatially under present and future climate scenarios. The multivariate viticulture suitability estimation model using MaxEnt showed good performance in predicting regional viticulture suitability. We found that the variability in precipitation and humidity largely determines the viticulture suitability in California under current climate conditions. Under future climate scenarios, areas currently characterized by intensive viticulture are projected to experience a decline in suitability, whereas northern regions are likely to see an increase. In these areas, wildfire danger is also expected to intensify.
**Keywords:** Wine; Species Distribution Modeling (SDM); MaxEnt; Agriculture.

## 1 Introduction
The quality of grapes and wine is well known to be strongly tied to a combination of climate, soil, geography, and culture, often referred to as “terroir”. Several studies scientifically showed the importance of terroir, particularly climate, in determining viticulture region distributions and their wine quality[2]. No wonder climate change is a big concern to the wine industry based on such linkage. Recent studies showed that climate change is expected to cause significant changes in viticulture suitability and wine quality in many regions of the world[3]. It is also known that the magnitude and frequency of disasters such as landslides, floods, and wildfires are changing. Therefore, it is important to simultaneously assess the impacts of climate change on both agricultural productivity and disasters. Based on the above, this study focuses on California, USA, where viticulture is prominent and the frequency of wildfires is particularly high, and aims to (1) develop a multivariate model to estimate viticulture suitability using high-resolution climate data; (2) estimate future changes in the viticulture suitability based on the climate projections; (3) spatially assess the relationship between viticulture suitability and wildfire danger.

## 2 Materials and methods
### 2.1 Suitability Estimation Model
The estimation of viticulture suitability was conducted using the maximum entropy method. The entropy $H$ is calculated according to Equation (1).

$$H = -\sum_{i=1}^{n} q_\lambda(x_i) ln q_\lambda(x_i) \quad (1)$$

where $H$ is the entropy, $x_i$ is the presence locations, and $q_\lambda(x_i)$ is the probability distribution. The probability density distribution $q_\lambda(x_i)$ that maximizes the entropy $H$ in equation (1) corresponds to the estimated distribution. As a result, the spatial distribution of suitability was obtained as shown in equation (2).

$$suitability = 1 - \exp\big(-\exp(H)\, q_\lambda(x)\big) \quad (2)$$

This study focused on the state of California, USA. A total of 379 vineyard site coordinates published by the California Wine Institute[4] were used as viticulture presence locations for the maximum entropy modeling.

This study used the gridMET (Abatzoglou, 2013)[5] and MACA (Abatzoglou, 2012)[6] to obtain the current and future climate in the study area. 14 environmental variables is used in the maximum entropy model: growing degree days (GDD) (°C), average temperature during the growing season (April 1st to October 31st) (MEAN) (°C), maximum temperature in the warmest month in the growing season (TMAX) (°C), minimum temperature in the coldest month in the growing season (TMIN) (°C), minimum temperature in the coldest month (TMIN-A) (°C), average diurnal temperature range (DTR) (°C), accumulated Precipitation during the growing season (PRECIP) (mm), annual precipitation (PRECIP-A) (mm), precipitation seasonality (CV), and average vapor pressure deficit during the growing season (VPD) (hPa). For these meteorological variables, mean values for the present (1980-2009, 30-year average), the near future (2040-2069, 30-year average), and the late 21st century (2070-2099, 30-year average) were derived from the MRI-CGCM3, HadGEM2-ES365, CNRM-CM5, IPSL-CM5A-MR, and CanESM2 models under the RCP2.6 and RCP8.5 scenarios.

### 2.2 Wildfire danger Assessment
The Fire Weather Index (FWI) is a widely used indicator of wildfire danger, derived from the Canadian Forest Fire Weather Index System. FWI is then calculated as a function of ISI and BUI, expressed as equation (3).

$$FWI = f(ISI, BUI) \quad (3)$$

where $f$ is a non-linear function defined in Van Wagner, 1987[7]. $ISI$ is computed from wind speed and fine fuel moisture code, and $BUI$ is computed from the Duff Moisture Code and Drought Code. The detailed formulas and parameterizations are provided in Van Wagner, 1987.

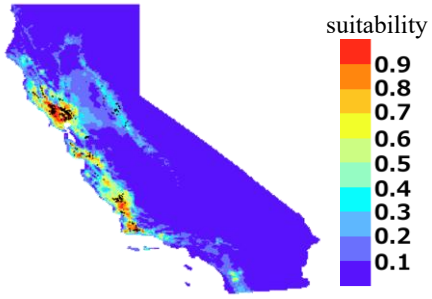


**Fig. 1. Suitability Estimation under the current climate**

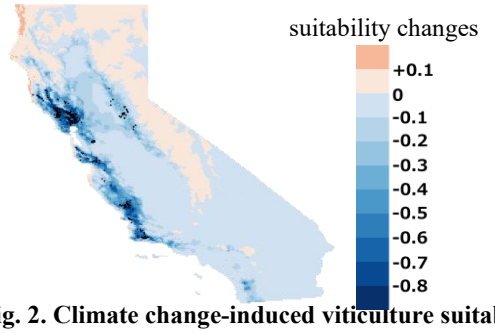


**Fig. 2. Climate change-induced viticulture suitability changes under RCP 8.5 for the late 21st century**

**Table 1. Percent contribution of the environmental variables**

| variables | contribution(%) | variables | contribution(%) |
|---|---|---|---|
| PRECIP-A | 27.38 | DTR | 6.13 |
| CV | 19.87 | TMIN-A | 6.11 |
| VPD | 18.79 | TMIN | 4.19 |
| MEAN | 9.08 | TMAX | 0.73 |
| GDD | 7.23 | PRECIP | 0.48 |

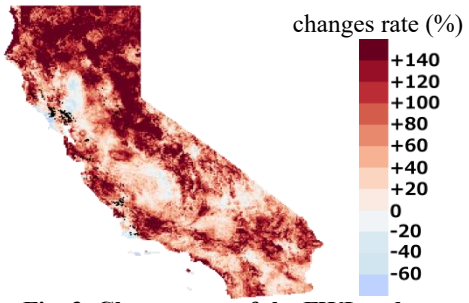


**Fig. 3. Change rate of the FWI under RCP 8.5 for the late 21st century**

## 3 Results and discussion

Fig. 1 shows the viticulture suitability under the current climate. The black dots indicate the presence locations. High suitability values are observed in coastal regions, where the density of presence data is also high. In contrast, in inland areas, relatively high suitability is found in the northern part, whereas the southern inland regions show lower suitability. The area under the curve (AUC), one of the model's performance metrics, was 0.959, indicating that the model accurately estimated suitable areas for viticulture in California.

Table 1 presents the percent contribution of each variable to the suitability estimation. The highest contributions were observed for PRECIP-A, CV, and VPD, which together accounted for approximately two-thirds of the total. The high importance of precipitation-related variables likely reflects the strong spatial variability of precipitation patterns across the study area.

Fig. 2 shows the difference in vineyard suitability between the late 21st century (RCP8.5 scenario) and the current climate. Overall, suitability is projected to decrease in most areas, whereas increases are observed in the northern coastal and inland regions. In contrast, suitability is expected to decline significantly in major current wine-producing regions such as Napa and Sonoma, indicating a potential northward and upward (higher elevation) shift in suitable areas.

Fig. 3 shows the change rate in wildfire danger between the late 21st century (RCP8.5 scenario) and the current climate. While wildfire danger is projected to increase across most of California, some coastal and arid inland areas show a decrease. Notably, wildfire danger is expected to rise in Napa, whereas it decreases along the Sonoma coast. Ideally, suitable regions would be those where suitability increases and wildfire danger decreases; however, no such regions were identified. In northern coastal areas where suitability increases markedly, wildfire danger is also projected to rise significantly. The Sonoma coastal region was the only area where a reduction in wildfire danger was observed, suggesting that, with appropriate adaptation measures, it may retain potential as a suitable area for viticulture under future climate conditions.

## 4 Conclusions

This study aimed to estimate and project the viticulture suitability and to spatially assess wildfire dangers. The results revealed that suitability increased in coastal regions, whereas it decreased in inland areas. The suitability model also indicated that variables related to moisture availability had the greatest influence on suitability estimation. Furthermore, wildfire danger was found to increase both in regions where viticulture is currently active and in areas projected to experience higher suitability under future climate conditions. Future research will focus on assessing and projecting grape quality while taking wildfire danger into consideration.

## Reference

[1] Jones, G. V., White, M. A., Cooper, O. R., and Storchmann, K.: Climate change and global wine quality, *Climatic Change*, Vol. 73, issue 3, pp. 319-343, 2005.

[2] Fraga, H., Santos, J. A., Malheiro, A. C., Oliveira, A. A., Moutinho-Pereira, J., and Jones, G. V.: Climatic suitability of Portuguese grapevine varieties and climate change adaptation, *International Journal of Climatology*, Vol. 36, issue 1, pp. 1–12, 2016.

[3] California Wine Institute. Navigate The State. https://discovercaliforniawines.com/wine-map-winery-directory/ (Accessed 2025-01-21)

[4] Abatzoglou, J. T.: Development of gridded surface meteorological data for ecological applications and modelling, *International Journal of Climatology*, Vol. 33, issue 1, pp. 121–131, 2013.

[5] Abatzoglou, J. T., and Brown, T. J.: A comparison of statistical downscaling methods suited for wildfire applications, *International Journal of Climatology*, Vol. 32, issue 5, pp. 772–780, 2012.

[6] Van Wagner, C. E.: Development and structure of the Canadian Forest Fire Weather Index System, *Canadian Forestry Service, Ottawa, ON*, Forestry Technical Report 35, 1987.

# Long-Term Flood Resilience in the Chao Phraya River Basin, Thailand: Evidence from Historical Temples

○ Zhaolong GU[1*], Daisuke KOMORI[2] & Sartsin Phakdimek[3]
[1]Graduate School of Environmental Studies, Tohoku University, Miyagi 980-0845, Japan.
[2]International Research Institute of Disaster Science, Tohoku University, Miyagi 980-8572, Japan.
[3]School of Geotechnology, Institute of Engineering, Suranaree University of Technology
[*]E-mail: gu.zhaolong.r5@dc.tohoku.ac.jp.

## Abstract

This study investigated long-term flood resilience in the Chao Phraya River Basin, focusing on Buddhist temples. Utilizing field measurements, the Rainfall-Runoff-Inundation (RRI) model, and exposure analysis, the study examined how temple architecture and location choice strategies reflect community adaptation to flood risks. Results showed that temples, designed with both ground elevation and the elevation for important structures, are resilient to floods, with regional variations in flood resilience strategies. Temples' locations and foundation types revealed the influence of local flood characteristics and cultural factors on flood risk management. These patterns demonstrated embedded long-term resilience and warranted further investigation of strategy implementation across flood-prone areas, informing basin-scale planning.

**Keywords:** Flood resilience, Rainfall-Runoff-Inundation (RRI) model, human-flood system

## 1 Introduction

In recent years, flood risk assessment research has increasingly focused on linking the social decisions related to exposure and vulnerability, such as disaster response measures and community expansion, with the hydrological processes. This approach clarifies the feedback loops between human actions and flood hazards, making risk assessment studies more prevalent in understanding flood dynamics. The Chao Phraya River Basin in Thailand, which both originates and receives runoff from several major cities, provides a critical setting for flood risk analysis. The basin's stable and long-standing seasonal flood regime allows local communities to adapt continuously, unlike the frequently shifting channels of Japan's steep-gradient rivers, which hinder the preservation of flood memory. The gentle slopes and stable inundation patterns of the Chao Phraya River enable better transmission of flood experiences across generations.

This unique combination of historical continuity and spatial diversity makes the Chao Phraya River Basin an ideal case for socio-hydrological inquiry. This study took the historical temples across the basin as the study targets. Historically positioned or raised to prevent flooding, these temples preserve paleo-flood evidence, including high-water marks and inscriptions, which support long-term human-flood system analyses. These temples also function as flood shelters, enhancing community resilience and providing valuable spatial data at the community level. This interdisciplinary study hypothesizes that the spatial distribution and architectural configurations of these temples reflect long-term community flood awareness, and aims to systematically compare human-flood feedback mechanisms in different parts of the basin.

## 2 Materials and methods

This study utilizes a multi-method approach to assess long-term flood resilience in the Chao Phraya River Basin, Thailand, focusing on Buddhist temples.

1. Field Survey: Physical measurements of 72 temples' "Pagoda" structures were taken during field investigations from September 26 to October 7, 2023. The necessary data is shown in Fig. 1. The definitions of the necessary data are as follows:

①. The total height increase relative to the surrounding terrain ($H_1$)
②. The foundation elevation of the structure "Pagoda" ($H_2$)
③. The ground elevation of the overall temple ($H_3$)


**Fig. 1. Schematic of a Buddhist temple "Pagoda".**

2. Flood Resilience of Temples analysis with RRI model simulation: The Rainfall-Runoff-Inundation (RRI) model was utilized to simulate flood scenarios for 10-year, 20-year, 50-year, and 100-year return periods. These simulations were based on probabilistic precipitation data, which incorporates varying probabilities of rainfall intensity to generate flood predictions. The model's simulated flood depths were then compared with the physical height of the temples' "Pagoda" structures to assess their flood resilience.

3. Exposure analysis: Exposure, defined as the location and topographic features of assets, plays a critical role in flood characteristics analysis. In this study, exposure (E) was quantified by simulating a 200-year return period flood event using the RRI model, normalizing the maximum inundation depth with a base value of 0.45 meters, the minimum floor height according to the Building Standards Law of Japan.
The formula is as follows:

$$\text{Indicator E} = \frac{\text{Simulated inundation depth (m)}}{0.45\ \text{m}} \quad (1)$$

4. Contribution of Elevation and Foundation: Temples were classified based on the proportion of natural elevation $H_3$ in their overall height $H_1$, and their flood resilience was compared with simulated flood depths to assess regional differences in flood management strategies.

## 3 Results and discussion

Analysis revealed that most temples' "Pagoda" structures maintain resilience during a 20-year return period flood event, as their total heights $H_1$ are sufficient to avoid the inundation. However, it is important to note that the heights of the "Pagoda", especially the artificial foundations for important structures ($H_2$), are influenced not only by local flood characteristics but also by cultural and religious factors. Further evidence was needed to substantiate the hypothesis that the construction of the temple "Pagoda" was influenced by the local flood characteristics.

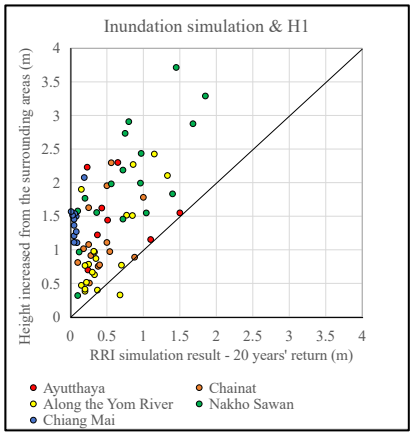


**Fig. 2. The comparison between the total height increase of the temple's "Pagoda" relative to the surrounding terrain ($H_1$) and the simulation results of flood scenarios for 20-year return periods.**

The study also identified a direct correlation between exposure and total height increased ($H_1$): as the exposure increased, the height of the temples' "Pagoda" relative to the surrounding terrain ($H_1$) also increased. This suggested that the construction of temples was influenced by local flood characteristics, with artificial foundation construction and site choice specifically aimed at mitigating flood risk.

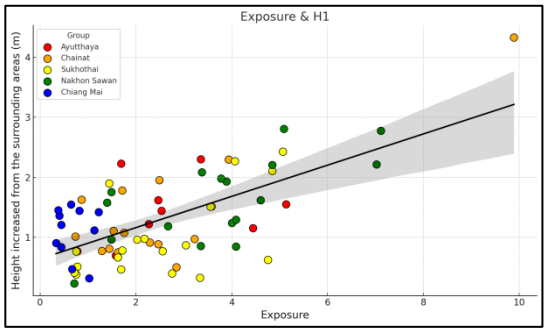


**Fig. 3. The relationship between the total height increase of the temple's "Pagoda" relative to the surrounding terrain ($H_1$) and the Exposure indicator.**

Furthermore, significant regional variations in flood resilience strategies were observed. In the lower reaches of the basin, such as Ayutthaya and Chainat, temple resilience primarily relies on the elevation of the important structure, "Pagoda" ($H_2$), whereas in the middle reaches, such as Sukhothai and Nakhon Sawan, resilience is more dependent on the artificial foundation for the overall temple ($H_3$). These findings underscored the critical role of both natural and anthropogenic factors in flood resilience and suggested that regional differences in flood awareness and preparedness can influence the strategies employed to mitigate flood risks.

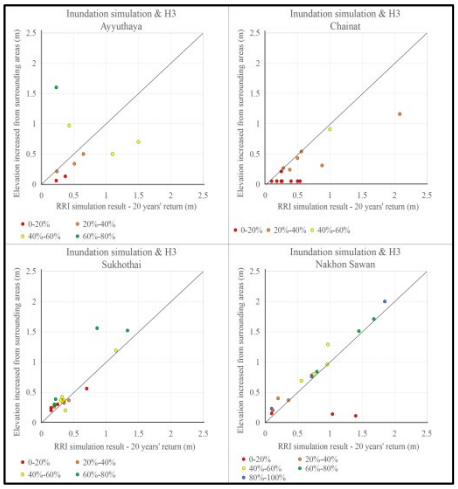


**Fig. 4. Relationship between the ground elevation of overall temples ($H_3$) and the simulation results of flood scenarios for a 20-year return period in the cities of Ayutthaya, Chainat, Sukhothai, and Nakhon Sawan (Temples are classified based on the proportion of natural elevation $H_3$ in the overall height increased $H_1$).**

## 4 Conclusions

This study demonstrated that the spatial distribution and architectural configurations of temples in the Chao Phraya River Basin reflected long-term community flood resilience. Temples were artificially elevated to enhance flood resilience, with the 20-year rainfall probability crucially aligned with residents' risk perceptions. Regional variations in flood resilience strategies highlighted differing levels of flood awareness and preparedness. These findings emphasized the need for further investigation into diverse flood management strategies, aiming to improve community-level resilience and strengthen flood risk mitigation approaches.

## Reference

[1] Chanta, S., & Sangsawang, O. (2012). Shelter-site selection during flood disaster. Proceedings of the 4th International Conference on Applied Operational Research pp. 282–288.

[2] Xia, J., Dong, Y., & Zou, L. (2022). Developing socio-hydrology: Research progress, opportunities and challenges. Journal of Geographical Sciences, 32(12), 2131–2146.

# Applying Initial Conditions into Multi-Scale Socio-Hydrological Flood Modeling in Nagoya City

○ Muthiah SADIDAH[1,2*], Daisuke KOMORI[1,2,3], Ryohei TACHIKAWA[4]
[1]Graduate School of Environmental Studies, Tohoku University, Miyagi 980-8572, Japan.
[2]Green Goals Initiative Laboratory, IRIDES building, Tohoku University, Miyagi 980-8572, Japan.
[3]International Research Institute of Disaster Science, Tohoku University, Sendai 980-8572, Japan
[4]Department of Civil and Environmental Engineering, Tohoku University, Sendai 980-8579, Japan
[*]E-mail: Muthiah.sadidah.t2@dc.tohoku.ac.jp

## Abstract

In previous socio-hydrological (SH) studies, the initial value of residents' flood memory has often been set to zero, although communities typically possess prior flood experience. Moreover, most SH model applications have been conducted at large spatial scales, such as entire cities or river basins, where multiple communities with different flood histories are aggregated. These assumptions limit the model's ability to reproduce localized human–flood interactions. To address these gaps, this study applied a modified SH model to frequent inland flood-prone areas in Nagoya City, Japan, incorporating a realistic initial memory condition and comparing model behavior across spatial scales. The model was first applied to five small-scale areas (0.04–0.05 km² each) over a 25-year period (1993–2017) and then to a large-scale area (91.5 km²) over 22 years (1996–2017). The initial memory values were estimated through a spin-up procedure that stabilized the memory variable before the main simulation period.

At the small scale, the model successfully reproduced both the levee and adaptation effects, indicating that realistic initial memory values improved the representation of flood memory and population dynamics. In contrast, these dynamics were less evident at the large scale, suggesting that spatial aggregation masks local socio-hydrological feedback. The results demonstrate that the SH model's ability to capture human–flood interactions strongly depend on both the initial memory condition and the spatial scale of analysis. These findings highlight the importance of incorporating realistic initial conditions and appropriate spatial resolution when applying the SH model for urban flood risk assessment and disaster risk reduction.

**Keywords:** socio-hydrological modeling, socio-hydrology, flooding, flood memory, society, initial condition, multi-scale

## 1 Introduction

Inland flooding has become a major cause of disaster losses in Japan, accounting for about 40–70% of all floods in cities such as Tokyo, Osaka, and Nagoya (Kato, 2021; Komori et al., 2022). Recent MLIT data (2023) show that inland floods still cause the largest share of total damage, emphasizing the need to understand both physical and societal dimensions of flooding.

Most socio-hydrological (SH) models have been applied at large scales and assume no prior societal memory, limiting their ability to capture localized responses (Xia et al., 2022; Komori et al., 2025). This study applies an improved SH model to frequent inland flood areas in Nagoya City, incorporating initial memory conditions and comparing multiple spatial scales to enhance the model's ability to capture human–flood interactions more accurately.

## 2 Materials and methods

Frequently flooded inland areas in Nagoya City were identified using flood hazard maps (1993–2017). Areas inundated five or more times—representing about 8% of the total flooded extent—were defined as "frequent." A 100 m mesh was selected as optimal (Komori et al., 2022), yielding 155 areas; five representative regions (Zenshincho, Tsunowaricho, Kanedacho, Yada-Minami, and Tatewakicho) were analyzed. Flood occurrence timing was classified as *early* (1993–2005), *continuous* (1993-2017), or *latter* (1993–2005 vs. 2006–2017). The small-scale areas ranged from 0.04–0.05 km², while the larger-scale area covered 91.5 km², enabling multi-scale comparison.

An improved socio-hydrological (SH) model (Komori et al., 2025) was applied to represent pluvial flooding by modifying the flood-intensity and protection-increment equations:

$$F = 1 - \exp\left(-\frac{R_F - \alpha_R \times H_-}{co}\right), if\ R_F > R_T$$

$$R_T = \alpha_R \times H_-$$

where $F$ is flood intensity (–), $R_F$ is rainfall intensity (mm/h), $\alpha_R$ is design rainfall intensity (mm/h), $H_-$ is pre-flood protection level (–), $R_T$ is rainfall threshold (mm/h), and $co$ is a coefficient relating rainfall to damage.

Population and memory dynamics were expressed as:

$$\frac{dD}{dt} = \rho_a\left(1 - D(1 + \alpha_D M)\right) - \Delta\left(\Psi(t)\right)FD_-$$

$$\frac{dM}{dt} = \Delta\left(\Psi(t)\right)FD_- - \mu_S M$$

where $D$ is normalized population density, $\rho_D$ is relative growth rate (/year), $\alpha_D$ is preparedness–awareness ratio (–), $\Delta(\Psi(t))$ is a flood-occurrence function (1 during flood, 0 otherwise), and $\mu_S$ is the rate of memory loss (/year).

Initial conditions for $M$ were determined through a spin-up simulation (1993–2005) until memory values stabilized. Model validation used the F-ratio between observed and simulated flood intensity.

## 3 Results and discussion

After applying the initial condition, differences in societal memory became evident across the target areas. In Yada Minami, the memory value showed a distinct decline—from 0.42 to 0.26 after 2000—whereas Tsunowaricho and Zenshincho displayed relatively stable or rising trends (see Fig. 1, Fig. 2, and Fig. 3, all representing results with initial conditions). Field surveys revealed zero household preparedness in Yada Minami despite continuous flooding, suggesting that repeated events did not necessarily strengthen awareness or collective memory.

The levee effect was observed in Tsunowaricho (see Fig.2), classified as a "latter" area where flooding became frequent after 2006. In this area, no flooding was recorded until 2008, resulting in very low community memory (0.02 in 1993). After 2006, the construction of flood countermeasures remained unfinished and could not accommodate the increasing rainfall intensity, leading to more frequent flooding events after 2008. Consequently, residents' flood memory rose sharply in 2008 (0.1962), and peaked at 0.27 in 2013. The F ratio also exceeded 1 in 2008, indicating that the inundation ratio was greater than the flood model projection, which represents the occurrence of the levee effect after memory decline due to no flood period.

At the larger spatial scale (see Figure 4), the SH model could not clearly reproduce the levee effect. In 2008, the observed inundation ratio exceeded the modeled flood intensity (F = 5.5), while societal memory remained high due to continuous small floods, preventing the typical pre-flood decline. In 2016, F < 1 indicated the adaptation effect, but memory values still fluctuated and declined instead of accumulating, suggesting that the model failed to capture adaptive behavior.

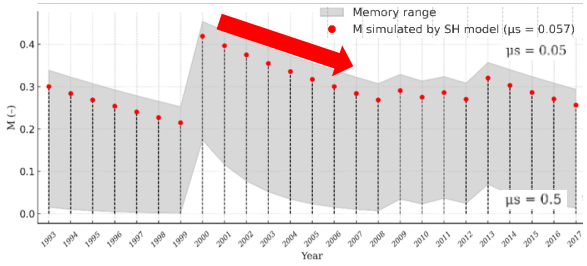


**Fig. 1. SH model results with initial condition (Yada Minami): flood memory**

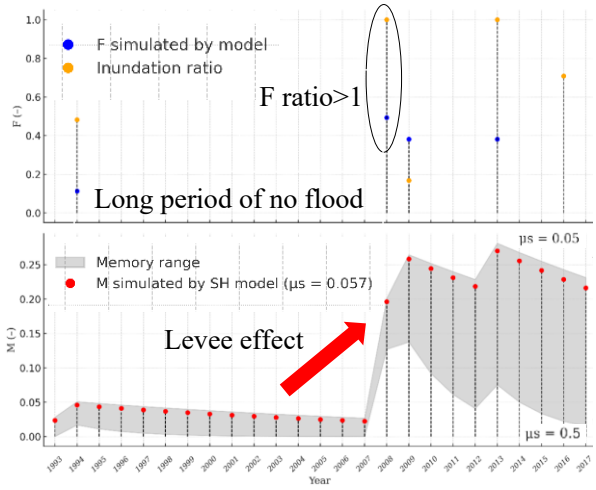


**Fig. 2. SH model results with initial condition (Tsunowaricho). (a) Flood intensity, (b) Flood memory**

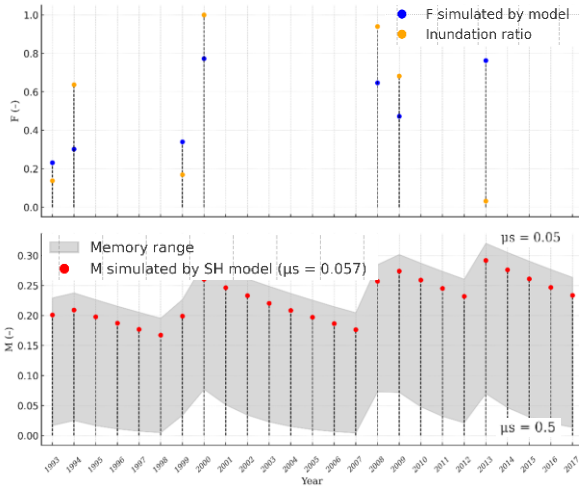


**Fig. 3. SH model results initial condition (Zenshincho). (a) Flood intensity, (b) Flood memory**

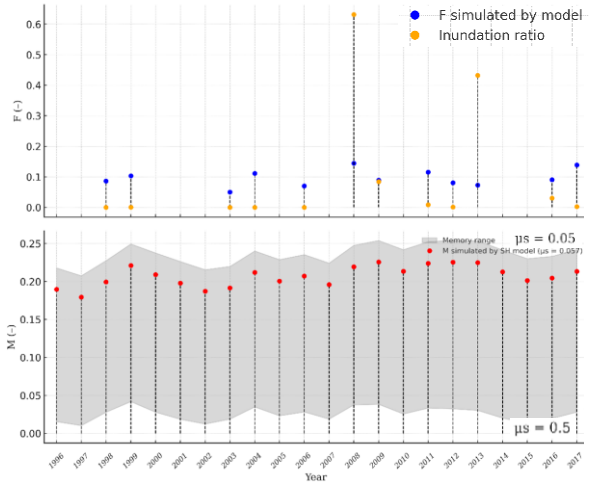


**Fig. 4. SH model results (larger scale of Nagoya City). (a) Flood intensity, (b) Flood memory**

## 4 Conclusions

This study applied a socio-hydrological (SH) model to inland flood-prone areas of Nagoya City, introducing realistic initial memory conditions and comparing results across spatial scales. At the small scale, the model captured both the levee effect after long flood-free periods and the adaptation effect under repeated flooding, it is showing that initial memory improves alignment with observed social and population trends. At the larger scale, these dynamics became less distinct, as spatial averaging reduced local feedback between people and floods. The findings highlight that realistic initial conditions and appropriate spatial resolution are essential for reproducing human–flood interactions and improving the SH model's reliability in urban flood analysis.

## Reference

Baldassarre, G. D., Viglione, A., Carr, G., Kuil, L., Salinas, J. L., & Blöschl, G. (2013). Socio-hydrology: Conceptualising human–flood interactions. *Hydrology and Earth System Sciences, 17*(8), 3295–3303. https://doi.org/10.5194/hess-17-3295-2013

Komori, D., Oyatsu, Y., Sadidah, M., & Nagami, K. (2025). Improvement of socio-hydrological model to capture the dynamics of pluvial floods: A case study in frequent pluvial flooding areas in Wakayama City, Japan. *Frontiers in Water, Water and Human Systems* section, *Advances in Socio-hydrology for Building Resilience to a Changing Climate*. (in press).